

IntechOpen

# Shape-Memory Materials

*Edited by Alicia Esther Ares*





---

# SHAPE-MEMORY MATERIALS

---

Edited by **Alicia Esther Ares**

## Shape-Memory Materials

<http://dx.doi.org/10.5772/intechopen.74096>

Edited by Alicia Esther Ares

### Contributors

Takuo Sakon, Naoki Fujimoto, Sho Saruki, Takeshi Kanomata, Hiroyuki Nojiri, Yoshiya Adachi, Petrică Vizureanu, Dragos Cristian Achitei, Mirabela Georgiana Minciuna, Manuela Cristina Perju, Meddour Belkacem, Brek Samir, Velaphi Msomi, Graeme Oliver, Qianhua Kan, Jian Li, Zebin Zhang, Guozheng Kang, Beñat Artetxe, Leire Ruiz, José Luis Vilas-Vilela, Leyre Pérez-Álvarez, Juan Manuel Gutierrez-Zorrilla

### © The Editor(s) and the Author(s) 2018

The rights of the editor(s) and the author(s) have been asserted in accordance with the Copyright, Designs and Patents Act 1988. All rights to the book as a whole are reserved by INTECHOPEN LIMITED. The book as a whole (compilation) cannot be reproduced, distributed or used for commercial or non-commercial purposes without INTECHOPEN LIMITED's written permission. Enquiries concerning the use of the book should be directed to INTECHOPEN LIMITED rights and permissions department ([permissions@intechopen.com](mailto:permissions@intechopen.com)). Violations are liable to prosecution under the governing Copyright Law.



Individual chapters of this publication are distributed under the terms of the Creative Commons Attribution 3.0 Unported License which permits commercial use, distribution and reproduction of the individual chapters, provided the original author(s) and source publication are appropriately acknowledged. If so indicated, certain images may not be included under the Creative Commons license. In such cases users will need to obtain permission from the license holder to reproduce the material. More details and guidelines concerning content reuse and adaptation can be found at <http://www.intechopen.com/copyright-policy.html>.

### Notice

Statements and opinions expressed in the chapters are those of the individual contributors and not necessarily those of the editors or publisher. No responsibility is accepted for the accuracy of information contained in the published chapters. The publisher assumes no responsibility for any damage or injury to persons or property arising out of the use of any materials, instructions, methods or ideas contained in the book.

First published in London, United Kingdom, 2018 by IntechOpen

eBook (PDF) Published by IntechOpen, 2019

IntechOpen is the global imprint of INTECHOPEN LIMITED, registered in England and Wales, registration number:

11086078, The Shard, 25th floor, 32 London Bridge Street

London, SE19SG – United Kingdom

Printed in Croatia

British Library Cataloguing-in-Publication Data

A catalogue record for this book is available from the British Library

Additional hard and PDF copies can be obtained from [orders@intechopen.com](mailto:orders@intechopen.com)

Shape-Memory Materials

Edited by Alicia Esther Ares

p. cm.

Print ISBN 978-1-78923-682-8

Online ISBN 978-1-78923-683-5

eBook (PDF) ISBN 978-1-83881-771-8

# We are IntechOpen, the world's leading publisher of Open Access books Built by scientists, for scientists

**3,700+**

Open access books available

**116,000+**

International authors and editors

**119M+**

Downloads

**151**

Countries delivered to

Our authors are among the  
**Top 1%**

most cited scientists

**12.2%**

Contributors from top 500 universities



**WEB OF SCIENCE™**

Selection of our books indexed in the Book Citation Index  
in Web of Science™ Core Collection (BKCI)

Interested in publishing with us?  
Contact [book.department@intechopen.com](mailto:book.department@intechopen.com)

Numbers displayed above are based on latest data collected.  
For more information visit [www.intechopen.com](http://www.intechopen.com)





# Meet the editor



Alicia Esther Ares has been a headline professor of Materials Science at the Chemical Engineering Department, School of Sciences (FCEQyN), National University of Misiones (UNaM), Posadas, Misiones, Argentina, since December 2013. She has also been an independent researcher at the National Scientific and Technical Research Council (CONICET), Argentina since January 2015. Previously a research associate at CONICET (2008–2014) and associate professor at UNaM (2007–2013), she has also been an assistant professor at UNaM (1989–2007). She graduated at the University of Misiones in 1992 and completed a PhD degree in Materials Science at the Institute of Technology “Jorge Sabato,” UNSAM-CNEA, Buenos Aires, Argentina. Later, she undertook postdoctoral stays at the following institutions: Faculdade de Engenharia Mecânica, Departamento de Engenharia de Materiais, Universidade Estadual de Campinas, Campinas, São Paulo, Brasil (2001 and 2005–2006); Department of Materials Science and Engineering, University of Florida, Gainesville, Florida, United States (2002–2003); and the Faculty of Sciences, National University of Misiones, Posadas-Misiones, Argentina (2003–2004). She has 30 years of teaching experience both at the undergraduate and graduate levels. Her articles are published in well-established international journals.



---

# Contents

---

## **Preface XI**

- Chapter 1 **Magnetic Field-Induced Strain of Metamagnetic Heusler Alloy Ni<sub>41</sub>Co<sub>9</sub>Mn<sub>31.5</sub>Ga<sub>18.5</sub> 1**  
Takuo Sakon, Naoki Fujimoto, Sho Saruki, Takeshi Kanomata, Hiroyuki Nojiri and Yoshiya Adachi
- Chapter 2 **Aspects Regarding Thermal-Mechanical Fatigue of Shape Memory Alloys 17**  
Petrică Vizureanu, Dragoș-Cristian Achiței, Mirabela-Georgiana Minciună and Manuela-Cristina Perju
- Chapter 3 **Modeling of the Two-Way Shape Memory Effect 43**  
Meddour Belkacem and Brek Samir
- Chapter 4 **Linear Shape Memory Alloy Thermomechanical Actuators 57**  
Velaphi Msomi and Graeme Oliver
- Chapter 5 **Experiments and Models of Thermo-Induced Shape Memory Polymers 75**  
Qianhua Kan, Jian Li, Guozheng Kang and Zebin Zhang
- Chapter 6 **Shape Memory Hydrogels Based on Noncovalent Interactions 95**  
Leire Ruiz-Rubio, Leyre Pérez-Álvarez, Beñat Artetxe, Juan M. Gutiérrez-Zorrilla and José Luis Vilas



---

# Preface

---

Shape-memory materials (SMMs) are materials that react under physical or chemical changes, variations of magnetic or electric fields, and that when returning to the initial conditions recover their original form, capable of repeating this process an infinite number of times without deteriorating.

Shape-memory materials are materials with shape-memory, capable of self-diagnosis and repair, thanks to their capacity for change. These materials are assigned an initial shape, and after being subjected to the physical field or corresponding chemical reaction, their shape is adjusted, so that, in the presence of said field or reaction, the materials vary between the two desired forms.

This kind of material has an infinite number of applications, for example, replacing the valves in motors or bearings, since one could take advantage of the capacity of self-regeneration so as not to have to change them if they are degraded, but by submitting them to the appropriate field, the problem would be solved.

Shape-memory alloys have two types of special behaviors, which are actually two expressions of the same phenomenon: shape-memory and super elasticity. In both cases, the behavior is the product of a transformation of phases without diffusion, of martensitic type, in which the order to first neighbors is not lost. Strictly speaking, order is lost, but what is not lost are neighboring atoms. If in a state, an atom has a group of first neighbors, its position in the second state is different, but the neighbors do not change.

Fitting the material properties of polymers is much easier compared with that of metals/alloys. In addition, the cost (both material cost and processing cost) of polymers is traditionally much lower. SMP composites have remarkably widened the potential applications of SMPs.

This book, "Shape-Memory Materials," logically develops through careful presentation of relevant theories and models occurring in a variety of materials. Conclusions and outlooks for the future of SMMs are presented in this book.

## **Section I: Magnetic Field-Induced Strain of Metamagnetic Heusler Alloy $\text{Ni}_{41}\text{Co}_9\text{Mn}_{31.5}\text{Ga}_{18.5}$**

The authors investigate the magnetic functionality of polycrystalline metamagnetic Heusler alloy  $\text{Ni}_{41}\text{Co}_9\text{Mn}_{31.5}\text{Ga}_{18.5}$  and performed magnetic field-induced strain (MFIS) measurements. The investigation of time response of the MFIS was performed by means of sweep water-cooled electric magnet, zero magnetic field to 1.66 T in 8.0 seconds at 354 K. 2.210<sup>-4</sup>

MFIS was observed, which was 80% of the MFIS in 60 seconds mode. This indicates that high-speed transition has occurred with the application of magnetic fields.

### **Section II: Aspects Regarding Thermal-Mechanical Fatigue of Shape-Memory Alloys**

The authors present advanced research about the use of metallic alloys with shape-memory properties in construction and exploitation of parts subjected to combined stress by thermal and mechanical fatigue during their functioning. The research and results presented in this chapter make useful data on design principles available to scientists.

### **Section III: Modeling of the Two-Way Shape Memory Effect**

The authors developed a 3D constitutive model using the principles of thermodynamics and a simple formalism. These principles have permitted the authors to write criteria of transformation. This macroscopic model is developed by simple formalism and assumptions. This model can be used in applications for engineering problems, in order to simulate the pseudoelastic effect of shape-memory alloys.

### **Section IV: Linear Shape-Memory Alloy Thermomechanical Actuators**

The authors developed a finite element analysis based on the proposed SMA model. The finite element analysis was performed on the 1D setup, which was oriented on the 2D space. The c++ code was developed in order to perform the 2D numerical analysis. The experiment was performed in order to obtain the parameters to input in the developed code and also to validate the numerical results. The maximum deflection obtained numerically matches that which was measured experimentally. It was verified through the results that the developed SMA model has the ability to capture all the temperature range and not only the intended range.

### **Section V: Experiments and Models of Thermo-Induced Shape-Memory Polymers**

The authors studied some important viscoelastic and viscoplastic features, such as rate-dependent and temperature-dependent stress-strain curves and nonuniform temperature distribution. The results were experimentally investigated and discussed regarding the interaction between the mechanical deformation and the internal heat generation. The influences of loading rate and peak strain on the shape-memory effect (SME) and shape-memory degeneration of TSMPs were revealed under monotonic and cyclic thermo-mechanical loadings, respectively.

### **Section VI: Shape-Memory Hydrogels Based on Noncovalent Interactions**

Shape-memory polymers (SMPs) are polymeric materials that are capable of fixing temporary shape and recovering the permanent shape in response to external stimuli. The authors described shape memory hydrogels based on noncovalent interactions.

**Alicia Esther Ares**

Chemical Engineering Department  
School of Sciences (FCEQyN)  
National University of Misiones (UNaM)  
Posadas, Misiones, Argentina

---

# Magnetic Field-Induced Strain of Metamagnetic Heusler Alloy $\text{Ni}_{41}\text{Co}_9\text{Mn}_{31.5}\text{Ga}_{18.5}$

---

Takuo Sakon, Naoki Fujimoto, Sho Saruki,  
Takeshi Kanomata, Hiroyuki Nojiri and  
Yoshiya Adachi

Additional information is available at the end of the chapter

<http://dx.doi.org/10.5772/intechopen.76291>

---

## Abstract

$\text{Ni}_{41}\text{Co}_9\text{Mn}_{31.5}\text{Ga}_{18.5}$  is a re-entrant and metamagnetic Heusler alloy. In order to investigate the magnetic functionality of polycrystalline  $\text{Ni}_{41}\text{Co}_9\text{Mn}_{31.5}\text{Ga}_{18.5}$ , magnetic field-induced strain (MFIS) measurements were performed. A 0.12% MFIS was observed at 340 K and 10 T. Strict MFISs between 330 and 370 K were observed. These magneto-structural variances acted in concert with the metamagnetic property observed by the magnetization measurements and magneto-caloric property observed by the caloric measurements in applied magnetic fields. The MFISs were proportional to the fourth power of the magnetization, and this result is in agreement with Takahashi's spin fluctuation theory of itinerant electron magnetism. The investigation of time response of the MFIS was performed by means of water-cooled electric magnet, zero magnetic field to 1.66 T in 8.0 s at 354 K. A  $2.2 \times 10^{-4}$  MFIS was observed, which was 80% of the MFIS in a 60-s mode. This indicates that a high-speed transition has occurred on applying magnetic fields.

**Keywords:** magnetostriction, Heusler alloys, shape memory alloys, metamagnetic transition, itinerant magnetism

---

## 1. Introduction

In recent years, the ferromagnetic shape memory alloy (FSMA) was investigated as a candidate of the functional materials widely. Among FSMA,  $\text{Ni}_2\text{MnGa}$  is the most famous alloy [1]. The alloy has a cubic  $L2_1$  Heusler structure (space group of  $Fm\bar{3}m$ ), and ferromagnetic

---

transition realized [2, 3]. Cooling from room temperature, a martensite transition occurred at the martensitic transition temperature,  $T_M$ . Below  $T_M$ , a superstructure state occurred as a result of lattice deformation [4-6].

New alloys in the FMSAs of NiMnIn-, NiMnSn-, and NiMnSb-type Heusler alloys have been studied [7, 8]. In these alloys, a metamagnetic transition from paramagnetic martensite phase to ferromagnetic austenite phase occurred, and reverse martensitic transition, which was induced by magnetic fields, occurred under high magnetic fields [9, 10]. These alloys are hopeful as a metamagnetic shape memory alloys with a magnetic field-induced shape memory effect (MSIF) and as magnetocaloric materials which can be cooled down or heated up on applying external magnetic fields. It is noticeable that 3% MFIS has been observed for  $\text{Ni}_{45}\text{Co}_5\text{Mn}_{36.7}\text{In}_{13.3}$  single crystal in compressive stress-strain measurements [11].

The Co-doped NiCoMnGa-type alloys turned the magnetic order of the parent phase from antiferromagnetic or paramagnetic phase, due to a large magnetization change across the transformation. As a result, it strengthens magnetic field driving force dramatically [12-24]. As for  $\text{Ni}_{50-x}\text{Co}_x\text{Mn}_{31.5}\text{Ga}_{18.5}$ , the determined phases are a paramagnetic austenite (Para-A) phase, ferromagnetic austenite phase (Ferro-A), paramagnetic martensite phase (Para-M), and ferromagnetic martensite (Ferro-M) phase, with cooling from a higher temperature than  $T_C$ , which indicates re-entrant ferromagnetism [23].

Albertini et al. performed the experimental studies regarding the composition dependence of the structural and magnetic properties of the Ni-Mn-Ga ferromagnetic shape memory alloys substituting Co for Ni atoms around the composition of  $\text{Ni}_{50}\text{Mn}_{30}\text{Ga}_{20}$  [12, 20]. The magnetic and structural properties indicated remarkable discontinuities around the martensitic transition. A metamagnetic transition appeared in the magnetic field around 400 K. The field dependence of the reverse martensitic transition temperature  $dT_R/\mu_0 dH$  was  $-2.8$  K/T and that of the thermal strain was reported. The most characteristic alloy is  $\text{Ni}_{41}\text{Co}_9\text{Mn}_{32}\text{Ga}_{18}$ . The magnetic susceptibility indicates a re-entrant magnetism property. We studied the magnetic properties of polycrystalline  $\text{Ni}_{41}\text{Co}_9\text{Mn}_{31.5}\text{Ga}_{18.5}$ . Magnetization results indicated the metamagnetic transition between 330 and 370 K for 0–10 T. Moreover, a 0.1% magnetic field-induced strain (MFIS) was observed at the temperature of 340 K [23].

In our former article [25], we determined the magnetic field dependence of the magnetization of  $\text{Ni}_{41}\text{Co}_9\text{Mn}_{31.5}\text{Ga}_{18.5}$  around the Curie temperature in the martensite phase in order to investigate the properties of the itinerant electron magnetism according to Takahashi's spin fluctuation theory of itinerant electron magnetism [26, 27]. The  $M^4$  versus  $H/M$  plot was crossed across the coordinate axis at the Curie temperature in the martensite phase,  $T_{CM} = 263$  K, and indicates a good linear relation behavior around  $T_{CM}$ . The results were in agreement with the Takahashi's theory concerning itinerant electron magnetism [26, 27]. Moreover, the spin fluctuation temperature  $T_A$  can be obtained from the  $M^4$  versus  $H/M$  plot. The obtained  $T_A$  was 703 K. This value was much smaller than Ni ( $1.76 \times 10^4$  K). The value was comparable to that of  $\text{UGe}_2$  (493 K), which is famous for the strongly correlated heavy fermion ferromagnet [27, 28].

Takahashi suggested that the anomalous behavior for the magnetostriction can be observed under the influence of the itinerant spin fluctuations around the critical temperature [27]. It is mentioned that the reason is that the magnetostriction is given by the volume derivative

of the free energy. By Eq. (6.101) of [27], the magnetostriction is proportional to the fourth power of the magnetization,  $M^4$ . The experimental magnetostriction study of weak itinerant ferromagnet MnSi was performed by Matsunaga et al. [29]. They plotted the magnetostriction against  $M^2$ . Around the Curie temperature,  $T_C = 30$  K, the plot considerably deviated from the linearity. Takahashi mentioned that the linearity was confirmed by plotting the magnetostriction data against  $M^4$  at  $T = 29$  K around  $T_C$ .

In this chapter, we performed MFIS measurements by means of a 10-T helium-free superconducting magnet and a 1.7-T water-cooled electric magnet. We compared the results of the strain and calorimetric differential scanning calorimetry (DSC) measurements and discussed the irreversibility of the MFIS and the reverse martensitic and metamagnetic transition. We investigated the correlations between magneto-structural variance and the magneto-caloric property observed by the caloric measurements in applied magnetic fields. It is interesting with the investigation of time response of the MFIS for the purpose of industrial use [30]. The time response of the MFIS performed by means of a 1.6-T water-cooled electric magnet and under atmospheric pressure,  $P = 0.1$  MPa, was investigated. We also investigated the relation between the magnetostriction and the magnetization according to Takahashi's spin fluctuation theory of the itinerant ferromagnet for  $\text{Ni}_2\text{MnGa}$  and  $\text{Ni}_{41}\text{Co}_9\text{Mn}_{31.5}\text{Ga}_{18.5}$ .

## 2. Sample properties and experimental details

The crystal structure of  $\text{Ni}_{41}\text{Co}_9\text{Mn}_{31.5}\text{Ga}_{18.5}$  is tetragonal  $DO_{22}$  structure, and the sample preparation of polycrystalline alloy was shown in our former article [23]. The nominal concentrations of the elements were Ni 41.0, Co 9.0, Mn 31.5, and Ga 18.5 at.%. The concentrations of the elements after thermal treatment are shown in **Table 1**. The ratio was almost the same as that of the nominal state. When cooling from 500 K, a ferromagnetic transition in the austenite phase was realized at  $T_C^A = 465$  K. At the martensitic transition temperature,  $T_M = 315$  K, the magnetization decreased drastically. The reverse martensitic transition temperature  $T_R$  was 380 K. The re-entrant magnetism, ferromagnetic-paramagnetic state, should be interacted with the crystal structures. The hysteresis of temperature,  $T_R - T_M$  was 65 K, which is much larger than that of other  $\text{Ni}_2\text{MnGa}$ -type alloys. This is due to the large motive force in order for a martensitic transition to occur [24].

MFIS measurements were performed with bulk samples with the size of  $0.8 \times 3.0 \times 4.0$  mm<sup>3</sup>. Strain gauges were used (KFH-02-120-C1-16, size: sensor grid 0.2 mm length  $\times$  1.0 mm width, film base 2.5 mm length  $\times$  2.2 mm width, Kyowa Dengyo Co., Ltd., Yamagata, Japan). Strain gauge was fixed parallel to the long distance direction (4.0 mm) of the sample.

Ni	Co	Mn	Ga
40.8	9.0	31.5	18.7

**Table 1.** The concentrations of elements by means of EDS spectrometry (at. %).

External magnetic field was applied parallel to the long distance direction of the sample, and elongation of the sample was measured in applied magnetic fields and in atmospheric pressure. Measurements were performed by means of a 10-T helium-free magnet (10 T-CSM) at High Field Laboratory for Superconducting Materials, Institute for Materials Research, Tohoku University. We also performed MFIS measurements by means of a 1.7-T water-cooled electric magnet at Ryukoku University in order to investigate time response of MFIS. The magnetization measurements were performed by using a pulsed-field magnet with the time constant of 6.3 ms. The absolute value was calibrated against a sample of pure Ni.

### 3. Results and discussion

#### 3.1. Relation between the magnetic field-induced strain and the magnetic entropy of $\text{Ni}_{41}\text{Co}_9\text{Mn}_{31.5}\text{Ga}_{18.5}$

In this section, we compared the results of the strain and calorimetric DSC measurements of  $\text{Ni}_{41}\text{Co}_9\text{Mn}_{31.5}\text{Ga}_{18.5}$ . We considered the correlation between the magnetic field-induced strain and the magnetic entropy.

**Figure 1** shows the MFIS under steady field by means of the helium-free superconducting magnet. The MFIS measurements in this study were performed under atmospheric pressure and without the compression to make a pre-strain. The point zero of MFIS at each temperature is moved by  $1 \times 10^{-4}$  below 315 K and by  $5 \times 10^{-4}$  above 330 K. The thermal condition was the same as that for the magnetization measurement [23]. When increasing the magnetic field, distinct MFIS was observed. The maximum MFIS was 0.12%, which was approximately the same value as that of the thermal strain for the reverse martensitic transition. The shape of MFIS is similar to that of polycrystalline  $\text{Ni}_{41}\text{Co}_9\text{Mn}_{32}\text{Ga}_{16}\text{In}_2$ , where the alloy is also a re-entrant metamagnetic Heusler alloy, and 0.30% MFIS was observed [12]. The field dependence of the reverse martensitic transition temperature,  $dT_{\text{R}}/\mu_0 dH$ , are  $-7.9$ ,  $-6.8$ , and  $-4.8$  K/T for  $\text{Ni}_{41}\text{Co}_9\text{Mn}_{31.5}\text{Ga}_{18.5}$  [23],  $\text{Ni}_{41}\text{Co}_9\text{Mn}_{32}\text{Ga}_{16}\text{In}_2$  [12], and  $\text{Ni}_{45}\text{Co}_5\text{Mn}_{36.7}\text{In}_{13.3}$  respectively [11]. The field dependence of the reverse martensitic transition temperature of the ferromagnetic and non-metamagnetic  $\text{Ni}_2\text{MnGa}$  type alloys is between 0.2 and 1.0 K/T [2, 31, 32]. As for metamagnetic Heusler alloys,  $dT_{\text{R}}/\mu_0 dH$  is much larger than that of non-metamagnetic Heusler alloys. Therefore, the MFIS occurs at a wide temperature range. The strain curves shown in **Figure 1** and the thermal strain in Ref. [23] suggest that the magneto-structural transition of  $\text{Ni}_{41}\text{Co}_9\text{Mn}_{31.5}\text{Ga}_{18.5}$  alloy is very sensitive to magnetic fields. Below 330 K, the MFIS value returned to zero when a magnetic field became zero. By contrast, the MFIS value remained at the limit value without returning zero.

The MFIS of 2, 4, 6, and 8 T is shown in **Figure 2**. Between 340 and 370 K, large MFIS was observed. Metamagnetic S-shape like  $M$ - $H$  curve was observed for the magnetization around 360 K [23]. The decreasing field process shows ferromagnetic behavior. Magnetization process indicates that the paramagnetic to ferromagnetic transition occurred. Considering the magnetization, MFIS indicates that the structural transformation from the paramagnetic martensite phase to the austenite ferromagnetic phase occurred. The MFIS and metamagnetism indicate

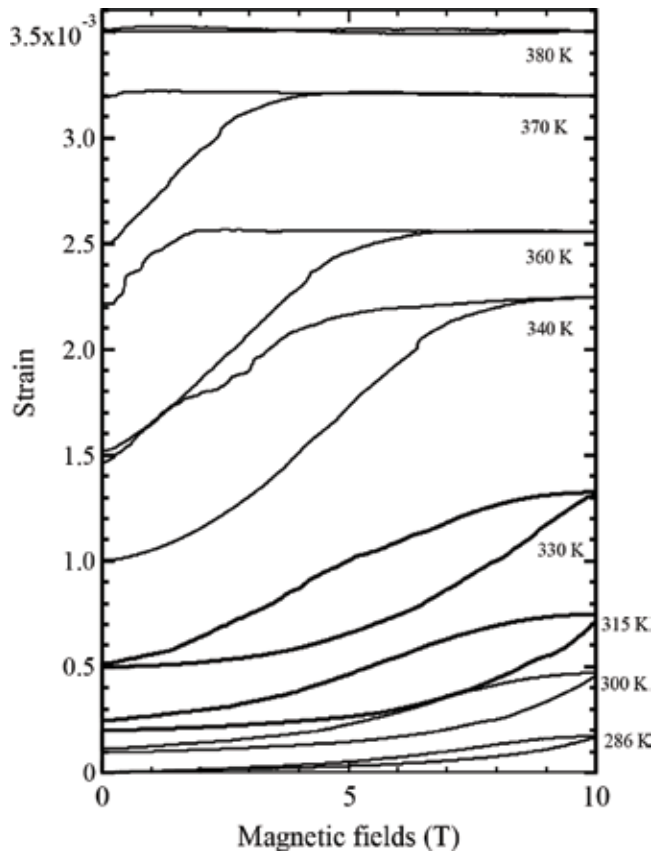


**Figure 1.** MFIS of  $\text{Ni}_{41}\text{Co}_9\text{Mn}_{31.5}\text{Ga}_{18.5}$  in static magnetic fields. The point zero at each temperature is moved by  $1 \times 10^{-4}$  below 315 K and by  $5 \times 10^{-4}$  above 330 K.

that the magneto-structural coupling is large. The 0.12% (1200 ppm) MFIS is larger than the magnetostriction of TbDyFe single crystal under atmospheric pressure [33]. In this study,  $\text{Ni}_{41}\text{Co}_9\text{Mn}_{38.5}\text{Ga}_{18.5}$  is a polycrystalline sample; then, it is easier to process and handle the sample than single crystals. **Table 2** indicates the thermal linear striction  $\Delta L/L(t)$ , saturated magnetostriction  $\Delta L/L(m)$ , and relative volume discontinuity at the martensitic transition,  $\Delta V/V$ .

In the former article, we studied the magneto-caloric properties of  $\text{Ni}_{41}\text{Co}_9\text{Mn}_{31.5}\text{Ga}_{18.5}$  polycrystalline sample by means of the differential scanning calorimetry (DSC) measurements [25]. Magneto-calorimetric measurements and magnetization measurements of  $\text{Ni}_{41}\text{Co}_9\text{Mn}_{31.5}\text{Ga}_{18.5}$  polycrystalline ferromagnetic shape memory alloy (FSMA) were performed across the  $T_R$  at atmospheric pressure. When the sample was warmed from the martensite phase, a gradual increase in the thermal expansion due to the reverse martensitic transition at  $T_R$  was observed by the thermal expansion experimental study. These transition temperatures decreased steeply with an increasing magnetic field. The field dependence of the reverse martensitic transition temperature,  $dT_R/\mu_0 dH$ , is  $-7.9$  K/T near zero fields. From the DSC measurements, the value of the latent heat was obtained as 2.6 kJ/kg in zero fields. The maximum value of

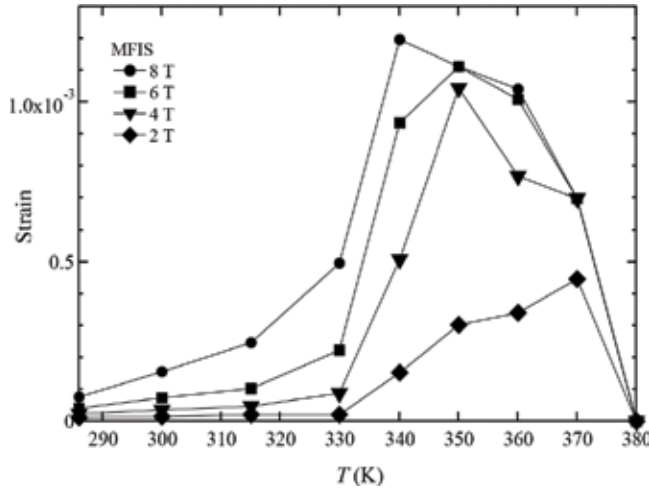


**Figure 2.** Field dependences of the MFIS of  $\text{Ni}_{41}\text{Co}_9\text{Mn}_{31.5}\text{Ga}_{18.5}$ . The values of MFIS at 350 K were quoted from our former result [23].

Alloys	$\Delta L/L(t)$	$\Delta L/L(m)$	$\Delta V/V$ (%)	Reference
$\text{Ni}_{41}\text{Co}_9\text{Mn}_{31.5}\text{Ga}_{18.5}$	$1.1 \times 10^{-3}$	$1.2 \times 10^{-3}$	$\sim 0.33$	This work
$\text{Ni}_{41}\text{Co}_9\text{Mn}_{32}\text{Ga}_{16}\text{In}_2$	$3.5 \times 10^{-3}$	$3.0 \times 10^{-3}$	$\sim 0.9$	[12]

**Table 2.** The thermal linear striction  $\Delta L/L(t)$ , saturated magnetostriction  $\Delta L/L(m)$ , and the relative volume discontinuity at the martensitic transition,  $\Delta V/V$ .

the entropy change  $\Delta S$  was 7.0 J/kgK in zero fields, and with increasing magnetic fields,  $\Delta S$  was gradually increased. The relative cooling power (RCP) is obtained by integration  $\Delta S$  with the temperature. The RCP was 104 J/kg at 2.0 T, which was almost as same as the value with In-doped  $\text{Ni}_{41}\text{Co}_9\text{Mn}_{32}\text{Ga}_{16}\text{In}_2$  alloy [12].

Now, we compare the results of the strain and calorimetric DSC measurements. **Figure 3** shows the temperature dependence of the MFIS and entropy change. The entropy change  $\Delta S = S(6 \text{ T}) - S(0 \text{ T})$  was obtained from magnetization results and DSC results between zero field and 6 T, from the DSC results  $\Delta S$  in steady fields [25].

$\Delta S$  shows a finite value above 330 K. On the contrary, the MFIS shows almost zero below 330 K. The reversible MFIS (magnetostriction) was observed below 330 K. Above 330 K, irreversible MFIS and S-shape like  $M$ - $H$  curve were observed. Considering these results, in the irreversible region  $T \geq 330 \text{ K}$ , metamagnetic and reverse martensitic transition occurred between the paramagnetic martensite and ferromagnetic parent austenite phases. Around  $T_R$ , large latent heat was observed by DSC measurement. The irreversible MFIS, S-shape like  $M$ - $H$  curve, and the observation of latent heat indicates that this transition is first-order transition. Therefore, in the finite  $\Delta S$  value region ( $330 \text{ K} \leq T \leq 390 \text{ K}$ ), irreversible and large MFIS can be observed. This result indicates the strong influence of magnetic fields for magneto-structural transformation.

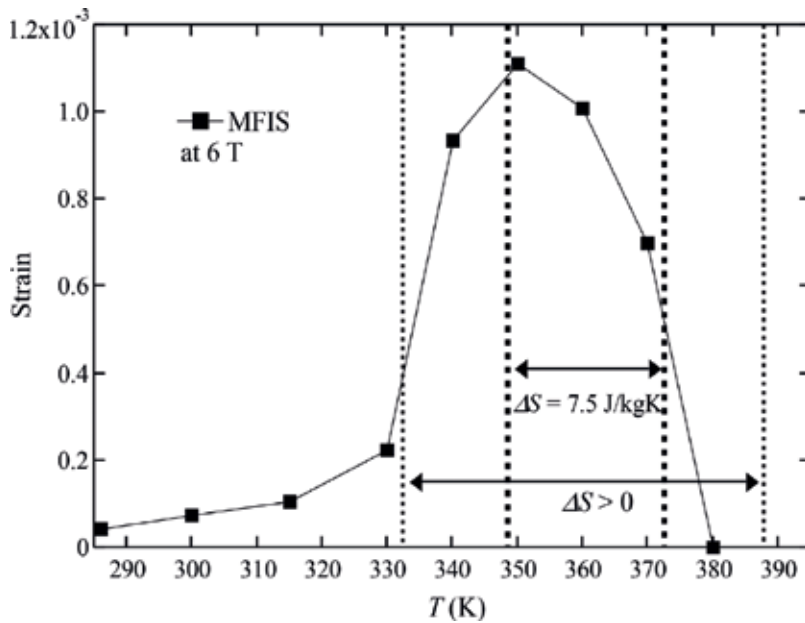


**Figure 3.** Temperature dependence of the MFIS at 6 T. Entropy change obtained from DSC results  $\Delta S$  [29] between zero field and 6 T is also shown. Thin dotted lines indicate the area for  $\Delta S > 0$ . Bold dotted lines indicate the area for  $\Delta S$  around 7.5 J/kgK.

### 3.2. Forced magnetostriction around the critical temperatures

In this section, we offer a topic of forced magnetostriction around the Curie temperature or magneto-structural transition temperature. The spin fluctuation theory of itinerant electron magnetism suggests that the critical index  $\delta$  is defined by the critical magnetic isotherm function,  $H \propto M^\delta$ , where  $\delta$  is around 5 [27]. Some scientists studied this relation concerning itinerant ferromagnetism. Nishihara et al. studied the magnetic field dependences of Ni and  $\text{Ni}_2\text{MnGa}$  [34]. As for Ni, the  $M^4$  versus  $H/M$  plot shows the reasonable linear relation at the Curie temperature. The critical temperature of the spin fluctuation temperature,  $T_A$ , was obtained as  $1.76 \times 10^4$  K. This value is comparable with the value of  $1.26 \times 10^4$  K, which was obtained by neutron diffraction experiments [35]. As for  $\text{Ni}_2\text{MnGa}$ , the critical index  $\delta$  of the magnetic field dependence of the magnetization,  $H \propto M^\delta$ , at the Curie temperature was  $4.70 \pm 0.5$  [34]. We measured the magnetization of  $\text{Ni}_2\text{MnGa}$  at the Curie temperature,  $T_C = 375$  K. **Figure 4** presents the  $M^{\delta-1}$  versus  $H/M$  plot. This figure indicates good linearity. These results indicate that the critical index  $\delta$  of the magnetic field dependence of the magnetization is 4.70 and confirms the result of the former magnetization experiment.

In this study, we measured the magnetostriction of  $\text{Ni}_2\text{MnGa}$  at the Curie temperature in order to investigate the magnetization dependence of the forced magnetostriction. **Figure 5** presents the magnetostriction  $\Delta L/L$  versus  $M^4$  plot. The dotted line indicates a linear plot in order to guide the eyes. The result shows good linearity. It is considered that this result orders the Takahashi's spin fluctuation theory. The magnetization analysis of  $\text{Ni}_{41}\text{Co}_9\text{Mn}_{31.5}\text{Ga}_{18.5}$  around the Curie temperature in the martensite phase according to the Takahashi's spin fluctuation theory was performed in the former article, as mentioned in Section 1 [25].

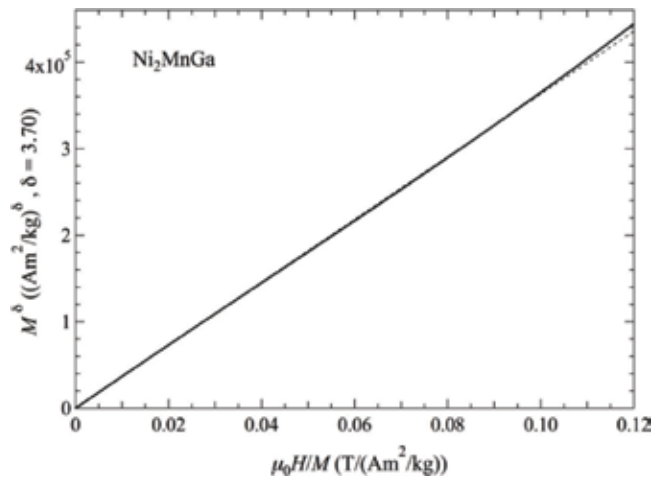


**Figure 4.** The  $M^{3.7}$  versus  $H/M$  plot of  $\text{Ni}_2\text{MnGa}$ . The dotted line is a fitted linear line.

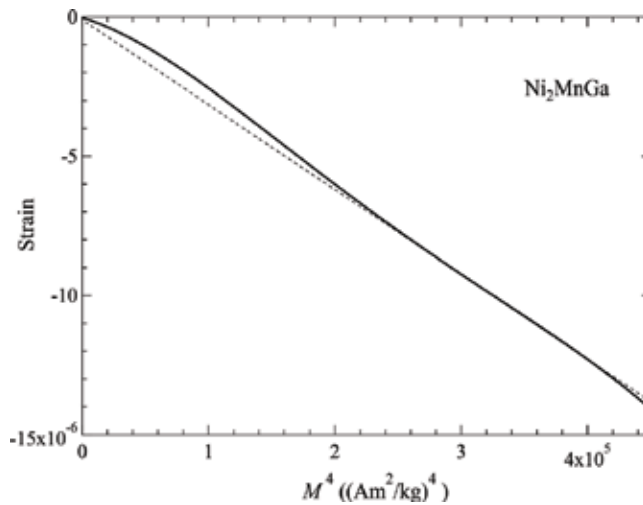


**Figure 5.** The magnetostriction  $\Delta L/L$  versus  $M^4$  plot of  $\text{Ni}_2\text{MnGa}$ . The dotted line is a fitted linear line.

We studied the magnetostriction at the Curie temperature in the martensite phase,  $T_C^M = 263$  K. At this temperature, no structural phase transition occurred. Therefore, the striction under magnetic fields was decided as the magnetostriction. **Figure 6** shows the plot of the magnetostriction against  $M^2$  at 263 K for  $\text{Ni}_{41}\text{Co}_9\text{Mn}_{31.5}\text{Ga}_{18.5}$ . The magnetostriction was not proportional to  $M^2$ . The plot was rounded. The plot of the numerically estimated magnetostriction at  $T_C$  was also rounded against  $M^2$  [27]. **Figure 7** shows the plot of the magnetostriction against  $M^4$  at 263 K. The dotted lines are linearly fitted lines. The fitted line passed the origin and shows good linearity, as that of  $\text{Ni}_2\text{MnGa}$ . It is conceivable that these results indicate that the magnetostriction is proportional to the fourth power of the magnetization,  $M^4$ .

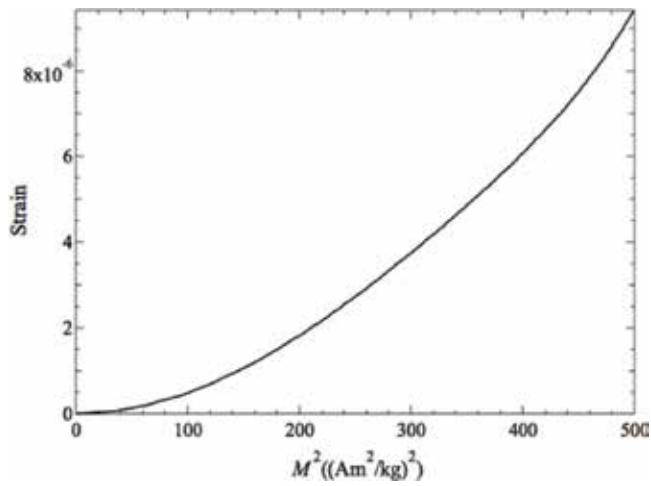


Figure 6. The plot of the magnetostriction against  $M^2$  at 263 K for  $\text{Ni}_{41}\text{Co}_9\text{Mn}_{31.5}\text{Ga}_{18.5}$ .

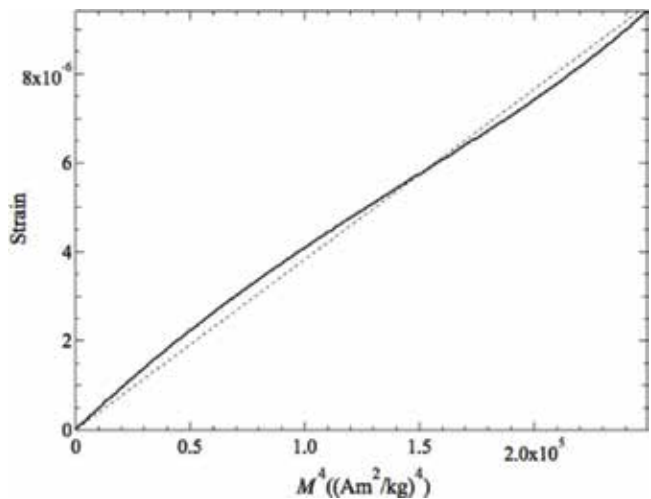
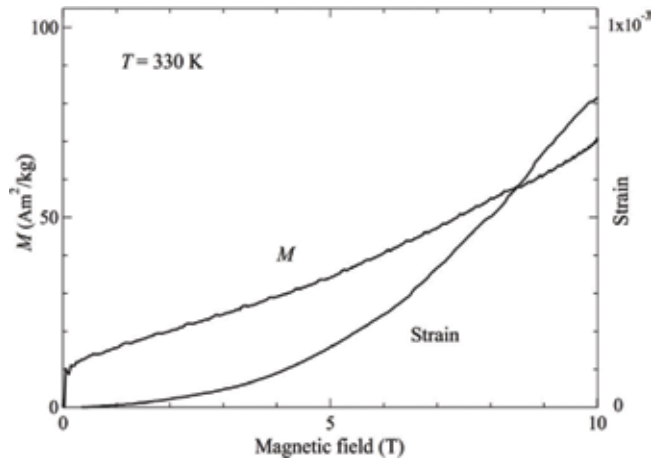
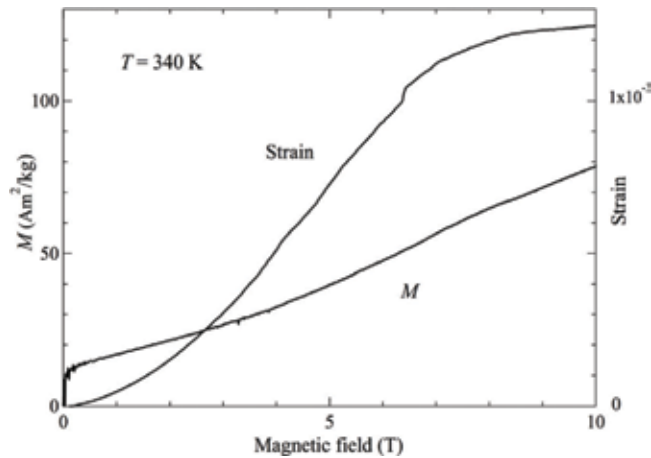


Figure 7. The plot of the magnetostriction against  $M^4$  at 263 K for  $\text{Ni}_{41}\text{Co}_9\text{Mn}_{31.5}\text{Ga}_{18.5}$ . The dotted line is a fitted linear line.

Further, we investigated the MFIS around the reverse martensitic transition temperature. Figures 8 and 9 show the magnetic field dependences of the magnetization and the MFIS at 330 and 340 K, respectively. These temperatures are around the reverse martensitic transition start temperature. The gradient of the magnetization and magnetostriction has tendencies toward increasing with the magnetic field increases for each temperature. However, the degree of the rate of increase of the magnetostriction is larger than that of the magnetization. From these figures, a correlation between the magnetostriction and magnetization could not be identified. As mentioned in Section 1,  $\text{Ni}_{41}\text{Co}_9\text{Mn}_{31.5}\text{Ga}_{18.5}$  is an itinerant ferromagnet. The magnetostriction is proportional to  $M^4$  at the Curie temperature in the martensite phase.



**Figure 8.** The magnetic field dependences of the magnetization and the MFIS at 330 K for  $\text{Ni}_{41}\text{Co}_9\text{Mn}_{31.5}\text{Ga}_{18.5}$ .



**Figure 9.** The magnetic field dependences of the magnetization and the MFIS at 340 K for  $\text{Ni}_{41}\text{Co}_9\text{Mn}_{31.5}\text{Ga}_{18.5}$ .

Therefore, it is presumed that the MFIS is also conformed to the power law suggested by Takahashi's theory.

**Figure 10** shows the plot of MFIS against  $M^2$  at 330 and 340 K. The dotted lines are linearly fitted lines. These fitted lines did not pass the origin, and the plot was rounded. **Figure 11** shows the plot of MFIS against  $M^4$  at 330 and 340 K. The dotted lines are linearly fitted lines. These fitted lines passed the origin. It is conceivable that these results indicate that the MFIS is proportional to the fourth power of the magnetization,  $M^4$ , which was suggested by Takahashi's theory [27]. It is interesting that the  $M^4$  behavior matures until 7 T at 330 K. At this temperature, magneto-structural transition (reverse martensitic and metamagnetic transition) occurred.

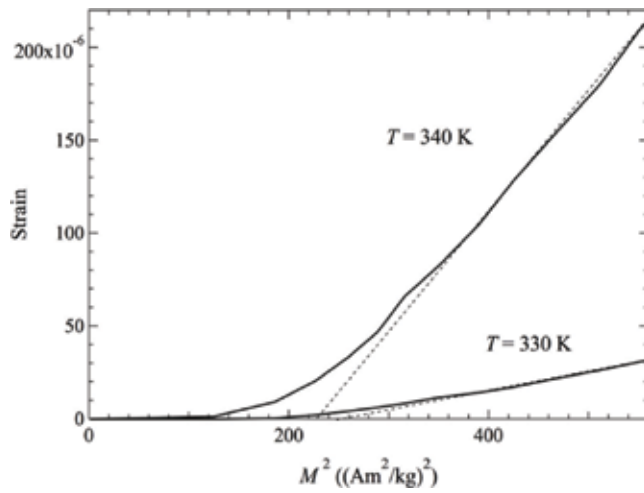


Figure 10. The plot of MFIS against  $M^2$  at 330 and 340 K for  $\text{Ni}_{41}\text{Co}_9\text{Mn}_{31.5}\text{Ga}_{18.5}$ .

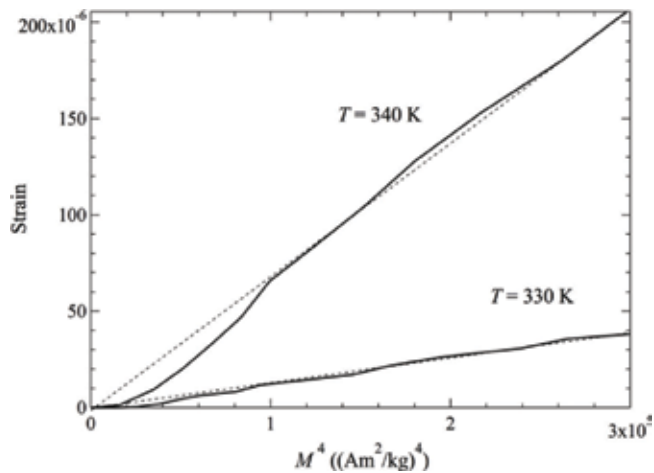
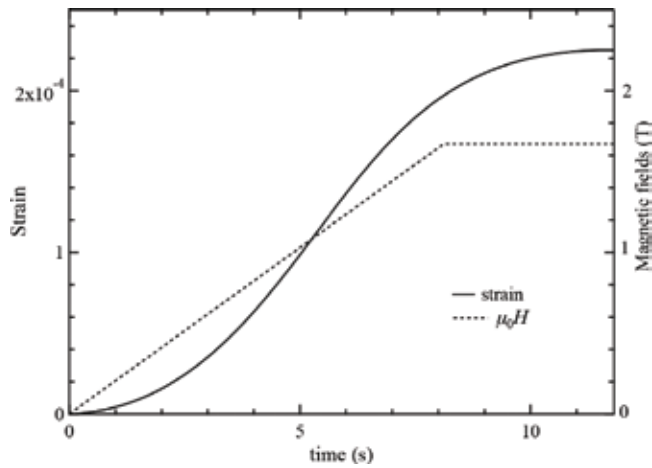


Figure 11. The plot of MFIS against  $M^4$  at 330 and 340 K for  $\text{Ni}_{41}\text{Co}_9\text{Mn}_{31.5}\text{Ga}_{18.5}$ .

### 3.3. The time response of the magnetic field-induced strain of $\text{Ni}_{41}\text{Co}_9\text{Mn}_{31.5}\text{Ga}_{18.5}$

In order to investigate time response of the MFIS, fast speed sweeping of the magnetic fields was performed at 354 K, as shown in **Figure 12**. The applied magnetic field increased from the zero magnetic field to 1.66 T in 8.0 s and under atmospheric pressure. **Figure 13** shows the MFIS, in which the applied magnetic field increased from the zero magnetic field to 1.66 T in 60 s. As for an 8.0-s mode,  $2.2 \times 10^{-4}$  MFIS was observed, which was 80% of the MFIS in a 60-s mode. This indicates that a high-speed transition has occurred on applying magnetic fields.



**Figure 12.** Time dependence of MFIS of  $\text{Ni}_{41}\text{Co}_9\text{Mn}_{31.5}\text{Ga}_{18.5}$  at 354 K in increasing magnetic fields by means of a water-cooled magnet. The applied magnetic field increased from the zero magnetic field to 1.66 T in 8.0 s.

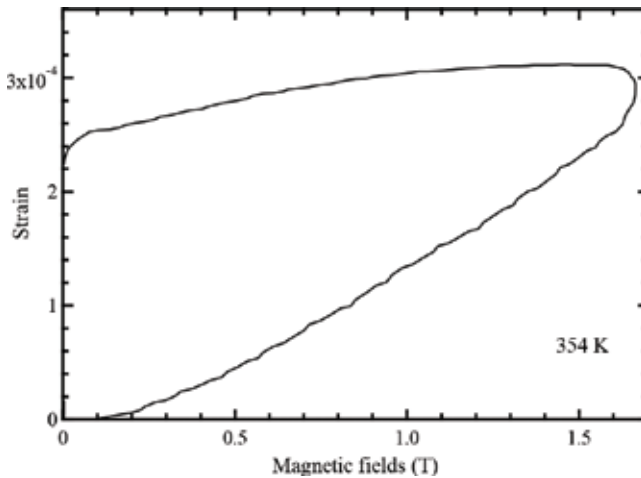


**Figure 13.** MFIS of  $\text{Ni}_{41}\text{Co}_9\text{Mn}_{31.5}\text{Ga}_{18.5}$  at 354 K by means of a water-cooled magnet. The applied magnetic field increased from the zero magnetic field to 1.66 T in 60 s.

The MFIS effect occurs at the temperature between room temperature and 370 K; therefore, it is useful for magnetic sensors, or actuators in the high temperature region, *ex.* the engine room in the motor vehicles.

#### 4. Conclusions

In order to investigate the magnetic functionality of polycrystalline metamagnetic Heusler alloy  $\text{Ni}_{41}\text{Co}_9\text{Mn}_{31.5}\text{Ga}_{18.5}$ , magnetic field-induced strain (MFIS) measurements were

performed. Strain gauge was fixed parallel to the long distance direction (4.0 mm) of the sample. The external magnetic field was applied parallel to the long distance direction of the sample, and the elongation of the sample was measured. A 0.12% MFIS was observed at 340 K and 10 T. Strict MFISs between 300 and 370 K were observed. These magneto-structural variances acted in concert with the metamagnetic property observed by the magnetization measurements and magneto-caloric property observed by the caloric measurements in the applied magnetic fields. The MFISs were proportional to the fourth power of the magnetization, and this result is in agreement with Takahashi's spin fluctuation theory of itinerant electron magnetism. The investigation of time response of the MFIS was performed by means of a sweep water-cooled electric magnet, and zero magnetic field to 1.66 T in 8.0 s at 354 K.  $2.2 \times 10^{-4}$  MFIS was observed, which was 80% of the MFIS in a 60-s mode. This indicates that a high-speed transition has occurred on applying magnetic fields.

## Acknowledgements

The authors thank Mr. M. Okamoto for helping prepare equipment for MFIS measuring system. This experimental study was partly performed at High Field Laboratory for Superconducting Materials, Institute for Materials Research, Tohoku University.

## Conflicts of interest

The authors declare no conflict of interest.

## Author details

Takuo Sakon<sup>1\*</sup>, Naoki Fujimoto<sup>1</sup>, Sho Saruki<sup>1</sup>, Takeshi Kanomata<sup>2</sup>, Hiroyuki Nojiri<sup>3</sup> and Yoshiya Adachi<sup>4</sup>

\*Address all correspondence to: [sakon@rins.ryukoku.ac.jp](mailto:sakon@rins.ryukoku.ac.jp)

1 Department of Mechanical and System Engineering, Faculty of Science and Technology, Ryukoku University, Otsu, Shiga, Japan

2 Research Institute for Engineering and Technology, Tohoku Gakuin University, Tagajo, Miyagi, Japan

3 Institute for Materials Research, Tohoku University, Sendai, Miyagi, Japan

4 Graduate School of Science and Engineering, Yamagata University, Yonezawa, Yamagata, Japan

## References

- [1] Ullakko K, Huang JK, Kantner C, O'Handley RC, Kokorin VV. Large magnetic-field-induced strains in  $\text{Ni}_2\text{MnGa}$  single crystals. *Applied Physics Letters*. 1996;**69**:1966
- [2] Webster PJ, Ziebeck KRA, Town SL, Peak MS. Magnetic order and phase transformation in  $\text{Ni}_2\text{MnGa}$ . *Philosophical Magazine B*. 1984;**49**:295
- [3] Brown PJ, Crangle J, Kanomata T, Matsumoto M, Neumann K-U, Ouladdiaf B, Ziebeck KRA. The crystal structure and phase transitions of the magnetic shape memory compound  $\text{Ni}_2\text{MnGa}$ . *Journal of Physics. Condensed Matter*. 2002;**14**:10159
- [4] Pons J, Santamarta R, Chernenko VA, Cesari E. Long-period martensitic structures of Ni-Mn-Ga alloys studied by high-resolution transmission electron microscopy. *Journal of Applied Physics*. 2005;**97**:083516
- [5] Ranjan R, Banik S, Barman SR, Kumar U, Mukhopadhyay PK, Pandey D. Powder X-ray diffraction study of the thermoelastic martensitic transition in  $\text{Ni}_2\text{Mn}_{1.05}\text{Ga}_{0.95}$ . *Physical Review B*. 2006;**74**:224443
- [6] Sakon T, Otsuka K, Matsubayashi J, Watanabe Y, Nishihara H, Sasaki K, Yamashita S, Umetsu RY, Nojiri H, Kanomata T. Magnetic properties of the ferromagnetic shape memory alloy  $\text{Ni}_{50+x}\text{Mn}_{27-x}\text{Ga}_{23}$  in magnetic fields. *Materials*. 2014;**7**:3715
- [7] Sutou Y, Imano Y, Koeda N, Omori T, Kainuma R, Ishida K, Oikawa K. Magnetic and martensitic transformations of  $\text{NiMnX}$  ( $\text{X}=\text{In,Sn,Sb}$ ) ferromagnetic shape memory alloys. *Applied Physics Letters*. 2004;**85**:4358
- [8] Oikawa K, Ito W, Imano Y, Sutou Y, Kainuma R, Ishida K, Okamoto S, Kitakami O, Kanomata T. Effect of magnetic field on martensitic transition of  $\text{Ni}_{46}\text{Mn}_{41}\text{In}_{13}$  Heusler alloy. *Applied Physics Letters*. 2006;**88**:122507
- [9] Umetsu RY, Kainuma R, Amako Y, Taniguchi Y, Kanomata T, Fukushima K, Fujita A, Oikawa K, Ishida K. Mössbauer study on martensite phase in  $\text{Ni}_{50}\text{Mn}_{36.5}\text{Fe}_{0.5}\text{Sn}_{13}$  metamagnetic shape memory alloy. *Applied Physics Letters*. 2008;**93**:042509
- [10] Khovaylo VV, Kanomata T, Tanaka T, Nakashima M, Amako Y, Kainuma R, Umetsu RY, Morito H, Miki H. Magnetic properties of  $\text{Ni}_{50}\text{Mn}_{34.8}\text{In}_{15.2}$  probed by Mössbauer spectroscopy. *Physical Review B*. 2009;**80**:144409
- [11] Kainuma R, Imano Y, Ito W, Morino YSH, Okamoto S, Kitakami O, Oikawa K, Fujita A, Kanomata T, Ishida K. Magnetic-field induced shape recovery by reverse phase transformation. *Nature*. 2006;**439**:957
- [12] Albertini F, Fabbrici S, Paoluzi A, Kamarad J, Arnold Z, Righi L, Solzi M, Porcari G, Pernechele C, Serrate D, Algarabel P. Reverse magnetostructural transitions by Co and In doping  $\text{NiMnGa}$  alloys: Structural, magnetic, and magnetoelastic properties. *Materials Science Forum*. 2011;**684**:151

- [13] Seguí C, Cesari E, Lázpita P. Magnetic properties of martensite in metamagnetic Ni–Co–Mn–Ga alloys. *Journal of Physics D: Applied Physics*. 2016;**49**:165007
- [14] Kamarád J, Kaštil J, Skourski Y, Albertini F, Fabbri S, Arnold Z. Magneto-structural transitions induced at 1.2 K in  $\text{Ni}_2\text{MnGa}$ -based Heusler alloys by high magnetic field up to 60 T. *Materials Research Express*. 2014;**1**:016109
- [15] Seguí C. Effects of the interplay between atomic and magnetic order on the properties of metamagnetic Ni-Co-Mn-Ga shape memory alloys. *Journal of Applied Physics*. 2014;**115**:113903
- [16] Entel P, Gruner ME, Comtesse D, Sokolovskiy VV, Buchelnikov VD. Interacting magnetic cluster-spin glasses and strain glasses in Ni–Mn based Heusler structured intermetallics. *Physica Status Solidi B*. 2014;**251**:2135
- [17] Porcari G, Fabbri S, Pernechele C, Albertini F, Buzzi M, Paoluzi A, Kamarad J, Arnold Z, Solzi M. Reverse magnetostructural transformation and adiabatic temperature change in Co- and In-substituted Ni-Mn-Ga alloys. *Physical Review B*. 2012;**85**:024414
- [18] Segui C, Cesari E. Composition and atomic order effects on the structural and magnetic transformations in ferromagnetic Ni–Co–Mn–Ga shape memory alloys. *Journal of Applied Physics*. 2012;**111**:043914
- [19] Kanomata T, Nunoki S, Endo K, Kataoka M, Nishihara H, Khovaylo VV, Umetsu RY, Shishido T, Nagasako M, Kainuma R, Ziebeck KRA. Phase diagram of the ferromagnetic shape memory alloys  $\text{Ni}_2\text{MnGa}_{1-x}\text{Co}_x$ . *Physical Review B*. 2012;**85**:134421
- [20] Fabbri S, Albertini F, Paoluzi A, Bolzoni F, Cabassi R, Solzi M, Righi L, Calestani G. Reverse magnetostructural transformation in Co-doped NiMnGa multifunctional alloys. *Applied Physics Letters*. 2009;**95**:022508
- [21] Kihara T, Xu X, Ito W, Kainuma R, Adachi Y, Kanomata T, Tokunaga M. Magnetocaloric effects in metamagnetic shape memory alloys. In: *Shape Memory Alloys—Fundamentals and Applications*. Vol. 59-79. Croatia: InTech Publisher, Rijeka; 2017
- [22] Yu SY, Cao ZX, Ma L, Liu GD, Chen JL, Wu GH, Zhang B, Zhang XX. Realization of magnetic field-induced reversible martensitic transformation in NiCoMnGa alloys. *Applied Physics Letters*. 2007;**91**:102507
- [23] Sakon T, Sasaki K, Numakura D, Abe M, Nojiri H, Adachi Y, Kanomata T. Magnetic field-induced transition in Co-doped  $\text{Ni}_{41}\text{Co}_9\text{Mn}_{31.5}\text{Ga}_{18.5}$  Heusler alloy. *Materials Transactions*. 2013;**54**:9
- [24] Sakon T, Adachi Y, Kanomata T. Magneto-structural properties of  $\text{Ni}_2\text{MnGa}$  ferromagnetic shape memory alloy in magnetic fields. *Metals*. 2013;**3**:202
- [25] Sakon T, Kitaoka T, Tanaka K, Nakagawa K, Nojiri H, Adachi Y, Kanomata T. Magnetocaloric and magnetic properties of meta-magnetic Heusler alloy  $\text{Ni}_{41}\text{Co}_9\text{Mn}_{31.5}\text{Ga}_{18.5}$ . In: *Progress in Metallic Alloys*. Rijeka, Croatia: InTech Publisher; 2016. p. 265

- [26] Takahashi Y. Quantum spin fluctuation theory of the magnetic equation of state of weak itinerant-electron ferromagnets. *Journal of Physics: Condensed Matter*. 2001;**13**:6323
- [27] Takahashi Y. *Spin Fluctuation Theory of Itinerant Electron Magnetism*. Berlin/Heidelberg, Germany: Springer-Verlag; 2013
- [28] Sakon T, Saito S, Koyama K, Awaji S, Sato I, Nojima T, Watanabe K, Sato NK. Experimental investigation of giant magnetocrystalline anisotropy of  $UGe_2$ . *Physica Scripta*. 2007;**75**:546
- [29] Matsunaga M, Ishikawa Y, Nakajima T. Magneto-volume effect of the weak itinerant ferromagnet MnSi. *Journal of the Physical Society of Japan*. 1982;**51**:1153
- [30] Techapiesancharoenkij R, Kostamo J, Allen SM, O'Handley RC. Frequency response of acoustic-assisted Ni–Mn–Ga ferromagnetic-shape-memory-alloy actuator. *Journal of Applied Physics*. 2009;**105**:093923
- [31] Gonzalez-Comas A, Obradó E, Mañosa L, Planes A, Chernenko VA, Hattink BJ, Labarta A. Premartensitic and martensitic phase transitions in ferromagnetic  $Ni_2MnGa$ . *Physical Review B*. 1999;**60**:7085
- [32] Khovailo VV, Takagi T, Tani TJ, Levitin RZ, Cherechukin AA, Matsumoto M, Note R. Magnetic properties of  $Ni_{2.18}Mn_{0.82}Ga$  Heusler alloys with a coupled magnetostructural transition. *Physical Review B*. 2002;**65**:092410
- [33] Wang Z, Liu J, Jiang C, Xu H. The stress dependence of magnetostriction hysteresis in TbDyFe [110] oriented crystal. *Journal of Applied Physics*. 2011;**109**:123923
- [34] Nishihara H, Komiyama K, Oguro I, Kanomata T, Chernenko V. Magnetization processes near the curie temperatures of the itinerant ferromagnets,  $Ni_2MnGa$  and pure nickel. *Journal of Alloys and Compounds*. 2007;**442**:191-193
- [35] Takahashi Y. On the origin of the curie-Weiss law of the magnetic susceptibility in itinerant electron magnetism. *Journal of the Physical Society of Japan*. 1986;**55**:3533

---

# Aspects Regarding Thermal-Mechanical Fatigue of Shape Memory Alloys

---

Petrică Vizureanu, Dragoș-Cristian Achiței,  
Mirabela-Georgiana Minciună and  
Manuela-Cristina Perju

Additional information is available at the end of the chapter

<http://dx.doi.org/10.5772/intechopen.77991>

---

## Abstract

This chapter presents advanced researches about the using of metallic alloys with shape memory properties in construction and exploitation of parts subjected to combined stress by thermal and mechanical fatigue during their functioning. The shape memory alloys (SMAs) have a series of properties much different from the usual metallic materials. Their main characteristic is recovery/returning from plastic deformation by heating, considering that in some cases at temperature changing, the shape modification is reversible. In the case of parts made from SMA, which work in conditions by thermal and mechanical stresses and temperature variations, the resistance evaluation at thermal and mechanical fatigue is absolutely necessary. Like researching domain, regarding thermal and mechanical fatigue behavior, it was selected the shape memory Cu-based alloy. The achieved researches, concerning methodology, investigation equipment, experimental results, allow evaluating and estimating the shape memory properties. Losing the shape memory properties of SMA, in requested conditions, namely amnesia, so to the calculation of fatigue resistance must be taken into account by this fundamental property. The expression of the fatigue state, through losing the memorizing capacity, represents a designing indicator, which ensures the guaranty of properties in fatigue conditions, through applying of fatigue cycles. To determine the fatigue resistance of SMA was necessary specific requests. The properties are guaranteed for a certain number of fatigue cycles. The experimental data, presented in this chapter, offer to scientists some information about the SMAs, Cu-based. These data can be used in designing and manufacturing of new parts for different devices.

**Keywords:** shape memory alloys, properties, shape memory effect, thermal and mechanical fatigue, Cu-based alloy

---

## 1. Introduction

The SMAs present some properties which are not found to metallic alloys used in practice. Characteristic to these alloys it is the capacity to change the geometric shape at temperature modification. After heating up to a imposed temperature, the part is cooled until ambient temperature and returns to his initial shape. In some conditions, the shape changing can be reversible and the material can memorize two geometric shapes: the shape from high temperature (hot shape) and the shape from low temperature (cold shape). The shape changing is realized due to shape memory effect (SME). Through SME, the alloy can do mechanical work in the passing time from cold shape to hot shape.

SMAs can be classified, according to the alloying elements, in following classes: Nickel-based alloys, Copper-based alloys, Iron-based alloys, and Noble Metals-based alloys, Exotic alloys. Copper-based alloys, like Cu Al, CuAlNi, AuCd, NiAl, CuZn, CuZnAl are named  $\beta$  phase alloys. There are numerous types of SMAs, but most of them have high manufacturing costs due to noble or rare metals from composition or to complex obtaining technology. Interest presents NiTi, CuZnAl, CuAlNi alloys which are used in various applications. The most important shape memory phenomena are: (1) pseudo-elastic or pseudo elasticity effect (PSE); (2) shape memory simple effect (SME); (3) double sense shape memory effect (DSSME); and (4) vibrations damping effect.

A less studied chapter is the behavior of these alloys at thermal fatigue and that is because SMA can work: with free return, with retained return, with manufacturing of mechanical work, and pseudo-elasticity. In each of these cases, the parts of SMAs will be heated and then cooled to obtain the proposed goal. Between the hot shape and the cold shape of SMA, there exists a difference of energy. The change reversibility of the two shapes stays at the base of many applications. In this case, the reproducibility of the two shapes has a high importance. After a certain number of functioning cycles, the reproducibility of the two shapes is affected, so does the shape memory property.

Nowadays, some SMAs have usages in domains like:

- aerospace and naval: flaps for aircrafts, solar panels benders for Hubble telescope or Clementine satellite;
- robotics: devices for channel drainage, actuators for tasks manipulation robots;
- medical: medical instruments, crack bones restoration clamps, coronary dilators, glasses frames, locomotor prostheses, arches for dental corrections, stents, brain spatulas;
- others: fire extinguishers, automatic sprinklers, pipe couplings, disassembly devices, automotive thermostats, filter holders, gas switches, solar actuators, steam valves, and vibration dampers.

## 2. Mechanical fatigue phenomena at SMA

The SMA from the construction of some installations is subjected to mechanical loads and also thermal loads. The SME supposes the existence of two structural states, with different mechanical

properties, in reduced temperature frame (cca. 15–30°C). Although in the two structural states (martensitic and austenitic), the alloy has certain properties of mechanical resistance, his basic function is to memorize. The loss of memory properties of the alloy, in certain conditions of loads, carries the names of *amnesia*. To keeping of the material integrity in load conditions is necessary the knowledge of the fatigue resistance both of the martensitic state and also the austenitic state. If the SMA element breaks during the load, then the fatigue resistance condition is not accomplished. In these conditions, the value of fatigue resistance will be smaller than the fatigue resistance values of the two structural states.

**Mechanical fatigue resistance** is defined through the minimal value of recovered deformation, after a certain number of usage cycles. Determining this size can be realized through different ways of loads, but the most precise is the stretching load. Considering that the shape memory properties are evaluated by the values of recovered deformation, this will be the function which characterizes the material. The basis method for results interpretation of the fatigue resistance is  $\sigma(N)$  diagram, named Wohler curve, in which  $\sigma$  represents the maximum amplitude of alternative load until breakage, after a certain number of cycles. This method can be applied to SMA, both in martensitic state and in austenitic state, characterizing the material resistance in the two states. The attempt consists in deformation in martensitic state at a determined value and its recovery through heating in austenitic domain, by an N number, as long as this value is kept. If the breakage is produced, the fatigue resistance condition is not accomplished. A cycle of fatigue load attempts must contain the following steps: (1) memory imprint at maximum limit or recovery deformation; (2) memory education through a number of cycles at maximum limit deformation; (3) demanding at tensions below the realization tension of memory deformation; (4) heating with the maintaining of the load tension; (5) cooling; (6) after a number of cycles, the recovered deformation value is measured. The diagram which contain variation curves of memory capacity according to the number of memory cycles and work load is presented in **Figure 1**.

There are many fatigue loading types according to the exploitation conditions.

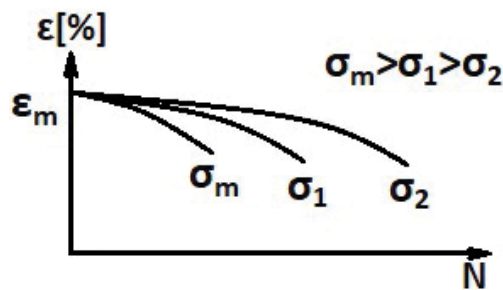


**Figure 1.** Fatigue under load diagram of CuZnAl alloy:  $\epsilon_m$ —recovered deformation;  $\sigma_m$ —memory imprint load;  $\sigma_1$ ,  $\sigma_2$ —loading tensions.

### 3. Fatigue solicitation with free recovery of deformation

This type of fatigue resistance property is guaranteed by the SMA producers. The function of these alloys being the recovered deformation and the variable is the number of memory cycles. If memory imprint deformation is higher, the recovery deformation is higher, but the number of exploitation cycles is reduced. The most encountered fatigue solicitation is solicitation with constant keeping of load during the test.

This type of load is found in the practice at a mechanical system with SMA element, which lifts a weight. The maximum load admitted is the one corresponding to the maximum memorized deformation. The value of free recovery deformation depends on the produced deformation in cold state (martensitic) and the constant load applied. The value of deformation produced by the constant load can be different throughout the test cycles.

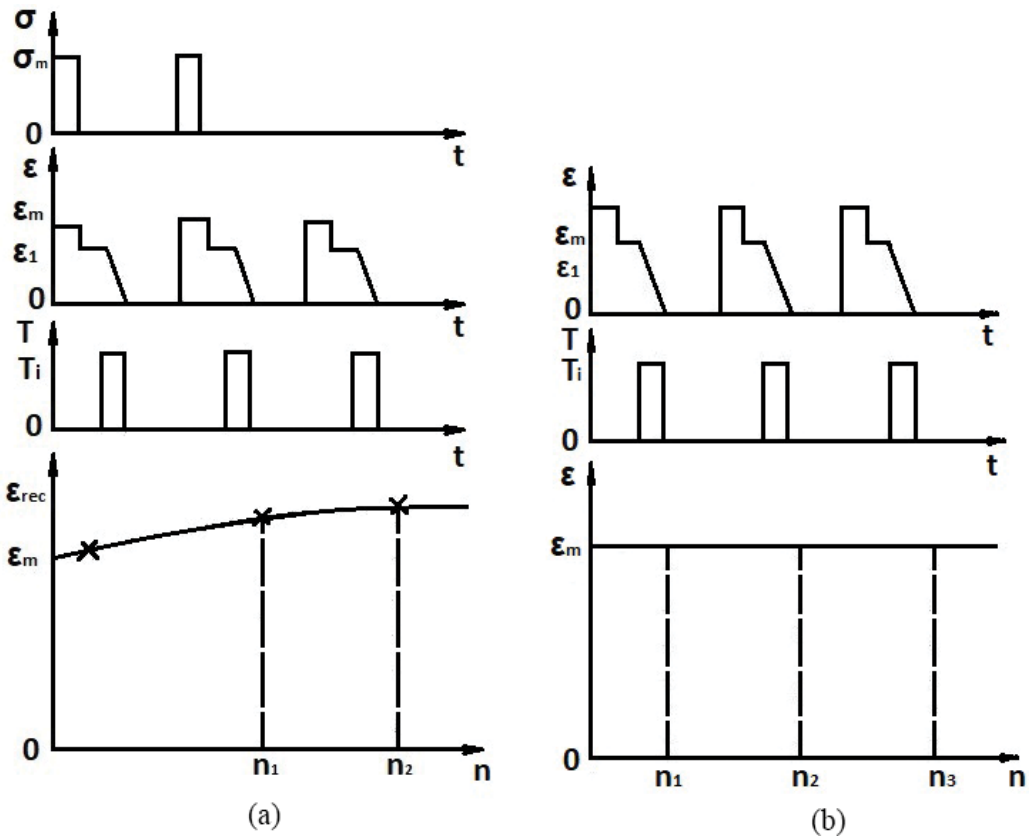


**Figure 2.** The graphic of fatigue test with constant load keeping (a) and constant deformation keeping (b):  $\sigma_m$ —load tension;  $\epsilon_m$ —maximum memory deformation;  $\epsilon$ —elastic recovery;  $T_i$ —temperature of heating cycle;  $\epsilon_{rec}$ —recovery deformation;  $n$ —number of load cycles.

The fatigue tests are proceeding at the determination of the maximum memory effect through traction and dilatometry, in order to establish both maximum load deformation, and also the corresponding tension of this deformation.

The establishment of the thermal cycle temperature is based on critical transformation temperatures. The test can be done on a specialized traction machine, provided with load and heat programmer. The test can be done at load or deformation values below the maximum memorizing value.

The grippers of sample in traction machine must allow the release adjustment of the sample with resulted remanent deformation, which is recovered through a later heating. From the diagram (Figure 2a), it results that every values are synchronized in time through repeating the fatigue test cycle.

In addition, solicitation at fatigue with constant keeping of deformation is found in the practice (Figure 2b) at mechanical systems with memory element with contrast spring, with limiter. The admitted maximum value of deformation corresponded to maximum memorizing deformation.

#### 4. Solicitation at fatigue with recovery under load of recovery deformation

Often, the SMA element from a device does not deform freely; it makes a mechanical work in memory recovery period. Because of that, the fatigue test with free recovery is not matching

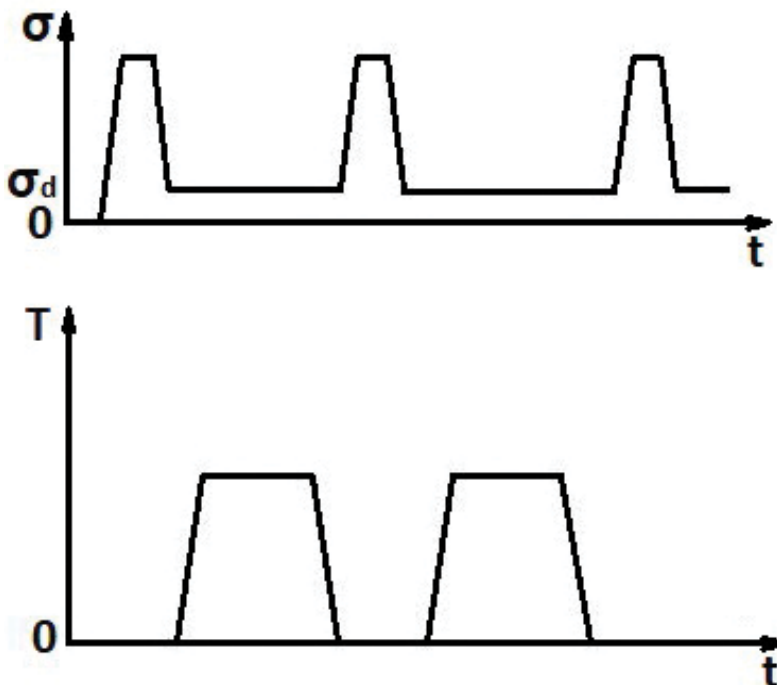


Figure 3. Load cycle ( $\sigma$ ) and thermal cycle ( $T$ ) for fatigue testing under load:  $\sigma_d$ —load in the time of shape recovery.

with the exploitation conditions. For determination of fatigue resistance in these conditions, the traction machine must be provided with a special program for load cycle (Figure 3).

Imprint tension of the cold shape ( $\sigma$ ) must not exceed the maximum memory deformation, and the tension in the recovery period of the shape must be constant. The number of test cycles is determined after the sample breakage or after the loss a certain of memory capacity, determined through dilatometry. The determination involves a large number of samples and high volume of attempts. The graphic of fatigue resistance is compound from a family of curves.

**Thermal fatigue** represents the loss of some properties under the influence of a number of thermal cycles. In the case of SMA, the loss of memory properties is pursued. The application domain of thermal cycles must be contained in transformation critical points area, where the

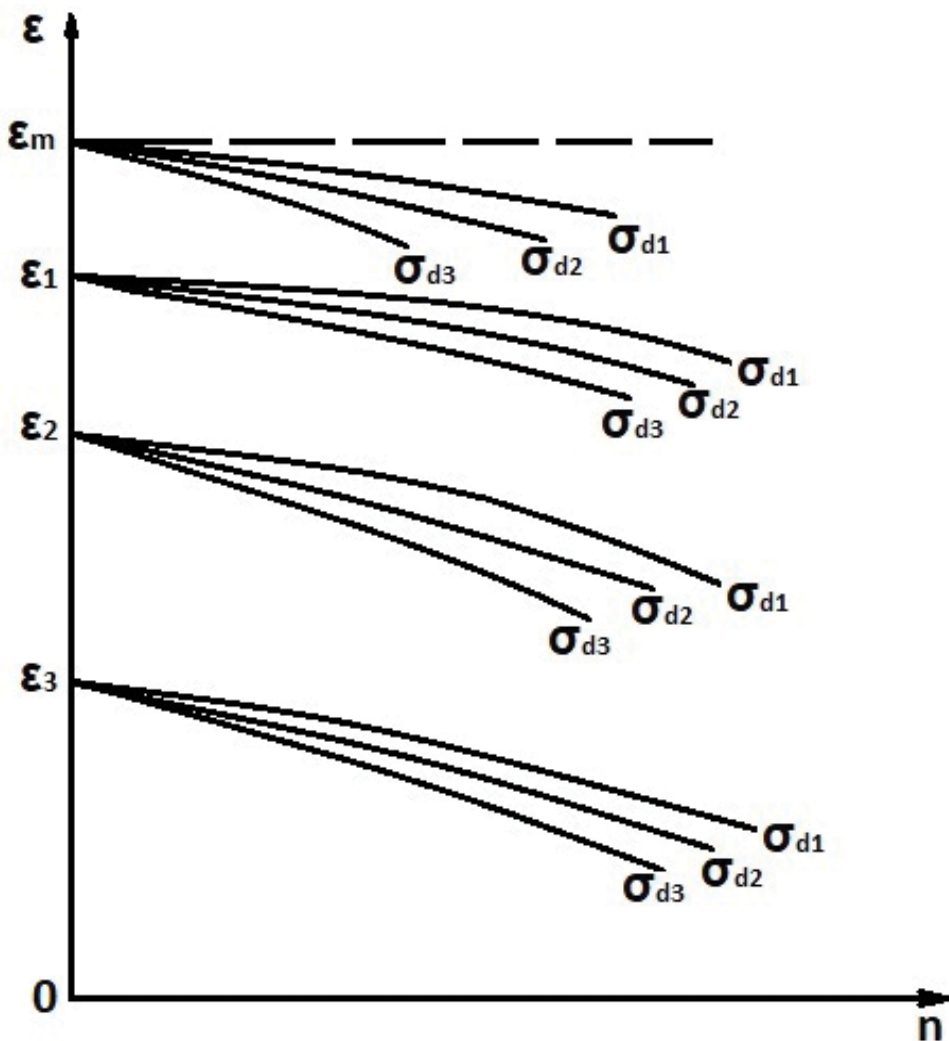


Figure 4. Graphic of fatigue test with recovery under load of deformation recovery.

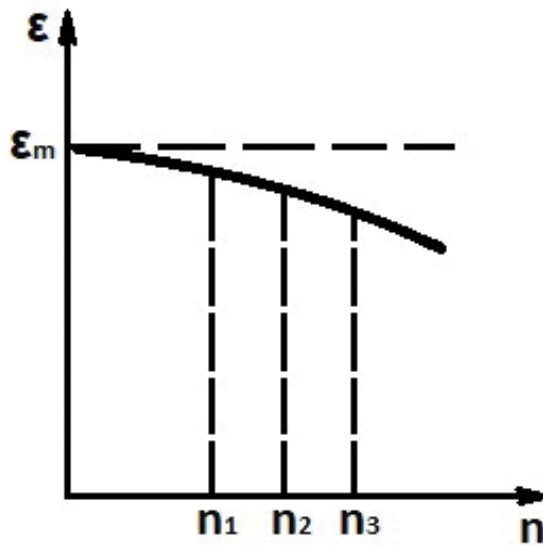


Figure 5. Diagram of thermal fatigue resistance.

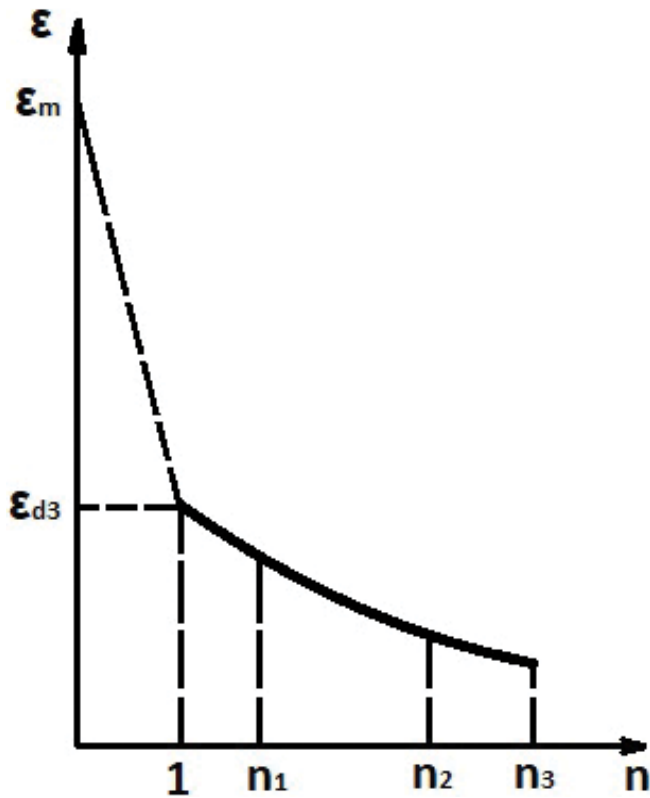


Figure 6. Thermal fatigue of the double sense memory component of a SMA:  $\epsilon_{ds}$ —double sense recovery deformation.

memory property manifests. The test for the determination of this property consists in determination of maximum recovery deformation, after a number of applied thermal cycles (**Figure 3**).

To determine the thermal fatigue of a SMA, a traction deformation ( $\epsilon_m$ ) is performed, after is subjected to a number heating and cooling cycles, without load, and then it is loaded to traction with the same deformation ( $\epsilon_m$ ) and is checked through thermal dilatometry the recovery deformation through heating (**Figure 4**).

Taking into account the precipitation produced through aging, the value of recovery deformation will decrease. At traction load for a remanent deformation ( $\epsilon_m$ ), the elastic recovery should be taken into account.

Depending on the number of points needed on the thermal fatigue diagram, a specific number of samples are subjected to thermal cycles. Then a sample is extracted and subjected to dilatometric test after a deformation ( $\epsilon_m$ ). Considering that the SMA has double sense component, a test of memory degradation through thermal fatigue (**Figure 5**) can be done.

For this purpose, the deformed sample with  $\epsilon_m$  value is subjected to thermal cycles on dilatometer following the recovery deformation value without load (**Figure 6**).

The heating range of the heating cycle must contain the critical points. Through this method, it is measured the memory component from heating process through free recovery and the deformation component at cooling. To determine, this property is used a single sample.

## 5. SMAs fatigue

In the case of a device in which the memory element makes double sense shape memory effect (DSSME) in the system, fatigue resistance limit is defined through the number of cycles until the recovery load decreases at a minimum value (usually 70% from initial value).

SMA can present various phenomena of irreversible deterioration of microstructure and which define specific categories of fatigue. Therefore, in the case of conventional behavior and superelasticity, although there is a difference because of martensitic transformation induced under load, the same type of mechanical fatigue occurs. In the case of education through DSSME, if the applied load is maintained constantly, the fatigue phenomenon is thermal. In the case when the applied load is modifying SME, thermal-mechanical fatigue appears.

Mechanical fatigue involves breaking cracks in four stages: (1) defects accumulation; (2) cracks formation; (3) cracks propagation, in stationary and unsteady regime; (4) final breaking.

On the other hand, when more different SMAs, CuZnAl type, are mechanically educated at room temperature until the same load, was found that the alloys have the resistance to mechanical fatigue lower their  $M_s$  are lower. For SMAs, CuZnAl type, the resistance to mechanical fatigue is higher in a martensitic state. This fact is explained by the high fragility of austenite grains limits, that is a particularity of SMAs, CuZnAl type.

To increase the resistance to mechanical fatigue, is applied a hot rolling, followed a quenching in water, through the grains limits gets an irregular shape. During mechanical education, this shape is recovering, absorbing an extra energy, thanks to which the tenacity of the limits is improved. The main method of enhancing the resistance at mechanical fatigue of SMA is grains finishing. The thermal fatigue is tied especially by the irreversible forming of defects, which leads to a considerable hardening in the case of a binary, biphasic brass (Cu-40%Zn).

In the case of CuZnAl SMA, the mechanical education affects the critical temperatures of transformation, but in much lower ways than the thermal one. The influences of the two types of education are opposite, such that the thermal education strongly reduced the temperature hysteresis, and the mechanical education accentuate it, but very lightly.

**Fatigue cracking** is the phenomenon which leads to breakage at a repeated or fluctuating load, which is smaller than the elastic material load. Fatigue breaking is progressive, at the beginning there are small cracks, which increase under the action of fluctuant loads.

The place where the cracking begins is never extended at more than 2–5 grains around starting point [1]. The location of breaking beginning is dictated by the loads concentration and can be extremely diverse as a position and hard to distinguish in the successive stages of the propagation or increase cracking. The location of breaking beginning is placed in a parallel plan with the direction of shear load. At continuous repetitive loads, the cracks direction is changed perpendicular to the direction of elastic load. After which the initial crack is formed, it becomes a load concentrator, which tends to drive the crack deeper in metal with every repetition of load.

The local loads at the pick of the cracking are extremely high because the cracking and any open crack causes the deepening of the crack. The striations are really thin and it appears at a certain time and although they a certain shape, specific to the breakage through thermal fatigue. At the propagation of fatigue cracking, a continuous reducing of section area is observed, which weakens the material until in the end the breakage is complete. In the end, the breakage can be ductile or fragile or a combination between the two.

## 6. Causes of properties degradation

The SMAs are very sensitive at fatigue. In addition to the phenomena encountered at classic crystalline materials, the SMAs have additional mechanisms tied to phase change which characterized it. These mechanisms are regrouped in a way of thermal fatigue and three ways of mechanical fatigue, which are defined in **Table 1**.

In most of the applications, according temperatures, applied load, imposed deformation and  $M_s$  transformation temperature, the various mechanisms which control the fatigue process are combined and the phenomenon becomes very complex.

**Improving life and breaking of SMAs.** The break type depends on the application mode of mechanical fatigue. At superelasticity, the break is generally intergranular. The improving life

of these alloys imposes to reduce the internal tensions between grains and increasing their resistance to cracking.

To obtain these results, the following factors must be realized: (1) creating a rolling texture, which reducing the orientation differences between grains; (2) possibility to obtain of plastic deformation at grains limit level; (3) heat treatment to reduce the grains size and phase uniformization of structure; (4) decreasing of the martensite plates (**Table 2**).

Regarding the standard chemical composition and the values of specific mechanical characteristics of SMAs, Cu-based alloy, little information is found. Some specific conditions to obtain SMAs are distinguishing: (1) chemical compositions which variants between very tied limits; (2) obtaining of alloy from high purity components with very strict limitation of impurities; (3) low physical and chemical anisotropy in the alloy volume, and (4) optimal correlation of elaboration and thermal-mechanical treatment parameters. Most of the SMAs obtaining method contain three steps: (1) elaboration-forging; (2) primary heat treatment; (3) obtaining of hot and cold shapes.

Analyzing (1) SMAs types, (2) shape memory properties, and (3) obtaining costs were chosen for the study of the thermo-mechanical fatigue on Cu-based alloys. Between the Cu-based alloys, CuZnAl types were chosen, that is,  $\text{Cu}_{75}\text{Zn}_{18}\text{Al}_6$ .

The thermal-mechanical fatigue phenomenon of SMA cannot be avoided. Although in the two structural states (martensite and austenite), the alloy has certain properties of mechanical

Fatigue	$T < M_f$	$A_f < T < M_s$	$T > M_s$
Mechanical	Reorient of martensite variants	Martensite formation through contraction	Classic fatigue in austenitic state
Thermal	Thermal education in stability domain of the two phases		

**Table 1.** Ways of thermal and mechanical fatigue at SMA.

Solicitation cycles	CuZnAl	NiTi	CuAlNi	
			Policristalyne	Monocristalyne
$s^{\max}$ ( $N = 10^5$ cycles)	75 MPa	250 MPa	100 MPa	150 MPa
$e^{\max}$ simple effect	4%	8%	5%	10%
$N = 10^3$	2%	3%	3%	6%
$N = 10^4$	1%	2%	2%	4%
$e^{\max}$ double effect	2%	5%	2%	—
$N = 10^2$	1%	—	1.2%	—
$N = 10^3$	0.8%	1%	0.8%	—

$s^{\max}$ —maximum load;  $e^{\max}$ —maximum effect; N—cycles number of load.

**Table 2.** Values of fatigue resistance coefficients.

resistance, its basic function is memorizing. The fatigue resistance will consider the loss of the memorizing capacity in cyclic load conditions.

The equipment used for testing the resistance at mechanical fatigue, reproduces the loads at which are subjects the parts in exploitation. The equipments used for testing the resistance at thermal fatigue study the modifications that appear in a sample subjected to a thermal load (heating-cooling).

The study of optimal exploitation time of an parts made from SMAs is necessary for the knowledge of the exploitation time in maximum parameters. This study proposes the necessity to realize thermal and mechanical combined loads for fatigue tests. The samples for the tests are samples with standard dimensions and will be subjected to traction, being caught between grippers. The samples load is made by mechanical means (**Figure 7**).

According to the weights attached to lever system, the sample will be loaded with a load directly proportionally with the weight placed (4.5 kg). The proportionality is obtained through a lever system. The alloy has certain mechanical resistance properties, which can be altered through fatigue in cyclic exploitation conditions. The sample will be heated and cooled cyclic, in 40–150°C temperatures interval, with an installation which blow hot or cold air. The heating time is 4 min and cooling time is 2 min. The cycle's number (N) needed for a sample is  $10^3$ – $10^4$  cycles, and the exploitation time for realizing of these cycles is in the order of tens of hours.

An important problem of this installation is the synchronization of thermal cycle with mechanical cycle, an important fact in the case of SMAs and the study of their thermal-mechanical fatigue phenomenon.

The prototype installation for thermal-mechanical fatigue tests (**Figure 8**) respect the principles of functioning for testing installation at mechanical and thermal fatigue. The control of parameters and result recording are made automatically with computer and XMEM original software.

### 1. Elaboration of shape memory alloy

Elaboration is a first step in obtaining process of shape memory alloy. The elaboration procedures are different according to the alloy type or the tracked properties. The alloy elaboration was made in an induction furnace, with graphite crucible (**Figure 9a**), using high purity alloying elements.

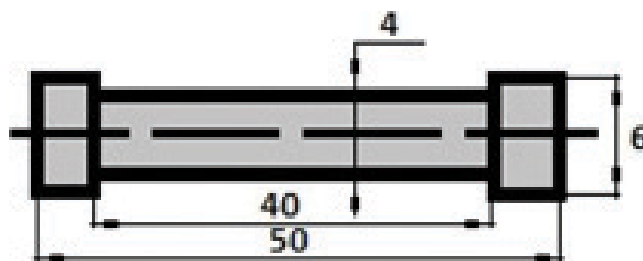


**Figure 7.** Shape and dimensions of samples used for experiments.

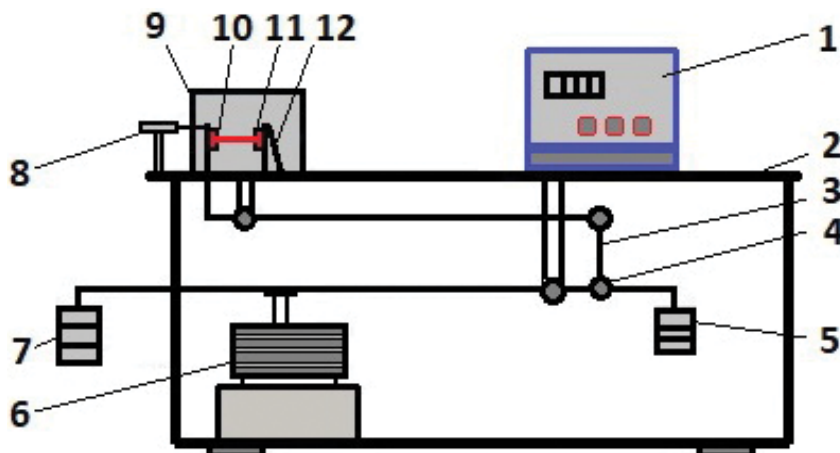


**Figure 8.** The prototype installation for thermal-mechanical fatigue tests. (1) control panel; (2) rigid metallic frame; (3, 4) bearings and levers system for mechanical load; (5) counter-weight; (6) motor-reducing gear-arm assembly for lift the weights; (7) weights; (8) comparator watch; (9) heating enclosure housing; (10) SMA test sample; (11) grippers; (12) fixed fastening system.

At elaboration temperature, the interaction between metallic charge and furnace atmosphere consist from oxidation reactions or gases dissolution. The elaboration stages are the following: (1) copper introducing in crucible; (2) after copper melting, aluminum adding; (3) zinc adding.

The melting temperature is limited to 1200°C to reduce the evaporation losses. There is a risk of zinc burning and dissolution of resulted gases in the metallic bath. The protection of metallic bath against oxidation was made with borax ( $\text{Na}_2\text{B}_4\text{O}_7$ ).

After homogenization of alloy in graphite crucible (**Figure 9a**), heating in induction furnace with high frequencies (8000 Hz), the alloy is casted in a metallic die (**Figure 9b**) and was obtained the samples (**Figure 9c**).

## 2. Experimental determination of chemical composition

The analysis of chemical composition on cast samples was made on Foundry Masters spectrometer, 01 J0013 type [4]. With WASLAB software and the extensible calibration programs, is obtained an analysis bulletin, which present the determined values (**Table 3**).

Through the quantitative spectral analysis, we want to have the certainty that the resulted percentages of alloying elements from sample are in the limits imposed for charge. In the calculation of charge was considered that impurifying elements exist: Fe (0.021–0.033), Co (<0.015), Si (0.009–0.026), Ni (<0.005), Ag (0.002), As (0.008–0.01), Mn (0.02–0.08).

## 3. Diffractometric analysis of sample in cast state

The diffractometric analysis was made on X-ray diffractometer, XPert Pro Philips Analytical type [5]. The obtained results are presented in **Figure 10**.



**Figure 9.** (a) Graphite crucible; (b) metallic dies for SMA casting; (c) cast samples.

Cu*	Zn*	Al*	Fe	Co	Si	Ni	Ag	As	Mn
75.4	18.6	5.85	0.021	0.015	0.026	0.005	0.002	0.008	0.073

\*Conventional notation of studied alloy— $\text{Cu}_{75}\text{Zn}_{18}\text{Al}_6$ .

**Table 3.** Chemical composition (%).

The presence of chemical compounds is distinguished with the formula:

- copper-zinc  $\text{Cu}_5\text{Zn}_8$  in 53%
- aluminum-copper  $\text{Al}_4\text{Cu}_9$  in 47%

#### 4. Structural analysis of sample in cast state through optical and SEM microscopy

Optical analysis of microstructure for studied alloy was made on a metallographic microscope, AxioObserver D1m type [7]. The SEM microscopy was made on VEGA II LSH microscope, which was coupled with EDX detector, QUANTAX QX2 type [8].

The  $\text{Cu}_{75}\text{Zn}_{18}\text{Al}_6$  alloy presents various types of martensite, with parallel plates, zig-zag and arrow heads (**Figures 11 and 12**).

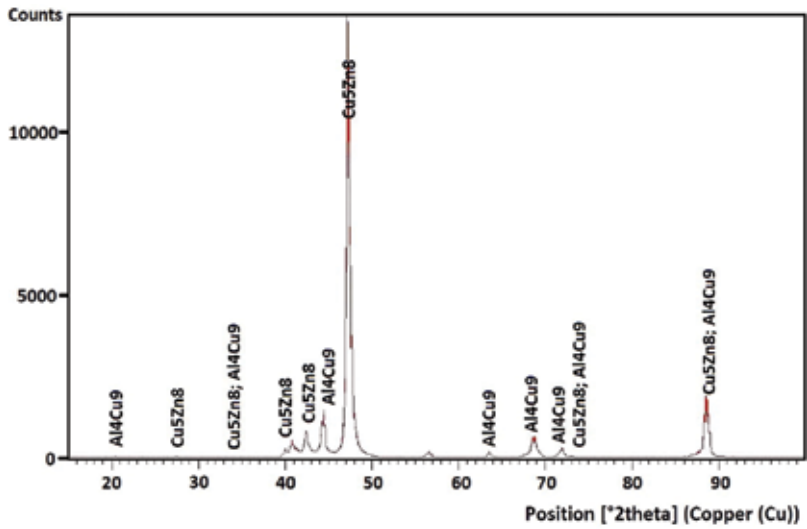


Figure 10. Chemical compounds distribution for Cu<sub>75</sub>Zn<sub>18</sub>Al<sub>6</sub> alloy, in cast state.

### 5. Thermal conductivity analysis of cast sample

The measurements of thermal conductivity were made because the SMAs are used in applications like actuators, fact which impose the correct establish of the values for this coefficient and his mode by electric activation. TCi system [6] determines directly the thermal conductivity and other parameters, for different types of materials: solids, liquids, powders, foams. The achieved analyses are nondestructive, and for tests they are necessary small samples (Table 4).

The Cu<sub>75</sub>Zn<sub>18</sub>Al<sub>6</sub> alloy present a good thermal conductivity in cast state, the medium value is fit in the limits which are specific to the copper alloys casted in parts.

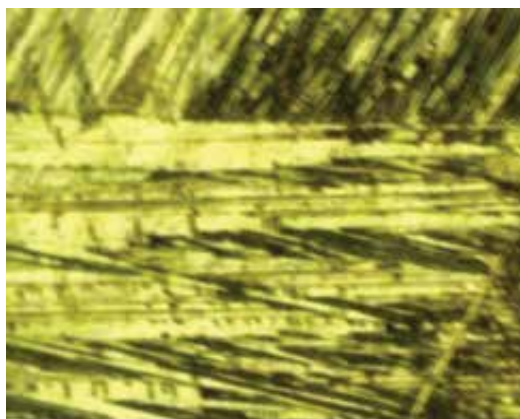
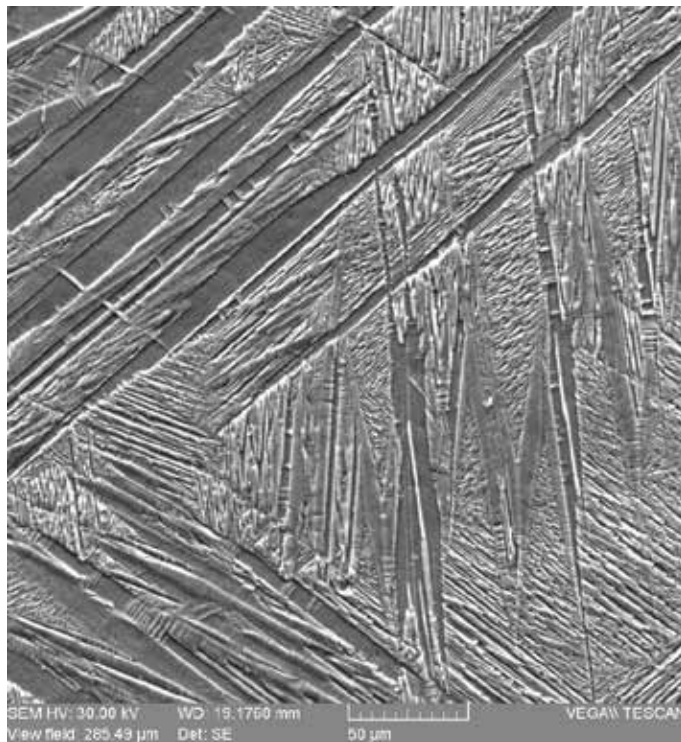


Figure 11. Optical microscopy, cast state, HNO<sub>3</sub> 30% attack, (100×).



**Figure 12.** SEM microscopy, cast state, HNO<sub>3</sub> 30% attack, (1000×).

No.	1	2	3	4	5	6	7	8	9	10
Thermal conductivity (W/m·K)	43.900	41.140	40.450	40.650	40.300	40.310	40.950	40.850	41.050	41.050
Caloric capacity (J/kg·K)	437.750	438.040	438.059	438.059	438.058	438.058	438.054	438.056	438.051	438.052

**Table 4.** Thermal conductivity for sample in cast state.

## 6. Hot plastic deformation

For structure finishing, the cast samples are subjected to a hot plastic deformation. The heating temperatures for plastic deformation is  $850 \pm 10^\circ\text{C}$ , with maintain period by 0.5 h/25 mm thickness of material, to ensure a mono-phasic structure.

The plastic deformation was made in  $850\text{--}800^\circ\text{C}$  thermal interval, what is means the obtaining of deformation grade through repeating the plastic deformation operation (10–20 cycles). **Figure 13c** presents the forged sample during plastic deformation.

## 7. Diffractometric analysis of sample in forged state (**Figure 14**)

The presence of chemical compounds is distinguished with the formula:

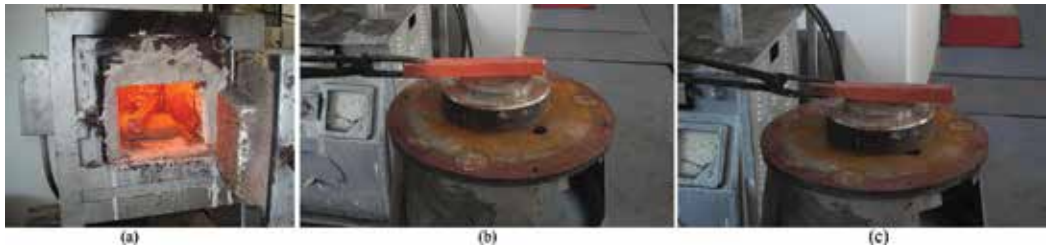


Figure 13. (a) Heating furnace and forged parts; (b) forging of cast; (c) hot forged sample (850–900°C).

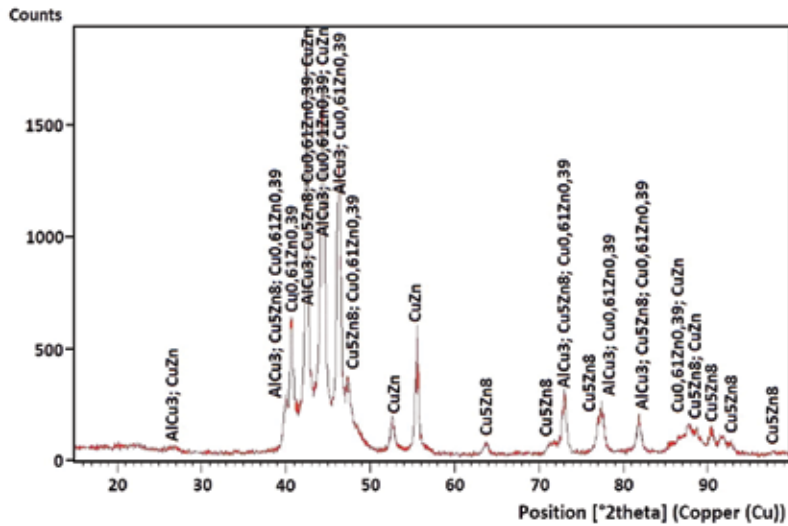


Figure 14. Chemical compounds distribution for Cu<sub>75</sub>Zn<sub>18</sub>Al<sub>6</sub> alloy, in a forged state.

- aluminum-copper AlCu<sub>3</sub> by 20.5%
- copper-zinc Cu<sub>5</sub>Zn<sub>8</sub> by 33.3%
- α-Cu<sub>0.61</sub>Zn<sub>0.39</sub> by 25.6%
- copper-zinc CuZn by 20.6%

8. Structural analysis of sample in forged state through optical and SEM microscopy (Figures 15 and 16)

The same martensitic structure, mixed, with different shapes: parallel plates, arrow head, is found and also in the case of forged sample.

9. Thermal conductivity analysis of samples in forged state (Table 5)

The hot plastic deformation has a lower influence on thermal conductivity; the measured values are falling in specific limits of SMA, based on copper, found in different stages of processing through plastic deformation and obtaining of parts.

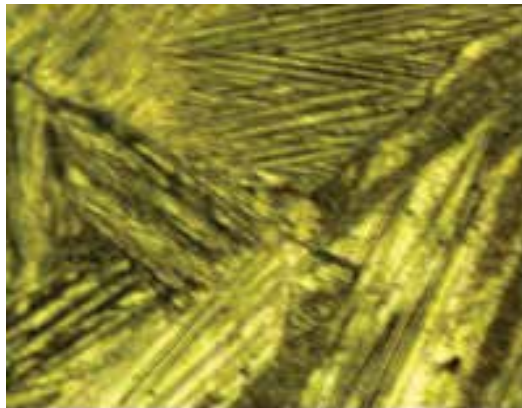


**Figure 15.** Optical microstructure, in forged state, HNO<sub>3</sub> 30% attack, (100×).

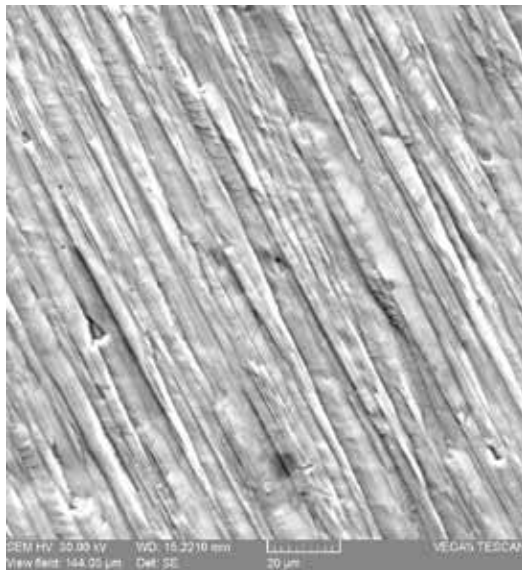


**Figure 16.** SEM microstructure, in forged state, HNO<sub>3</sub> 30% attack, (5000×).

#	1	2	3	4	5	6	7	8	9	10
Thermal conductivity (W/m·K)	39.289	37.880	37.121	36.883	36.492	36.588	36.225	35.968	36.015	35.444
Caloric capacity (J/kg·K)	438.015	437.853	437.713	437.662	437.569	437.592	437.500	437.428	437.442	437.268

**Table 5.** Thermal conductivity for sample in forged state.

### 10. Heat treatment of quenching to put in solution

The forged samples were processed through machining at standard dimensions according to the experimental tests. These samples are subjected to quenching heat treatment. The

parameters of heat treatments are the following: (1) heating with furnace until 800°C; (2) maintaining for temperature uniformization and finishing the structural transformation, for an hour; (3) rapid cooling in water at ambience temperature (**Figures 17 and 18**).

11. Diffractometric analysis of sample in quenched state

The presence of chemical compounds is distinguished with the formula:

- aluminum-copper  $AlCu_3$  by 42.8%
- copper-zinc  $Cu_5Zn_8$  by 51.2%

12. Structural analysis of quenched sample through optical and SEM microscopy

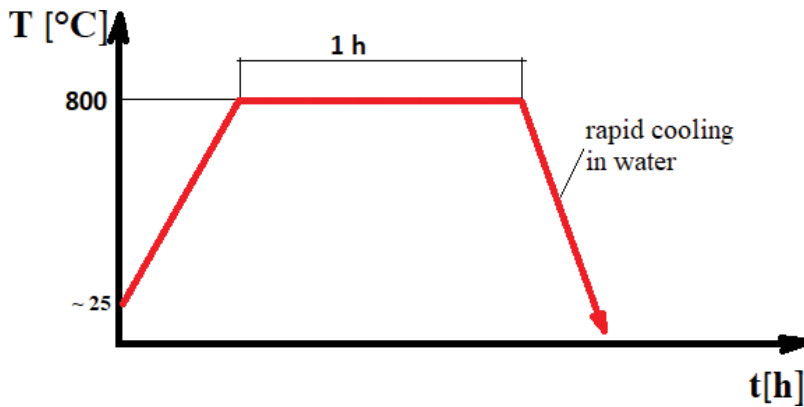


Figure 17. Primary heat treatment: quenching to put into solution.

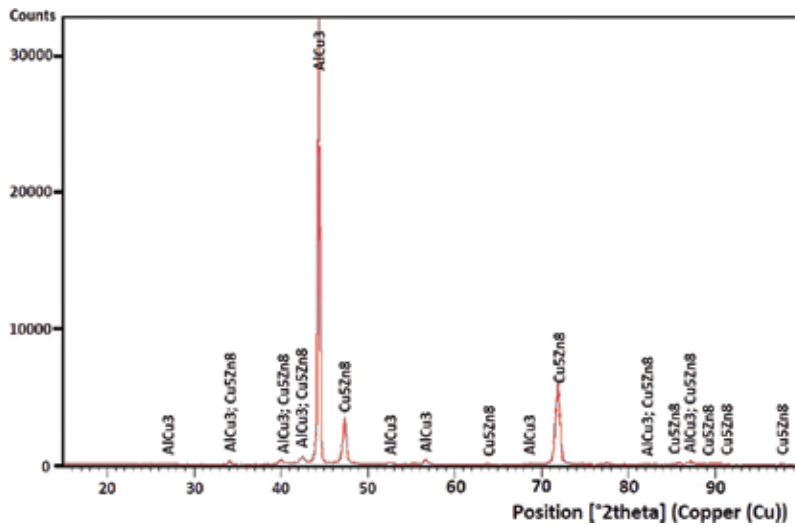


Figure 18. Chemical compounds distribution for  $Cu_{75}Zn_{18}Al_6$  alloy, in quenched state.

The martensitic structure from quenched sample is present, having predominantly the shape of arrow head (**Figure 19**).

13. Thermal conductivity analysis of sample in quenched state (**Table 6**)

The decrease of thermal conductivity for quenched sample more than six times over cast sample or forged sample, transform the SMA in a thermal barrier, following in the heating-cooling process, the stored energy to be used in DSSME goal.

14. Induction of SME—deformation with imposed elongation

After the heat treatment, the samples were subjected to an elongation with 3% deformation grade (**Figure 20**). The controlled elongation was realized on a traction machine, Instron 3382 model [2] (**Table 7**) (**Figure 21**).

15. Checking of SME through dilatometric analysis

The dilatometric analysis records the length modifications for a sample, when it is exposed to a temperature variation. This modification of length can be reversible. Through dilatometric analysis can determine the transformation points in solid states, specific to the analyzed alloy. The determination of these transformation points is important for the applications in which are used parts from SMA, Cu-based.

The dilatometric analysis of  $Cu_{75}Zn_{18}Al_6$  alloy was made on a differential dilatometer, Linseis L75H/1400 model [3]. In the heating time, with a constant heating rate ( $5^{\circ}C/min$ ), the alloy

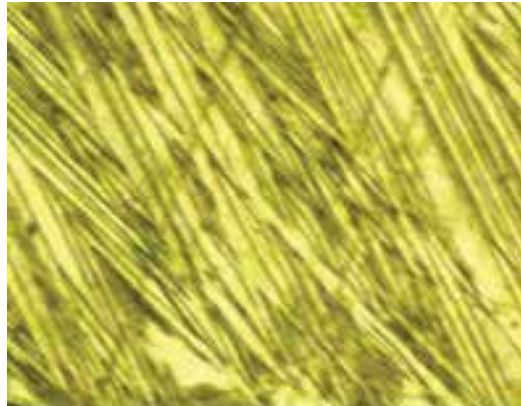


**Figure 19.** Optical microstructure, in quenched state,  $HNO_3$  30% attack, (100 $\times$ ).

#	1	2	3	4	5	6	7	8	9	10
Thermal conductivity (W/m·K)	6892	6613	6407	6333	6211	6142	6324	6265	6179	6178
Caloric capacity (J/kg·K)	403.249	404.328	405.291	405.673	406.355	406.766	405.722	406.045	406.543	406.551

**Table 6.** Thermal conductivity of sample in quenched state.

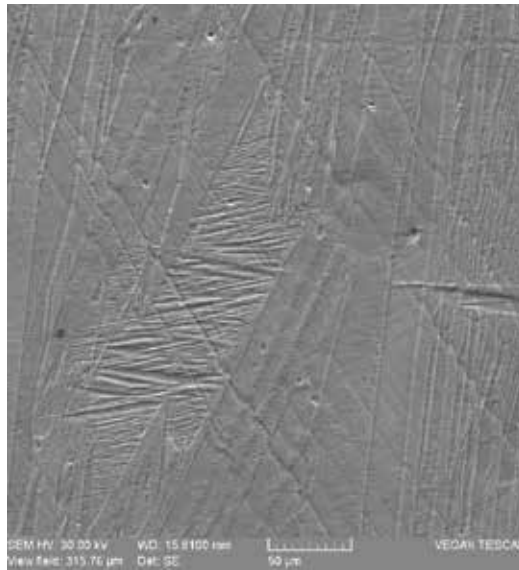


Figure 20. SEM microstructure, in quenched state, HNO<sub>3</sub> 30% attack, (1000×).

Maximum force $F_{max}$ (N)	Young modulus E (MPa)	Maximum load $\sigma_r$ (MPa)	Elongation (%)
3576.16	20908.02	284.58	3

Table 7. Mechanical characteristics.

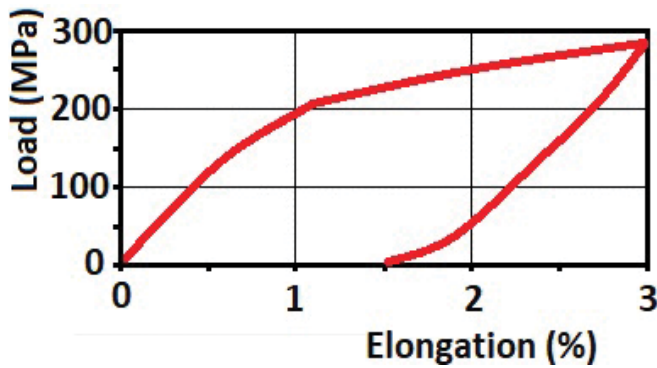
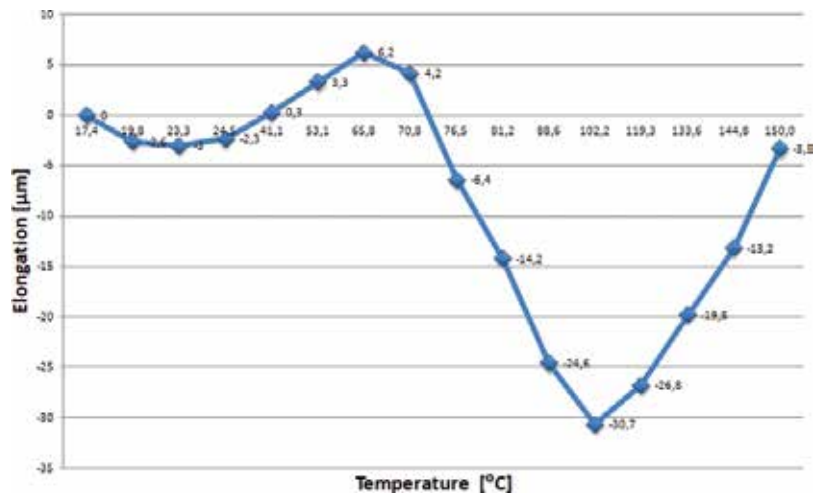


Figure 21. Load-elongation diagram.

presents a contraction phenomenon which starts at the start temperature of martensite-austenite transformation and finishes when the alloy does not present a martensitic structure (Figure 22).

The  $\text{Cu}_{75}\text{Zn}_{18}\text{Al}_6$  alloy presents the martensite-austenite transformation domain between 65.8°C and 102.2°C. The maximum contraction, between two temperature values, is 30.7  $\mu\text{m}$ .



**Figure 22.** Sample dilatogram, after quenching to put in solution and controlled deformation (3% grade), without fatigue cycles.

## 7. Thermal-mechanical fatigue of $\text{Cu}_{75}\text{Zn}_{18}\text{Al}_6$ alloy

### 7.1. Testing conditions

The samples (**Figure 7**) used for thermal-mechanical fatigue tests are falling in dimensional class of samples which can be used for dilatometric analysis (10–50 mm length, 3–6 mm diameter). The experiments were made on a prototype installation (**Figure 8**), designed and special manufactured for these tests. After education, the samples were subjected to a variable number of thermal-mechanical fatigue cycles.

After a certain number of cycles, the samples were analyzed on dilatometer, studying the contraction modifications on the heating time and the variation of temperatures domain for the critical points. With a hot/cold air installation (constructive element from prototype installation), the  $\text{Cu}_{75}\text{Zn}_{18}\text{Al}_6$  sample is heating up to 150°C, and then cooled until 40°C. The heating rate is 15°C/min, and cooling rate is 30°C/min.

The control of testing parameters (heating and cooling parameters, number of cycles, test times) was made with specific software, XMEM. The load to which it was subjected the sample is kept constant for all the thermal-mechanical fatigue tests. Also with XMEM software, was made and synchronization of mechanical load cycle with thermal cycle: when the sample is mechanical loaded, is started the heating. The sample stays under load during the heating time, up to 150°C final temperature. After this moment, the sample is cooled, and the mechanical load is removed, using motor-reducing gear-arm system to lift the weights (**Figure 8**). While the mechanical load is canceled, the sample is cooling until 40°C final temperature.

### 7.2. Experimental results

After an arbitrary number of thermal-mechanical fatigue cycles, the sample is analyzed on dilatometer to record the modifications of shape memory properties, which appear after the thermal-mechanical synchronized cycles.

The conditions for dilatometric analysis are the following: (1) the sample is heating from ambience temperature (25–30°C) up to 150°C; (2) the heating rate for SMA is imposed to 5°C/min; (3) the sample cooling is made in same time with the furnace of dilatometer (the cooling rate is 10°C/min); (4) after cooling the sample is subjected to other number of thermal-mechanical fatigue cycles; (5) with the specific software, can obtain dilatogram with the information about the analyzed SMA (Figures 23–25).

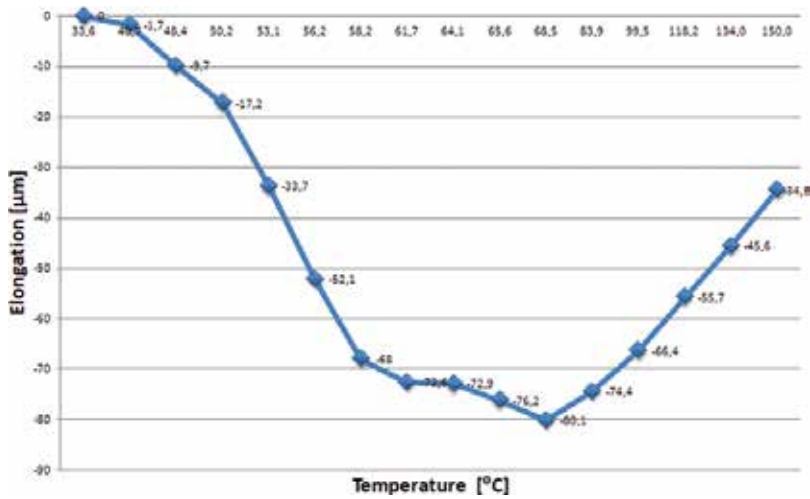


Figure 23. Dilatogram after 100 thermal-mechanical fatigue cycles.

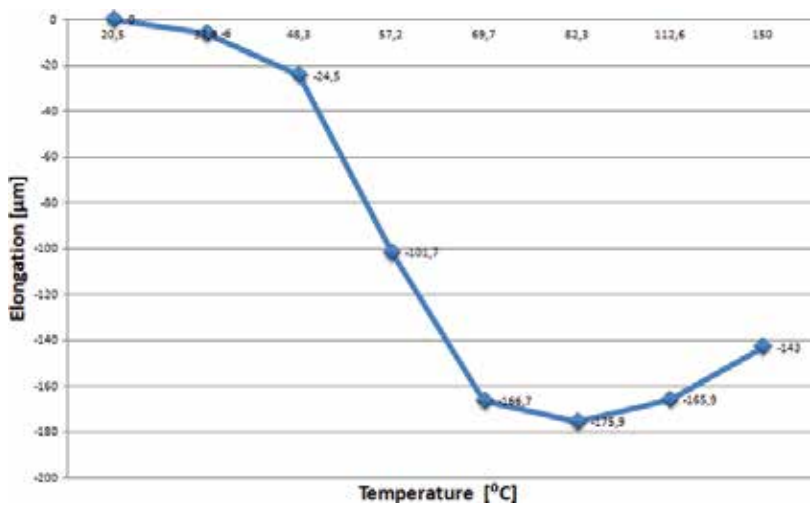


Figure 24. Dilatogram after 6985 thermal-mechanical fatigue cycles.

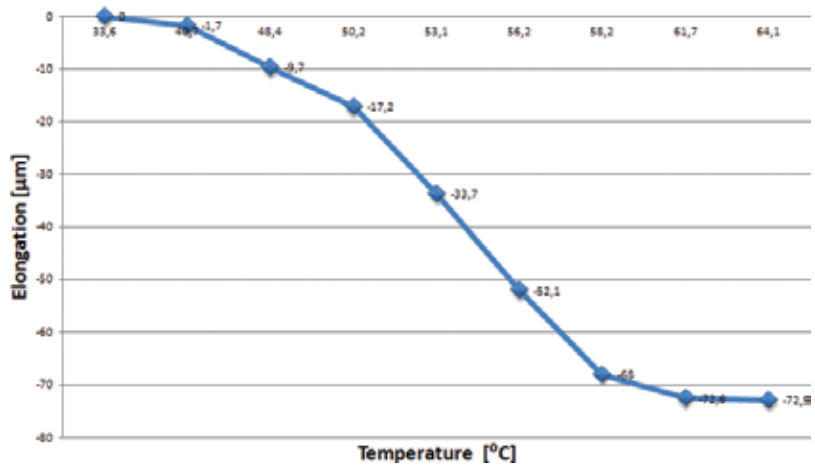


Figure 25. Dilatogram after 12,685 thermal-mechanical fatigue cycles.

Number of load cycles N	Maximum contraction values $\Delta l$ ( $\mu\text{m}$ )	Transformation temperatures ( $^{\circ}\text{C}$ )	
		Ms	Af
0	30.70	65.8	102.2
100	80.10	40.7	99.5
200	79.70	40.2	67.0
300	57.70	42.3	56.8
400	83.80	37.7	68.0
500	71.30	42.0	69.5
600	74.90	44.0	72.2
700	80.00	47.3	72.3
800	88.70	49.2	75.3
900	103.50	45.0	71.7
1000	96.10	47.9	77.0
1100	103.60	40.1	70.2
1200	80.20	48.5	73.3
1328	83.20	45.3	72.3
1667	118.70	39.9	80.1
2131	159.40	37.3	75.9
2680	127.30	43.8	72.2
3293	165.00	36.8	71.3
4103	149.10	42.4	77.5
4582	155.10	42.3	83.8
5758	186.30	42.9	79.8
6958	175.90	33.9	82.3

Number of load cycles N	Maximum contraction values $\Delta l$ ( $\mu\text{m}$ )	Transformation temperatures ( $^{\circ}\text{C}$ )	
		Ms	Af
8068	150.80	37.2	76.7
9355	134.20	29.4	73.3
10,948	123.00	28.5	81.6
11,321	123.70	26.0	73.5
12,209	69.60	28.0	64.0
12,865	97.40	26.6	65.3

Table 8. Measured parameters in fatigue study.

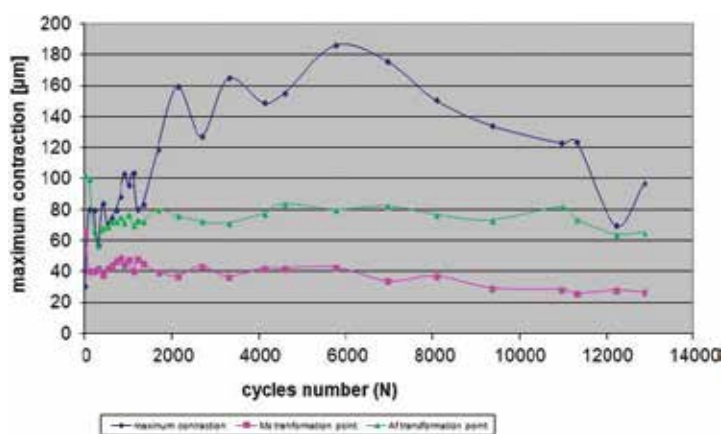


Figure 26. Variation of maximum contraction according the number of load cycles.

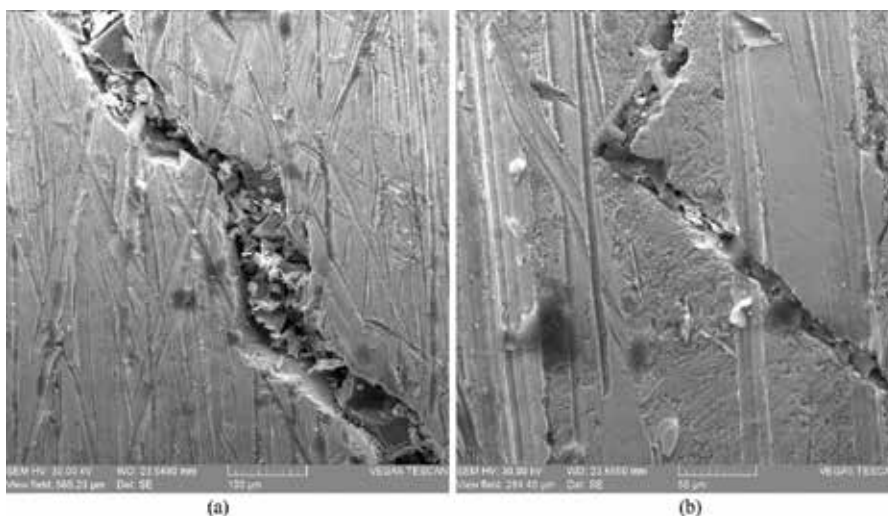


Figure 27. Micro-cracks on sample surface, after 12,865 fatigue cycles: (a) 500 $\times$  and (b) 1000 $\times$ .

Centralizing the maximum contraction values, after various number of thermal-mechanical fatigue cycles, can draw the fatigue curve for  $\text{Cu}_{75}\text{Zn}_{18}\text{Al}_6$  alloy (Table 8) (Figure 26).

After 12,685 thermal-mechanical fatigue cycles, on sample surface appeared some micro-cracks (Figure 27). The experimental tests were stopped. If it continued, these micro-cracks will evolve in the analyzed sample and finally will have his breaking. Figure 27 presents the aspect of micro-cracks, at different magnitudes.

## 8. Conclusions

- The  $\text{Cu}_{75}\text{Zn}_{18}\text{Al}_6$  studied alloy was obtained through classic elaboration, on an induction furnace, using alloying elements with high purity. Any influence in elaboration process, with modifications in percents calculus of alloying elements, can lead to obtaining an alloy with SME. A variation with 1% for aluminum or zinc can modify the critical points.
- For thermal-mechanical fatigue tests of SMA, a prototype installation has been designed and realized. The fatigue tests were completed with dilatometric analysis to highlight the deteriorations of SME.
- The  $\text{Cu}_{75}\text{Zn}_{18}\text{Al}_6$  is a ternary alloy and the structure contains inter-metallic compounds, like  $\text{Cu}_5\text{Zn}_8$  and  $\text{Al}_4\text{Cu}_9$ , for the sample in cast state (Figure 10).
- After a hot plastic deformation (forging at 850–800°C), the structure is finishing and contains the following compounds:  $\text{AlCu}_3$  (20.5%),  $\text{Cu}_5\text{Zn}_8$  (33.3%),  $\alpha\text{-Cu}_{0.61}\text{Zn}_{0.39}$  (25.6%) and  $\text{CuZn}$  (20.6%) (Figure 14).
- After quenching to put into solution, in the structure,  $\text{AlCu}_3$  (42.8%) and  $\text{Cu}_5\text{Zn}_8$  (51.2%) are found (Figure 18).
- Regarding the medium thermal conductivity can remark the following: (1) in cast state: 41.06 [W/m·K]; (2) in forged state: 36.79 [W/m·K]; (3) in quenched state: 6.35 [W/m·K] (Tables 4–6). The decrease of thermal conductivity for quenched sample more than six times over cast sample or forged sample. This fact transform this SMA in a thermal barrier, following in the heating-cooling process, the stored energy can be used in DSSME goal.
- The structure or  $\text{Cu}_{75}\text{Zn}_{18}\text{Al}_6$  alloy was analyzed through optical and SEM microscopy. The microstructures present the modifications of grains orientation and geometrical dimensions of martensite variants. The phenomenon is owed to the appearance of induced martensite under load, together with martensite thermal formed. The cast structure has a high granulation, with defects like goals, pores and chemical segregations.
- After hot plastic deformation through forging, the grains dimension are not modify, unless their orientation on deformation direction.

Although the SMAs have a large application domain, the obtaining of parts made from SMAs at industrial level is limited due to processing difficulties. The good shape memory properties can guarantee the functioning time for various parts, used in industrial applications.

## Author details

Petrică Vizureanu\*, Dragoș-Cristian Achiței, Mirabela-Georgiana Minciună and Manuela-Cristina Perju

\*Address all correspondence to: peviz2002@yahoo.com

“Gheorghe Asachi” Technical University of Iași, Romania

## References

- [1] Achiței DC, Abdullah MMA, Sandu AV, Vizureanu P, Abdullah A. On the fatigue of shape memory alloys. *Advanced Materials Engineering and Technology II*. 2014;**594-595**:133. DOI: 10.4028/www.scientific.net/KEM.594-595.133
- [2] Samoilă C, Cofas P, Cofas D, Ursuțiu D, Vizureanu P, Aliaje cu memoria formei; 2011; Brasov, Editura Universității Transilvania. ISBN 978-973-598-934-7
- [3] Available from: <https://www.linseis.com/>
- [4] Available from: <http://standardservice.ro/spectrometre/>
- [5] Available from: <http://www.panalytical.com/Xray-diffractometers.htm>
- [6] Available from: [http://ctherm.com/products/tci\\_thermal\\_conductivity/](http://ctherm.com/products/tci_thermal_conductivity/)
- [7] Available from: <https://www.zeiss.com/microscopy/us/products/light-microscopes/axio-observer-for-materials.html>
- [8] Available from: <https://www.tescan.com/en-us/technology/sem/vega3>

---

# Modeling of the Two-Way Shape Memory Effect

---

Meddour Belkacem and Brek Samir

Additional information is available at the end of the chapter

<http://dx.doi.org/10.5772/intechopen.75657>

---

## Abstract

The shape memory alloys (SMA) are distinguished from other conventional materials by a singular behavior which takes many forms depending on the thermomechanical load. The two-way shape memory effect is one of these forms. The interest that exhibits this behavior is that the material can remember two states, so this leads to many industrial applications. This thermoelastic property is driven by the temperature under residual stress of education. To model this effect in 3D, we considered stress and temperature as control variables and the fraction of martensite as internal variable; choosing Gibbs free energy expression and applying thermodynamic principles with transformation criteria have permitted to write the constitutive equations that control this behavior. The constructed model is then numerically simulated, and finally, the proposed model appears applicable in engineering.

**Keywords:** two-way, simulation, hysteresis, transformation

---

## 1. Introduction

Shape memory alloys (SMA) as they are called are a kind of particular materials which have a singular behavior, they can be largely deformed (about 10%) under an applied mechanical, a simple heating is sufficient to recover the previous form, that is why they are called that way.

By varying controlled parameters (stress and temperature), these alloys can exhibit other properties like pseudoelasticity, two-way shape memory effect, one-way shape memory effect [1, 2], and reorientation effect [3].

These properties derive from phase transformations, i.e., higher temperature phase (austenite) to lower temperature phase (martensite).

---

It is observed that these phase transformations do not occur with diffusion but rather with displacement, i.e., displacement at a distance less than interatomic [4, 5].

These important properties made them requested materials in various fields such as biomedical automotive industry, fire watch devices, aeronautics, and medical devices [6].

Two-way shape memory effect is obtained after the alloy is subjected to an education [7], i.e., to a cyclic thermal load under a constant mechanical load (**Figure 1**).

It should be noted that the previous education is performed to create a field of internal stresses, which will substitute the macroscopic ones; under a cyclic thermal load, the alloy will remember two states: one is at lower temperature (martensite) and the other at higher temperature (austenite) (**Figure 2**).

The next steps in this paper are to build the constitutive model and simulate it using an algorithm; regarding model parameters, we will use the work of [8].

## 2. Methods and materials

### 2.1. Constitutive equations

Let us choose the following free energy expression:

$$G(\sigma = \sigma_{00}, T, f) = -\sigma_{00} : S_A : \sigma_{00} - f \cdot \epsilon_0 \cdot \sigma_{00} : R + f \cdot B \cdot (T - M_s^0) + C \cdot f \cdot (1 - f) \quad (1)$$

$S_A$ : Fourth order tensor of complaisance; B, C: Constants to be determined, respectively, related to change of phase and interaction between austenite and martensite; f: Fraction of martensite;  $\sigma_{00}$ : Tensor of stress created after education.

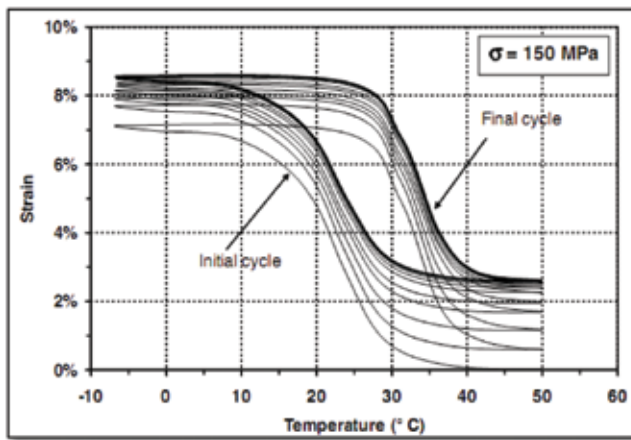


**Figure 1.** Education (50 cycles) performed on a NiTi wire under constant stress of 150 MPa [7].

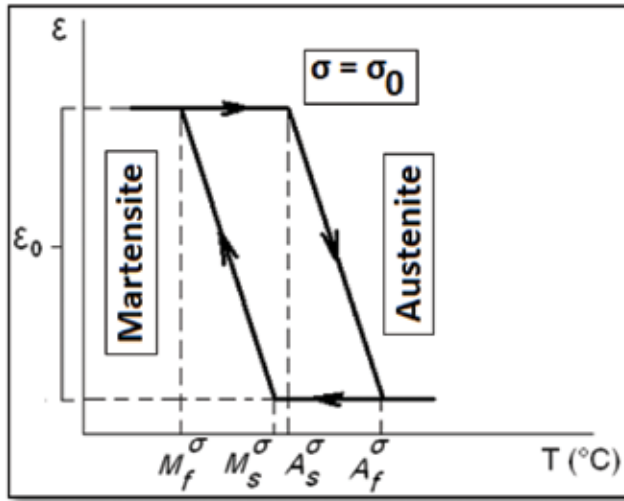


**Figure 2.** One-dimensional two-way effect.  $M_s^\sigma$  : Temperature of transformation start A- > M under stress  $\sigma$ .  $M_f^\sigma$  : Temperature of transformation finish A- > M under stress  $\sigma$ .  $A_s^\sigma$  : Temperature of transformation start M- > A under stress  $\sigma$ .  $A_f^\sigma$  : Temperature of transformation finish M- > A under stress  $\sigma$ .  $\epsilon_0$ : Uniaxial maximum deformation.

Assuming that dissipation is associated only with transformation (fraction of martensite) [9, 10], the second principle of thermodynamics can be written as

$$-\frac{\partial G}{\partial f} \cdot \frac{df}{dt} \geq 0 \quad (2)$$

Let us write the driving force  $F^{th}$ :

$$F^{th} = -\frac{\partial G}{\partial f} \quad (3)$$

Then,

$$F^{th} = \epsilon_0 \cdot \sigma_0 : R - B \cdot (T - M_s^0) + C(2f - 1) \quad (4)$$

Because of hysteresis, there is a dissipative force  $F^{di}$ , which will oppose  $F^{th}$ .

We choose expression of  $F^{di}$ :

$$F^{di} = Kf + H \quad (5)$$

Transformation occurs when

$$F^{th} = F^{di} \quad (6)$$

We introduce the criteria functions:

$$\varphi^{\text{di}} = F^{\text{th}} - F^{\text{di}}; \dot{f} > 0; f \geq 0; f \leq 1 \quad (7)$$

$$\varphi^{\text{di}}(\sigma = \sigma_{00}, T, f) = \varepsilon_0 \cdot \sigma_{00} : R - B \cdot (T - M_s^0) + C(2f - 1) - Kf - H \quad (8)$$

Condition of consistence gives

$$d\varphi^{\text{di}}(\sigma = \sigma_{00}, T, f) = 0; \dot{f} > 0; f \geq 0; f \leq 1 \quad (9)$$

$$\frac{\partial \varphi^{\text{di}}}{\partial \sigma} d\sigma + \frac{\partial \varphi^{\text{di}}}{\partial T} dT + \frac{\partial \varphi^{\text{di}}}{\partial f} df = 0 \quad (d\sigma = 0) \quad (10)$$

$$df = \frac{B \cdot dT}{(2C - K)}; \dot{f} > 0 \quad (11)$$

Doing the same with the reverse transformation

$$\varphi^{\text{in}}(\sigma = \sigma_{00}, T, f) = \varepsilon_0 \cdot \sigma_{00} : R - B \cdot (T - M_s^0) + C(2f - 1) + Gf + H \quad (12)$$

$$df = \frac{B \cdot dT}{(2C + K)}; \dot{f} < 0; f \geq 0; f \leq 1 \quad (13)$$

Eqs. (11) and (13) give the evolution of fraction of martensite.

The deformation resulting from transformation of austenite to martensite is denoted  $\varepsilon^T$ ; this deformation is associated with fraction of martensite:

$$d\varepsilon^T = df \cdot \varepsilon_0 \cdot R; \dot{f} > 0; f \geq 0; f \leq 1 \quad (14)$$

$R$  is a tensor of transformation, and it can be written as the following:

$$R = \frac{\sigma}{\sqrt{\sigma : \sigma}} \quad (15)$$

$$d\varepsilon^T = \frac{B \cdot dT}{(2C - K)} \varepsilon_0 \cdot R; \dot{f} > 0; f \geq 0; f \leq 1 \quad (16)$$

$$d\varepsilon^T = \frac{B \cdot dT}{(2C + K)} \varepsilon_0 \cdot R; \dot{f} < 0; f \geq 0; f \leq 1 \quad (17)$$

## 2.2. Determination of constants $B$ , $C$ , $K$ , and $H$

At the beginning of direct transformation

$$\sigma_{00} = \begin{pmatrix} \sigma_0 & 0 & 0 \\ 0 & 0 & 0 \\ 0 & 0 & 0 \end{pmatrix}, T = M_s^\sigma, f = 0 \quad (18)$$

$$\varphi^{\text{di}}(\sigma = \sigma_{00}, T = M_s^\sigma, f = 0) = \varepsilon_0 \cdot \sigma_{00} : R - B \cdot (M_s^\sigma - M_s^0) + C - H = 0 \quad (19)$$

At the end of the direct transformation

$$\sigma_{00} = \begin{pmatrix} \sigma_0 & 0 & 0 \\ 0 & 0 & 0 \\ 0 & 0 & 0 \end{pmatrix}, T = M_f^\sigma, f = 1 \quad (20)$$

$$\varphi^{di}(\sigma = \sigma_0, T = M_f^\sigma, f = 1) = \varepsilon_0 \cdot \sigma_0 : R - B \cdot (M_f^\sigma - M_s^0) - C - K - H = 0 \quad (21)$$

At the beginning of the reverse transformation

$$\sigma_{00} = \begin{pmatrix} \sigma_0 & 0 & 0 \\ 0 & 0 & 0 \\ 0 & 0 & 0 \end{pmatrix}, T = A_s^\sigma, f = 1 \quad (22)$$

$$\varphi^{in}(\sigma = \sigma_0, T = A_s^\sigma, f = 1) = \varepsilon_0 \cdot \sigma_0 : R - B \cdot (A_s^\sigma - M_s^0) - C + K + H = 0 \quad (23)$$

At the end of the reverse transformation

$$\sigma_{00} = \begin{pmatrix} \sigma_0 & 0 & 0 \\ 0 & 0 & 0 \\ 0 & 0 & 0 \end{pmatrix}, T = A_f^\sigma, f = 0 \quad (24)$$

$$\varphi^{in}(\sigma = \sigma_0, T = A_f^\sigma, f = 0) = \varepsilon_0 \cdot \sigma_0 : R - B \cdot (A_f^\sigma - M_s^0) + C + H = 0 \quad (25)$$

### 2.3. Experimental data

**Table 1** illustrates experimental data and material constants  $B$ ,  $C$ ,  $K$ , and  $H$ . The used material is CuZnAl. The test was performed under constant stress ( $\sigma = 65$  MPa).

### 2.4. Numerical simulation

#### 2.4.1. One-dimensional case

We considered a segment of CuZnAl submitted to a constant stress ( $\sigma = 65$  MPa) and a thermal load ( $300 \leq T \leq 400$  K) (**Figure 3**).

$M_s^0(K)$	313	$M_s^\sigma(K)$	324	$E_A(MPa)$	72,000
$M_f^0(K)$	303	$M_f^\sigma(K)$	311	$E_M(MPa)$	70,000
$A_s^0(K)$	315	$A_s^\sigma(K)$	330	$\varepsilon_0$	0.023937
$A_f^0(K)$	325	$A_f^\sigma(K)$	340	$H(MPa)$	0.2606751918
$B(MPa \cdot K^1)$	3.258439E-2	$C(MPa)$	0.18736036121	$K(MPa)$	4.8876464E-2
$\nu$	0.3				

**Table 1.** Experimental data [8, 11].

2.4.2. Three-dimensional case

The considered specimen is a cubic element subjected to a constant mechanical load which is a triaxial traction and thermal loads ( $\sigma_{11} = \sigma_{22} = \sigma_{33} = 50 \text{ MPa}$ ) and ( $300 \leq T \leq 400 \text{ K}$ ) (Figures 4–6).

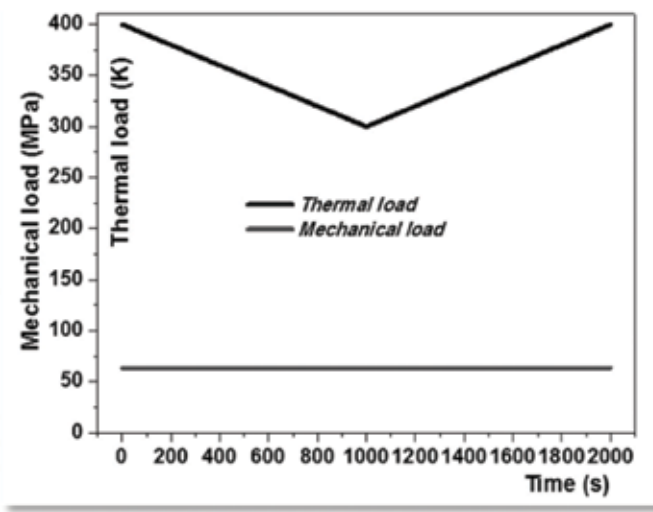


Figure 3. History of coupled loading.

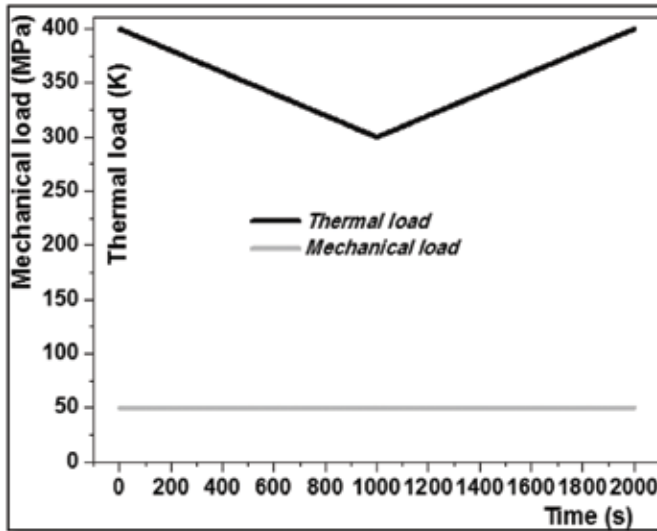


Figure 4. Loading in the direction of  $\sigma_{11}$ .

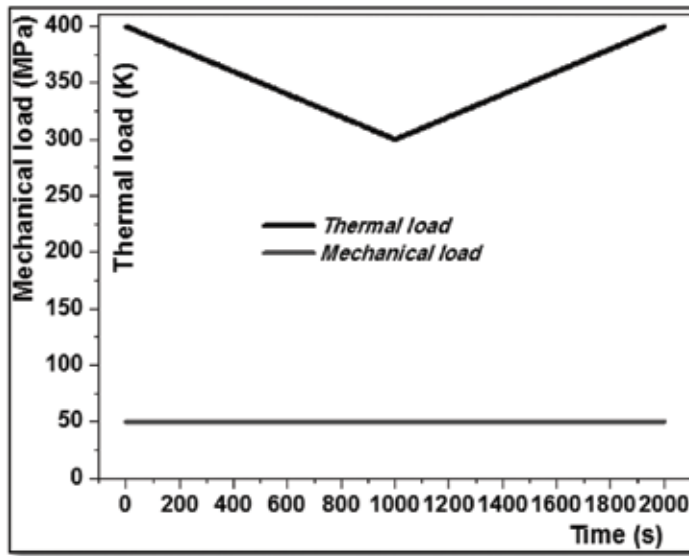


Figure 5. Loading in the direction of  $\sigma_{22}$ .

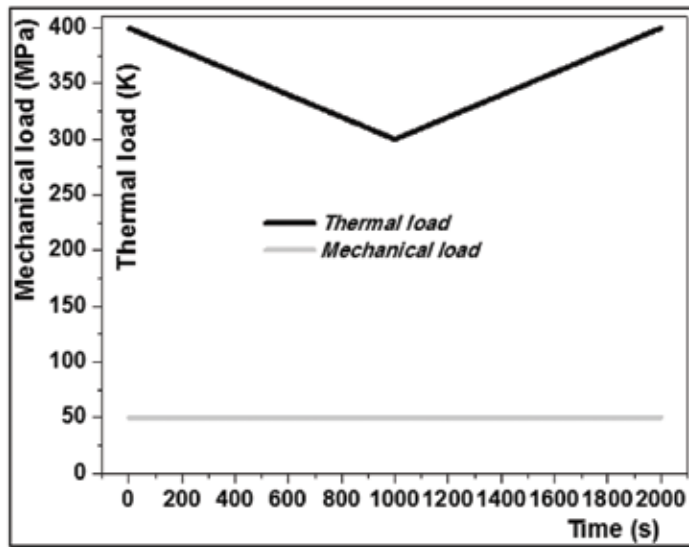


Figure 6. Loading in the direction of  $\sigma_{33}$ .

### 3. Results

#### 3.1. One-dimensional case

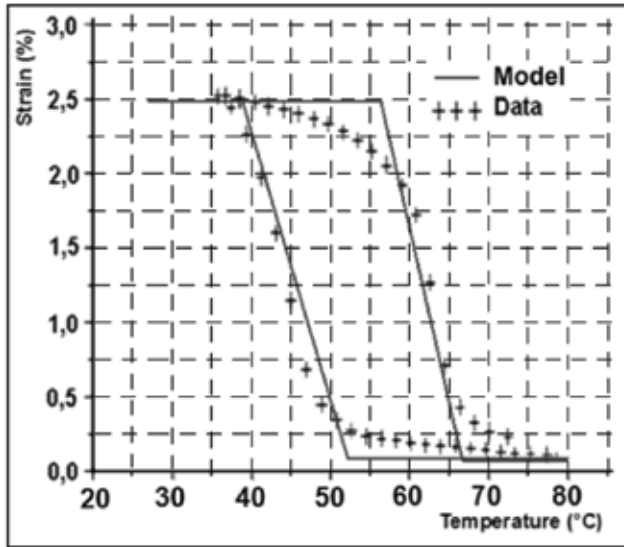


Figure 7. Response at ( $\sigma = 65$  MPa).

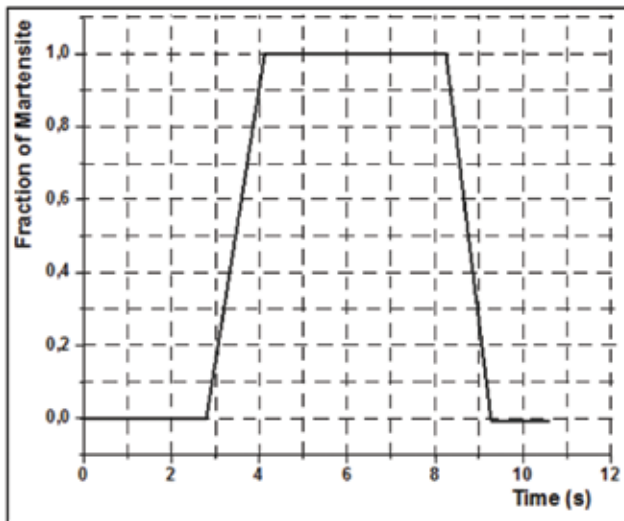


Figure 8. Evolution of the fraction of martensite.

### 3.2. Three-dimensional case

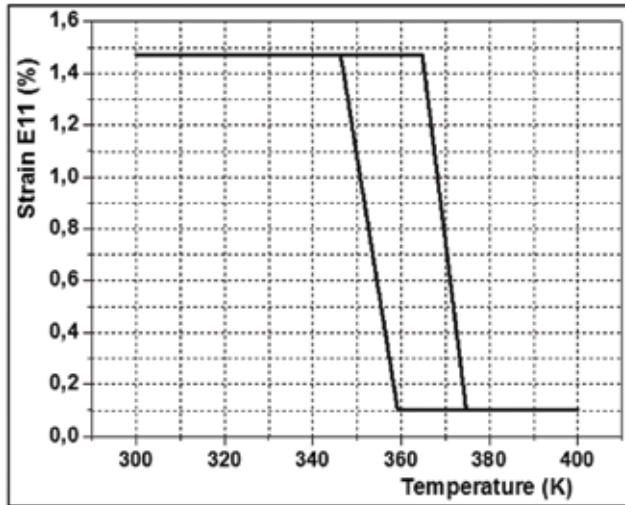


Figure 9. Plot  $T - \epsilon_{11}$ .

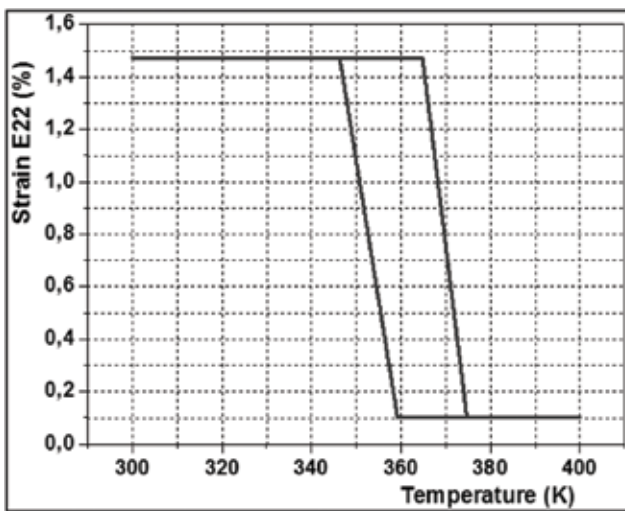


Figure 10. Plot  $T - \epsilon_{22}$ .

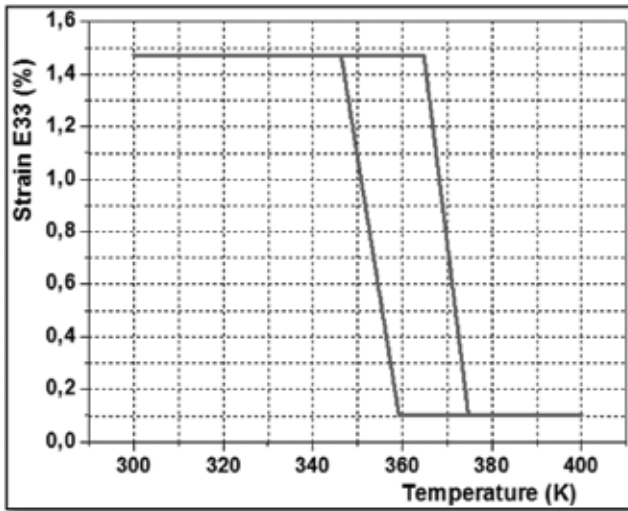


Figure 11. Plot  $T-\epsilon_{22}$ .

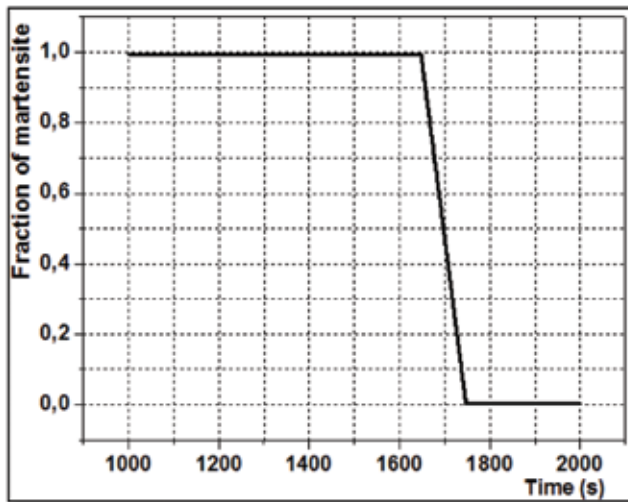


Figure 12. Evolution of fraction of martensite in direct transformation.

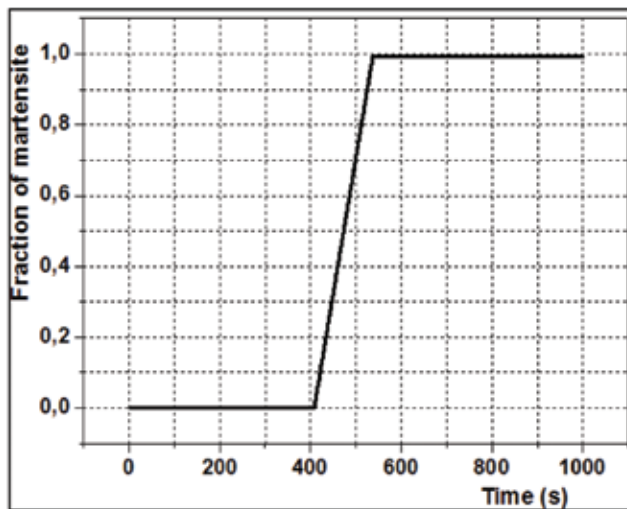


Figure 13. Evolution of fraction of martensite in reverse transformation.

#### 4. Discussion

After having written constitutive equations and criteria functions, the numerical simulation has permitted to obtain previous results.

First, we used the extracted values from the curve of the test in order to compare this curve with the response of the model in one-dimensional case, and we obtained **Figure 7**. This figure presents a good agreement between experimental data and the model response.

On the other hand, **Figure 8**, which is representing the evolution of the martensite fraction, is also in agreement with the curve in **Figure 7**, i.e., the direct transformation and the reverse transformation are functions of martensite fraction. We can say that the constitutive model behaves well in one-dimensional case.

For the three-dimensional case, **Figures 9–11** show the response under the triaxial traction and thermal load; for each plot, there is a hysteresis.

The shrinking of the hysteresis in each case of the figures should be noted (**Figures 9–11**); this is due to the triaxial loading.

Despite the applied triaxial load, **Figures 9–11** exhibit the thermomechanical cycle as it is in case of one-dimensional two-way effect (**Figure 7**).

**Figures 12 and 13** show the evolution of fraction of martensite for each case of direct and reverse transformations, and the shapes of the plots are compatible with **Figures 9–11** as the

one-dimensional case because it was noticed previously that the deformation is proportional to the amount of martensite.

## 5. Conclusion

In this work, we have developed a 3D constitutive model using the principles of thermodynamics and a simple formalism, and these principles have permitted to write criteria of transformation. This macroscopic model is developed by simple formalism and assumptions.

By using an algorithm, we have implemented the model, and the response seems to be compatible with the nature of the two-way shape memory effect. In the one-dimensional case, we have observed a good agreement between the numerical and experimental plots.

It should be noted that the parameters of the model were determined by the one-dimensional test and further used in the biaxial and triaxial cases to ensure consistency of the model in different cases of loading. The implementation of the model in the algorithm is simple and practical. The obtained results testify the usability of the developed model.

At the end, we can say that this macroscopic constitutive model can be used in applications to engineering problems, in order to particularly simulate the pseudoelastic effect of shape memory alloys.

## Author details

Meddour Belkacem\* and Brek Samir

\*Address all correspondence to: [samsum66@gmail.com](mailto:samsum66@gmail.com).in

Department of Mechanical Engineering, University of Khenchela, Algeria

## References

- [1] Arghavani J, Auricchio F, Naghdabadi R, Reali A, Sohrabpour S. A 3D phenomenological constitutive model for shape memory alloys under multiaxial loadings. *International Journal of Plasticity*. 2010;**26**:976-991
- [2] Yutaka T, Jong-Bin L, Minoru T. Finite element analysis of superelastic, large deformation behaviour of shape memory alloy helical springs. *Computers and Structures*. 2004;**82**: 1685-1693
- [3] Pan H, Thamburaja P, Chau FS. Multi-axial behaviour of shape memory alloys undergoing martensitic reorientation and detwinning. *International Journal of Plasticity*. 2007;**23**: 711-732

- [4] Otsuka K. Perspective of research on martensitic transformations present and future. *Journal de Physique IV*. 2001;**11**:3-9
- [5] J. Van Humbeeck. La transformation martensitique, dans *Technologie des*. Chapter 3. In: *Alliages 'a M'emoire de Forme*. Paris, France: Hermes; 1993. pp. 63-88
- [6] Duerig T, Pelton A, Stockel D. An overview of nitinol medical applications. *Materials Science and Engineering*. 1999;**A273-275**:149-160
- [7] Miller DA, Lagoudas DC. Thermo-mechanical characterization of NiTiCu and NiTi SMA actuators: Influence of plastic strains. *Smart Materials and Structures*. 2000;**9**(5):640-652
- [8] Bourbon G, Lexcelent C, Leclercq S. Modelling of the non-isothermal cyclic behaviour of a polycrystalline Cu-Zn-Al shape memory alloy. *Journal de Physique IV*. 1995;**5**(C8):221-226
- [9] Patoor E, Eberhardt A, Berveiller M. On Micromechanics of Thermoelastic Phase Transition. The proceedings of *Plasticity 93: The Fourth International Symposium on Plasticity and Its Applications*, Baltimore, Maryland. 1993, July. 19-23
- [10] Lagoudas DC, Entchev PB. Modeling of transformation-induced plasticity and its effect on the behavior of porous shape memory alloys. Part I: Constitutive model for fully dense SMAs. *Mechanics of Materials*. 2004;**36**(9):865-892
- [11] Shape Memory Applications Inc. Available from: <http://heim.ifi.uio.no/~mes/inf1400/COOL/Robot%20Projekt/Flexinol/Shape%20Memory%20Alloys.htm>



---

# Linear Shape Memory Alloy Thermomechanical Actuators

---

Velaphi Msomi and Graeme Oliver

Additional information is available at the end of the chapter

<http://dx.doi.org/10.5772/intechopen.76292>

---

## Abstract

The thermally activated changes in crystal structure in nickel-titanium shape memory alloy (SMA) material, which produces transformation strains of an order of magnitude higher than and opposite to the thermal strains, have been described using different models. Some of these models are defined by cyclic functions (trigonometric functions) which they become complex to control when they are subjected to a wide range of transformation temperatures. This chapter presents an alternative model to better describe the behavior of SMA for a more general temperature range, which an SMA-powered actuator might be subjected to. The proposed model is then implemented to the analysis of one-dimensional (1D) problem oriented to the two-dimensional (2D) space. The simulation results were then graphically compared to the experiment.

**Keywords:** shape memory alloy, finite element analysis, shape memory effect, phase transformation

---

## 1. Introduction

Shape memory alloys (SMAs) are being described as smart materials due to their ability of memorizing shape. Their ability in memorizing shapes requires some training suitable for user's application. The trained SMA exhibits two behaviors, that is, superelasticity and shape memory effect depending on the temperature. Those behaviors are triggered by the phenomenon occurring at the microstructural level called phase transformation. Phase transformation can be induced by stress or temperature. When SMA is mechanically loaded at room temperature (or at a temperature below thermal transition), the twinned martensite transforms to detwinned martensite [1]. When the detwinned martensite is subjected to heat, the detwinned martensite transforms to austenite phase. When the fully austenite SMA is cooled down, there

---

will be a temperature range where austenite will transform back to twinned martensite. This whole process is called shape memory effect. When a mechanical load is applied on SMA which is subjected to temperature above austenitic finish temperature, the deformation will take place. The deformation will be reversed completely upon the removal of mechanical load. This phenomenon is called superelasticity. These two physical behaviors are the ones that make SMA a good candidate for actuation applications. There are a number of models reported in the study which are meant to describe the phase transformation kinetics [1]. The first model was developed by Tanaka and Nagaki [2, 3] which was later improved by Boyd and Lagoudas [4]. The firstly developed model was based on exponential functions. Boyd and Lagoudas redefined the material constants so as to suit their application. Later, a model based on cosine functions was developed by Liang and Rogers [5]. Liang and Rogers developed their model with the purpose of applying it to the analysis of acoustic vibrations control [5–7]. The common factor in these models is the calculation material constants which are calculated based on transformation temperatures. Brinson [8] developed another alternative phase transformation model, where the internal variable measuring the evolution of martensite phase was split into two.

The first internal variable is induced by temperature and the second one is induced by stress. This work proposed that the elastic modulus should be split into austenitic and martensitic modulus. It should be noted that these models developed by the previously listed authors are functions of transformation temperature (martensite start temperature, martensite finish temperature, austenite start temperature and austenite finish temperature). These temperatures are crucial since they are used to calculate certain material constants. More work has been done in improving the already existing models [9, 12–15]. This chapter proposes a one-dimensional (1D) new model to describe the physical behavior of SMA for all transformation ranges. The proposed model is then used to simulate 1D structural deflection which is orientated in two-dimensional (2D) space. The simulated results are compared to the experimental results.

## 2. Phase transformation models

This section shows the already available phase transformation models. It should be noted that the law adopted for the proposed model is based on the one adopted by Liang and Rogers [5] with the difference on the phase transformation estimation. The first phase transformation model based on exponential functions was developed by Tanaka et al. [2, 3]. The transformation from martensite to austenite is given by

$$\xi = \xi_0 \exp[a_A(T - A_s) - b_A\sigma] \quad (1)$$

And the transformation from austenite to martensite is given by

$$\xi = 1 - \exp[a_M(T - M_s) - b_M\sigma] + \xi_0 \quad (2)$$

where  $\xi_0$ ,  $a_M$  and  $b_M$ ,  $M_s$ ,  $\sigma$ ,  $a_A$ ,  $b_A$  and  $A_s$  are internal variables measuring martensite volume fraction evolution, martensitic material constants, martensite start temperature, austenitic

material constants and austenite start temperature, respectively. Boyd and Lagoudas [11] developed the calculation of material constants ( $a_M$ ,  $b_M$ ,  $a_A$  and  $b_A$ ) as follows:

$$a_M = \frac{2\ln 10}{M_s - M_f}, b_M = \frac{a_M}{C_M}, a_A = \frac{2\ln 10}{A_f - A_s}, b_A = \frac{a_A}{C_A} \quad (3)$$

Later, Liang and Rogers [5] presented another alternative model for martensite volume fraction calculation. Their model was based on trigonometric functions (cyclic functions), that is, cosine functions. The following equation describes the phase transformation during heating (martensite transforms to austenite):

$$\xi = \frac{\xi_0}{2} \left\{ 1 + \cos \left[ A_A \left( T - A_s - \frac{\sigma}{C_A} \right) \right] \right\} \quad (4)$$

This transformation occurs between the stress ranges described as follows:

$$C_A(T - A_f) < \sigma < C_A(T - A_s) \quad (5)$$

The transformation occurs during cooling (austenite transforms to martensite) and is given by

$$\xi = \frac{1 - \xi_0}{2} \cos \left[ A_M \left( T - M_f - \frac{\sigma}{C_M} \right) \right] + \frac{1 + \xi_0}{2} \quad (6)$$

The stress restriction is described as follows:

$$C_M(T - M_s) < \sigma < C_M(T - M_f) \quad (7)$$

The material constants involved in Liang and Rogers [5] are the same as those used in Tanaka's model [2]. The difference comes with the calculation of the two constants which are given as follows:

$$A_M = \frac{\pi}{M_s - M_f}; A_A = \frac{\pi}{A_f - A_s} \quad (8)$$

It should be noted that the calculation of the two material constants,  $A_A$  and  $A_M$ , involves the difference in transformation temperatures. It was noticed that the previously mentioned models were not compatible with our application due to the size of our temperature range. The new non-cyclic model had to be developed. The proposed phase transformation model is based on the hyperbolic functions. The phase transformation during heating (martensite transforms to austenite) is given by the following equation:

$$\xi = \xi_0 \{ 1 - \tanh[A_A(T - A_s) + \vartheta_A] \} \quad (9)$$

The phase transformation during cooling (austenite transforms to martensite) is described by the following equation:

$$\xi = \xi_0 \{ 1 - \tanh[A_M(T - M_f) + \vartheta_M] \} \quad (10)$$

The calculation of material constants  $A_A$  and  $A_M$  is similar to that of Eq. (8). The phase transformation constants ( $A_s$  and  $M_s$ ) are those described previously. The constants  $\vartheta_A$  and  $\vartheta_M$  are given by

$$\vartheta_A = -\frac{A_A}{C_A}\sigma; \vartheta_M = -\frac{A_M}{C_M}\sigma \quad (11)$$

The constants  $C_A$  and  $C_M$  are the same as those used by Liang and Rogers. The developed phase transformation model was then used in performing the 2D analysis on a steel beam deflection explained in the next section. Prior to the performance of simulation analysis, an experiment was performed with the purpose of obtaining simulation parameters and verification of numerical results.

### 3. Beam deflection test experiment

The experiment was performed using the following equipment:

1. Explorer GLX Data logger
2. Nickel titanium shape memory alloy wire of 0.5-mm diameter
3. ISO-TECH IPS 2303 Laboratory DC Power Supply
4. Linear variable differential transformer (LVDT)
5. Fluke 190C Scope meter
6. Rectangular steel beam
7. Rectangular steel frame

The steel beam used in the performance of this experiment was 300-mm long with a 25-mm breadth and 1.2-mm thickness. Both ends of the steel beam were fixed on top of the vertical rectangular steel frame. The effective length for the steel beam after installation to the vertical rectangular steel frame was 243 mm. **Figure 1** shows the complete experimental setup.

A 184-mm long NiTi SMA wire with a 0.5-mm diameter was attached with one end at the center of the steel beam and the other end at the center foot of the steel frame. The attachment of the NiTi SMA wire to the frame and to the beam was isolated using high-melting temperature plastic tubes. The isolation was required since the NiTi SMA wire was heated through the joules heating method. The NiTi SMA wire was attached at the center of the beam so as to get the maximum deflection. During the performance of the experiment, two types of data were being logged, that is, beam deflection and the NiTi SMA wire temperature. The beam deflection was recorded through the LVDT which was powered by the DC power supply (shown in **Figure 1**). The LVDT data were logged in the form of output voltage and it was translated into millimeters using the method described subsequently. The temperature was recorded using a GLX explorer data logger. A 1.54 A was supplied to the NiTi SMA wire, and the temperature

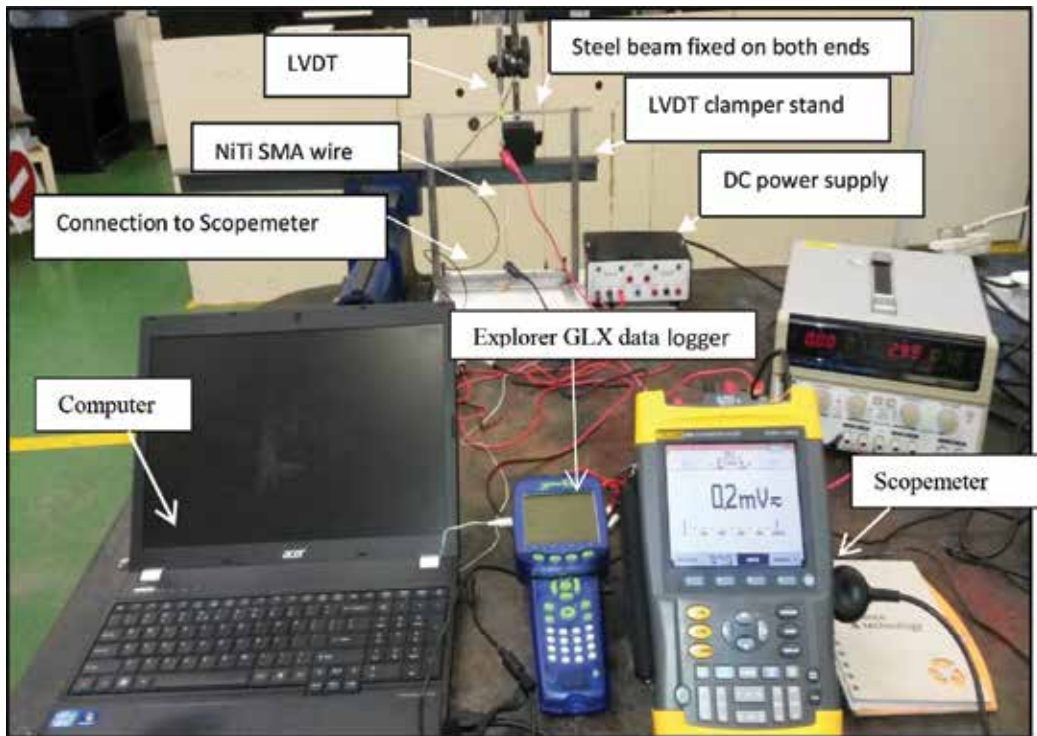


Figure 1. Beam test experiment setup.

of the wire increased from the room temperature to a maximum temperature. The wire was allowed to cool down after reaching the maximum deflection of the beam, and then the beam could go back to its rest position. This process was repeated several times so as to get stable results.

#### 4. Deflection test results

The following figures show the experimental results for the beam deflection test and these results are used to validate FEA results. Although there were several tests conducted, only one graph is presented to avoid repetition. It should be noted that the results presented are already translated into millimeters using the method explained in the study [10]. **Figure 2** shows the time it takes for a beam to finish the full deflection cycle, that is, the deflection from the rest position to the final position or the maximum deflection and from the final position back to the rest position.

During heating, the beam deflects from the rest position to the maximum deflection and the reverse during cooling. It is clearly seen from the figure that the beam's maximum deflection is reached in less than 10 s which is very quick. This quickness is suggested to be related to the wire diameter. The smaller the diameter, the faster the response of the wire. It is noted in

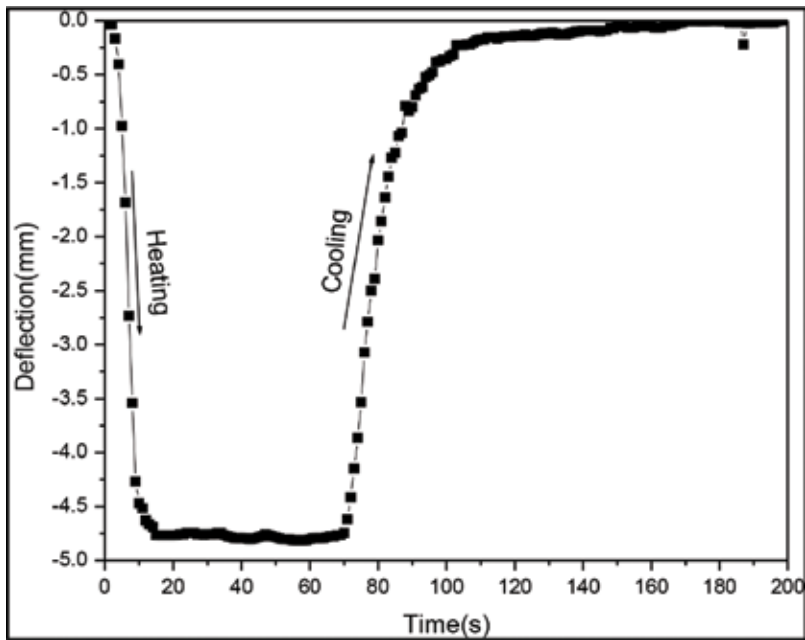


Figure 2. Time-deflection curve.

the figure that there is a flatness of the graph between 10 and 70 s. This flatness shows the beginning of the cooling cycle. It should be remembered that the driving force behind this graph is the NiTi SMA wire phase transition as discussed in Section 1. The martensite phase transforms to austenite phase between 0 and 10 s upon heating. The austenite phase is the dominant phase between 10 and 70 s, and then the nucleation of martensite starts to occur after 70 s. Martensite start occurs after 70 s and finishes after 140 s. The flatness behavior is seen after 140 s which depicts the domination of martensite phase. The number of data points between 0 and 10 s are few compared to the rest of the graph, and this is caused by the fact that the sampling rate was not easy to control.

The SMA wire force, which produced the maximum deflection of the steel beam, is shown in **Figure 3**. The maximum force produced by the current SMA wire (184-mm long) was found to be approximately 35.87517 N (~3.5 kg).

**Figure 3** shows the deflection of the beam to the negative vertical ( $y$ ) direction as the temperature increases and the reverse during cooling. It is noted that all the values on the  $y$ -axis of each figure are negative. This indicates that the direction of steel beam is to the negative  $y$ -direction. It is noted also that the curves (from **Figures 2–4**) are not smooth, and this is caused by the uncontrolled environmental conditions. The maximum deflection is taken with consideration of the sign of the value since it symbolizes the axis direction.

The deflection test results seem to be in agreement with the general behavior of shape memory alloy material. Therefore, these results will be used as the benchmark for simulation results and will be compared with FEA results in the following section.

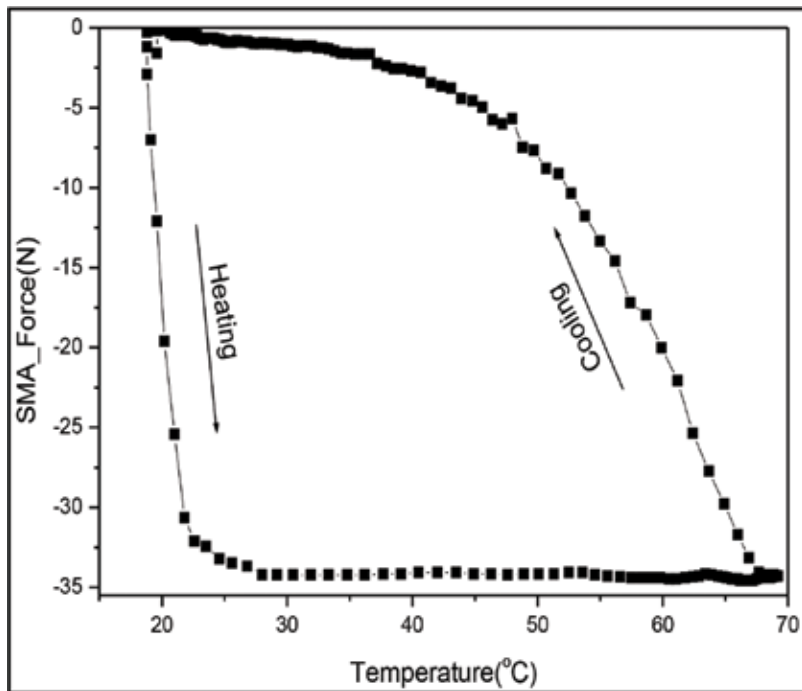


Figure 3. SMA wire force-temperature graph.

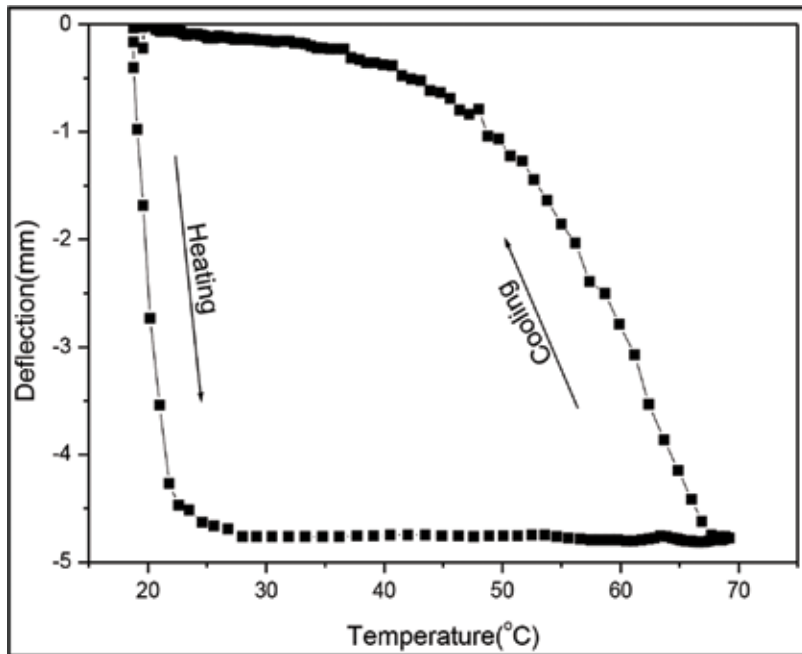
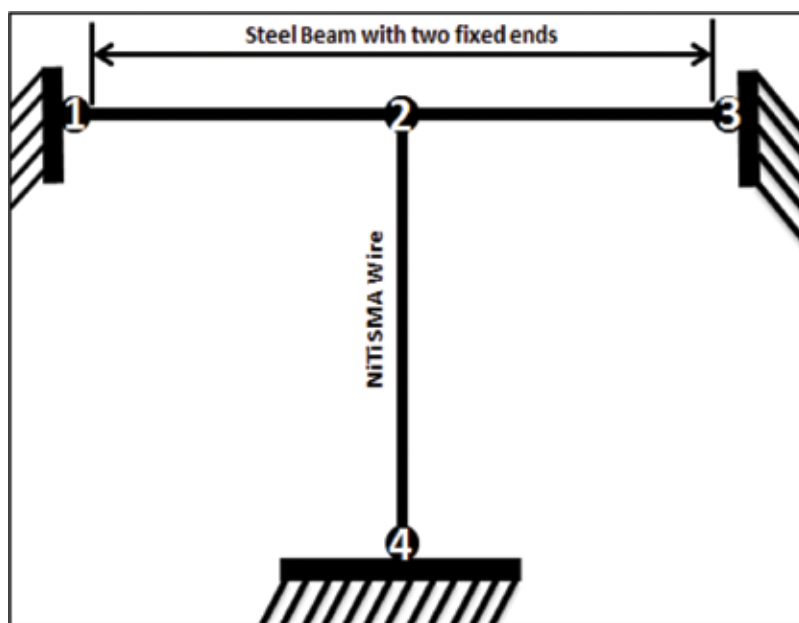


Figure 4. Steel beam deflection-temperature graph.

## 5. Finite element analysis on a 2D beam setup

This section reflects the application of the proposed NiTi SMA model in predicting the response of the steel beam subjected to mechanical loading from NiTi SMA wire. Prior to the performance of the finite element analysis, an experiment was performed so as to find the simulation parameters like transformation temperature, the beam effective length and breadth, SMA wire effective length, and so on. To perform finite element analysis, a four-noded beam bar structure was constructed as shown in **Figure 5**. Two elements were steel beam elements and one bar element was NiTi SMA wire.



**Figure 5.** Steel beam bar-SMA setup.

## 6. SMA model implementation

This section deals with the computer implementation of the finite element analysis. The local and the global plane beam bar element systems are being demonstrated schematically and are shown in **Figure 6**. The system has got three elements where each element has six degrees of freedom (three degrees of freedom per node). The axial degrees of freedom are ignored due to the nature of loading, hence the degrees of freedom per node are reduced from three to two, and therefore each element remains with four degrees of freedom (i.e. vertical displacement and rotation). The element node displacements and forces are given by Eqs. (12)–(14) as follows:

Element 1:

$$\underline{f}^{(1)} = \begin{bmatrix} f_{y1} \\ m_{\theta R1} \\ f_{y2} \\ m_{\theta R2} \end{bmatrix} \quad (12)$$

$$\underline{u}^{(1)} = \begin{bmatrix} u_{y1} \\ \theta_{R1} \\ u_{y2} \\ \theta_{R2} \end{bmatrix}$$

Element 2:

$$\underline{f}^{(2)} = \begin{bmatrix} f_{y2} \\ m_{\theta R2} \\ f_{y3} \\ m_{\theta R3} \end{bmatrix} \quad (13)$$

$$\underline{u}^{(2)} = \begin{bmatrix} u_{y2} \\ \theta_{R2} \\ u_{y3} \\ \theta_{R3} \end{bmatrix}$$

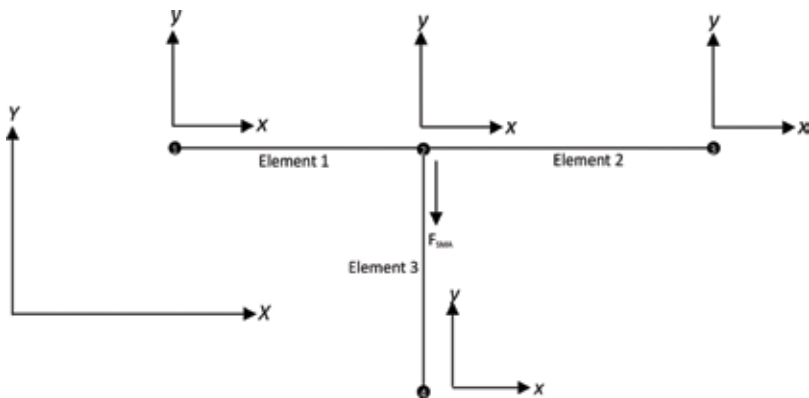


Figure 6. Plane bar elements in its local and global system.

Element 3:

$$\begin{aligned} \underline{f}^{(3)} &= \begin{bmatrix} f_{x2} \\ f_{y2} \\ f_{4x} \\ f_{4y} \end{bmatrix} \\ \underline{u}^{(3)} &= \begin{bmatrix} u_{x2} \\ u_{y2} \\ u_{4x} \\ u_{4y} \end{bmatrix} \end{aligned} \quad (14)$$

For beam stiffness calculations, the only material properties required are the modulus of elasticity  $E$ , the second moment of area  $I$  and the length  $L$  of the beam. For the bar stiffness calculation, the only properties required are the cross-sectional area  $A$ , the modulus of elasticity  $E$  and the length  $L$  of the bar. These properties are taken to be constant throughout the bar and the beam. The solution procedure for our present problem is shown in Appendix A.

The schematic diagram for solution flow is shown in **Figure 7**. The solution diagram is a general solution flow to be used to solve one-sided temperature and phase coupling of any given 2-D geometry. In our case, we assume that phases are only affected by temperature and not by stress or pressure. The temperature affects the calculation of volume fraction through Eqs. (9) and (10). The linear averaged property (Young's modulus,  $E$ ) is then calculated together with other parameters mentioned under phase transformation section.

The stiffness matrix of beam is formed using material properties of the beam and then that affects the formation of forces due to shape memory effect which is triggered by temperature variation. In our case, there are no external loads. This brings us to the calculation of the linear solution of Eq. (A8) from Appendix A. The process gets repeated until the maximum allowed temperature is reached.

**Figure 7** summarizes the solution flow process of the developed simulation tool.

## 7. Simulation and experimental results

This section reflects the numerical results obtained from 1D finite element analysis. The material parameters used during FEA simulation are tabulated in **Table 1**. These parameters were derived from experiment using the procedure available in the study [11].

**Figure 8** shows the deflection-time graph where we wanted to see if the numerical results would match the experimental results. Therefore, based on the results, it can be seen that the simulation curve resembles the experimental curve. Both curves show the maximum deflection of about 4.9 mm in less than 10 s. The two curves follow the same trend and they both do not exceed the maximum deflection of 5 mm.

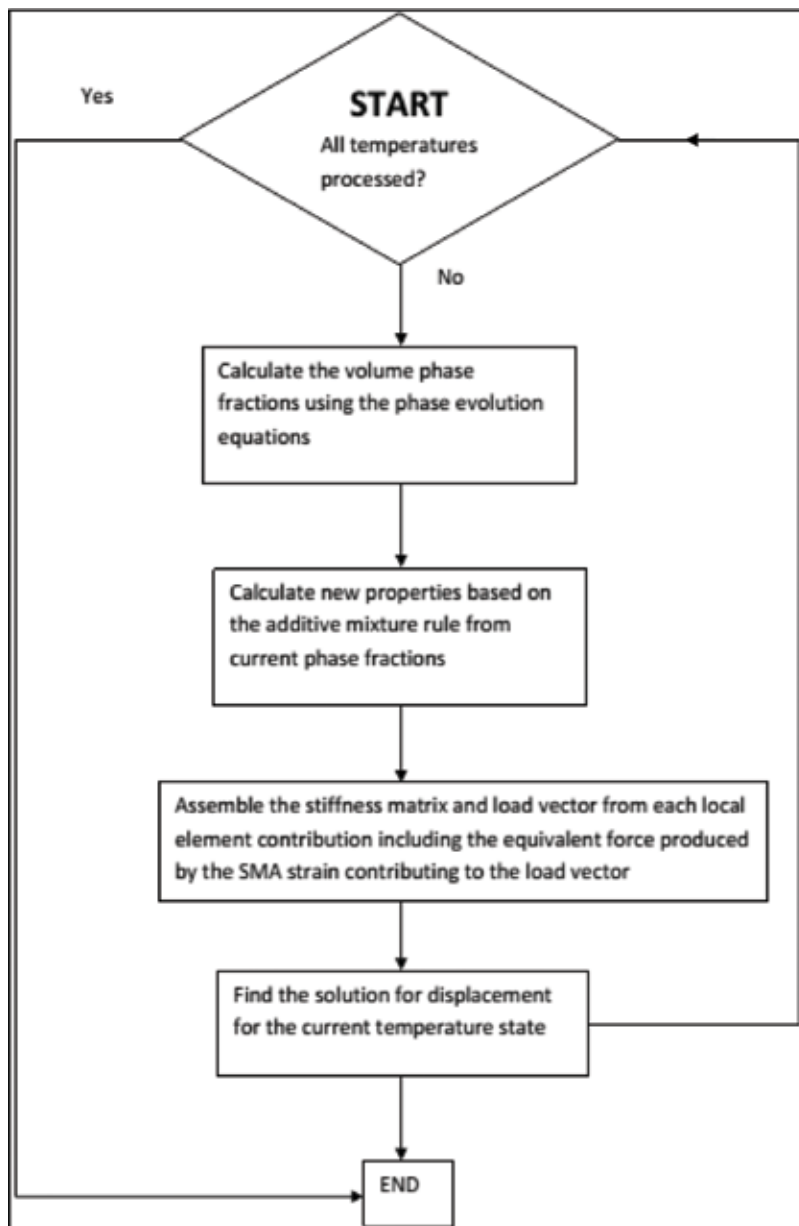


Figure 7. Finite element program solution flow process.

The force-temperature curves are shown in **Figure 9**. This graph shows the force variation which is effected by the temperature variation. The negative values indicate that the SMA wire was contracting. The maximum deflection (in **Figure 8**) was produced by a force of approximately 35.0 N (in **Figure 9**). The numerical results are in agreement with the experimental results with minor negligible difference. It can be seen from the figure that the numerical prediction follows a similar trend with experiment.

Property	Value	Units
$E_M$	16.8	GPa
$E_A$	31.8	GPa
$A_M$	0.6	$^{\circ}\text{C}^{-1}$
$A_A$	0.06	$^{\circ}\text{C}^{-1}$
$\xi_M$	0.5	—
$A_s$	43	$^{\circ}\text{C}$
$M_F$	18.3	$^{\circ}\text{C}$
$\varepsilon_L$	0.0485	mm/mm
$A_{SMA}$	1.9635E-7	$\text{m}^2$

Table 1. Measured material parameters for 0.5-mm diameter NiTi SMA wire.

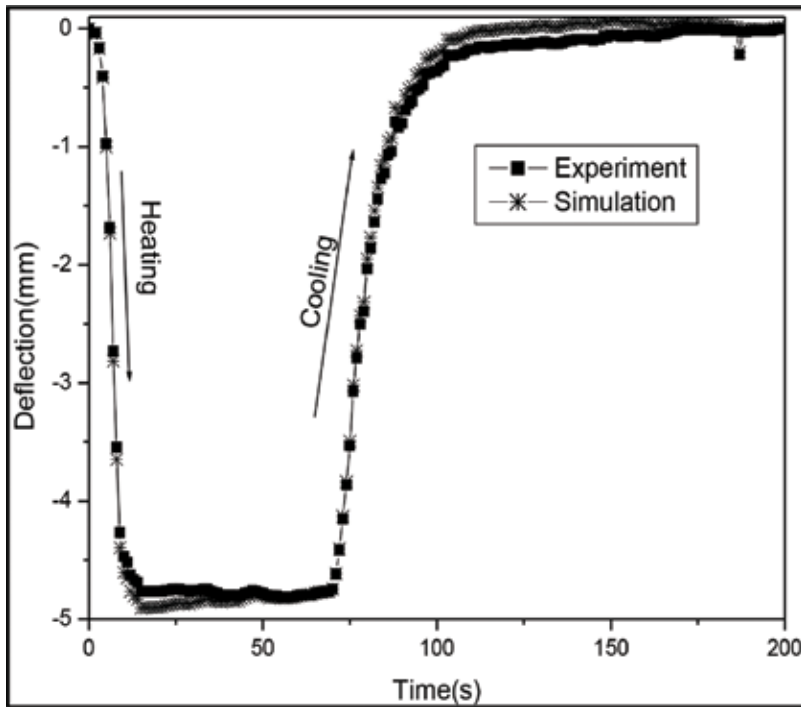


Figure 8. Deflection-time curve.

The maximum deflection for a steel beam as a function of temperature is shown in **Figure 10**. This figure shows graphical comparison between the numerical and the experimental results. The maximum deflection obtained experimentally agrees to that obtained numerically. The minor difference between the experimental and the numerical results is seen during the cooling path, and this is suggested to be caused by the uncontrolled environmental conditions. It can be concluded that the developed mathematical equations can be used to predict the behavior of smart simple structures.

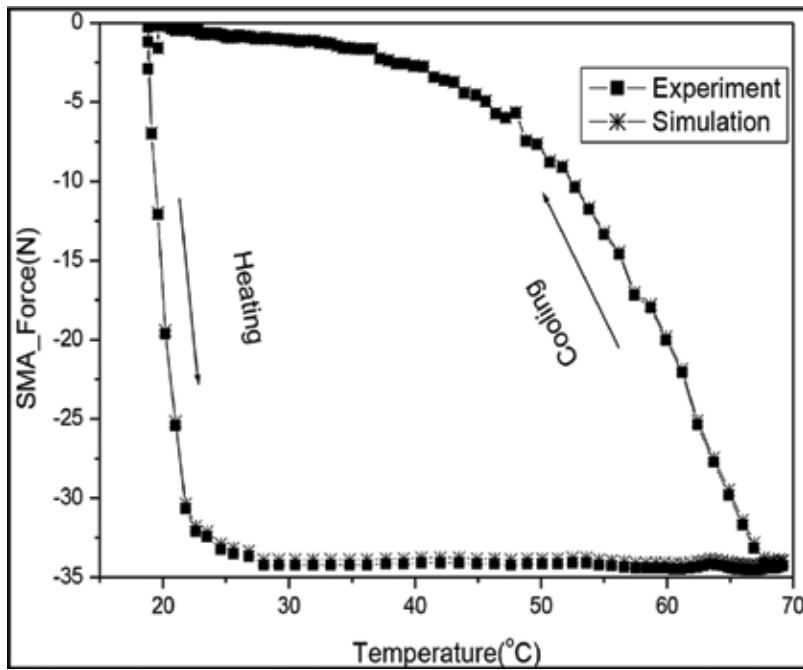


Figure 9. Force-temperature curves.

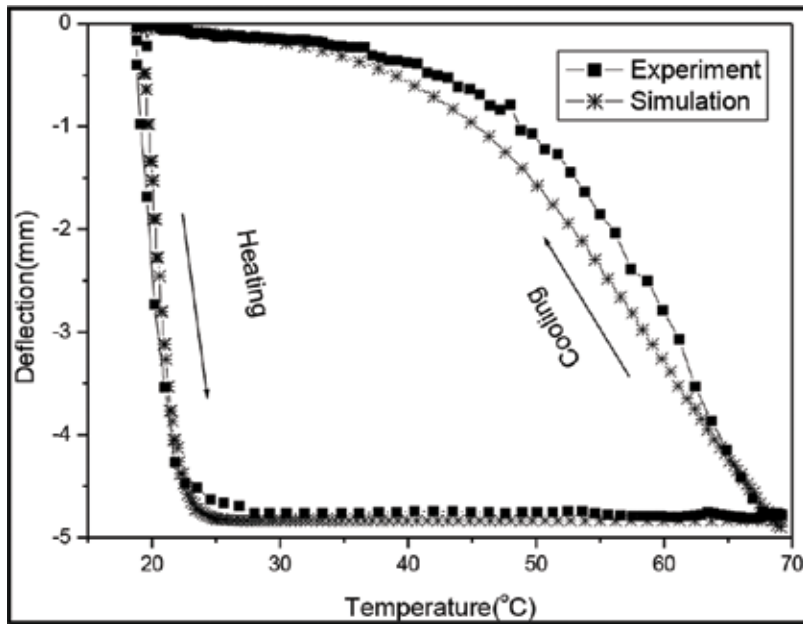


Figure 10. Experimental and numerical results for deflection-temperature curve.

## 8. Conclusion

A finite element analysis based on the proposed SMA model was performed successfully. The finite element analysis was performed on the 1D setup which was oriented on the 2D space. The C++ code was developed in order to perform the 2D numerical analysis. The experiment was performed in order to obtain the parameters to input in the developed code and also to validate the numerical results. The maximum deflection obtained numerically matches that which was measured experimentally. It was verified through the results that the developed SMA model has the ability to capture all the temperature range and not only the intended range.

### A. Beam bar elements used to solve our system presented in the main text

The element stiffness matrix in global coordinates  $(X, Y)$  is explicitly given as follows:

Element 1:

$$\left[ K^{(1)} \right] = \frac{EI}{L^3} \begin{bmatrix} 12 & 6L & -12 & 6L \\ 6L & 4L^2 & -6L & 2L^2 \\ -12 & -6L & 12 & -6L \\ 6L & 2L^2 & -6L & 4L^2 \end{bmatrix} \begin{matrix} u_1 \\ \theta_1 \\ u_2 \\ \theta_2 \end{matrix} \quad (A1)$$

Element 2:

$$\left[ K^{(1)} \right] = \frac{EI}{L^3} \begin{bmatrix} 12 & 6L & -12 & 6L \\ 6L & 4L^2 & -6L & 2L^2 \\ -12 & -6L & 12 & -6L \\ 6L & 2L^2 & -6L & 4L^2 \end{bmatrix} \begin{matrix} u_2 \\ \theta_2 \\ u_3 \\ \theta_3 \end{matrix} \quad (A2)$$

Element 3:

$$\left[ K^{(3)} \right] = \begin{bmatrix} kc^2 & ksc & -kc^2 & -ksc \\ ksc & ks^2 & -ksc & -ks^2 \\ -kc^2 & -ksc & kc^2 & ksc \\ -ksc & -ks^2 & ksc & ks^2 \end{bmatrix} = k \begin{bmatrix} c^2 & sc & -c^2 & -sc \\ sc & s^2 & -sc & -s^2 \\ -c^2 & -sc & c^2 & sc \\ -sc & -s^2 & sc & s^2 \end{bmatrix} \begin{matrix} u_{2x} \\ u_{2y} \\ u_{4x} \\ u_{4y} \end{matrix} \quad (A3)$$

$\theta = 270^0; c = 0; s = -1; cs = 0$

$$\left[ K^{(3)} \right] = \frac{AE}{L} \begin{bmatrix} 0 & 0 & 0 & 0 \\ 0 & 1 & 0 & -1 \\ 0 & 0 & 0 & 0 \\ 0 & -1 & 0 & 1 \end{bmatrix} \begin{matrix} u_{2x} \\ u_{2y} \\ u_{4x} \\ u_{4y} \end{matrix}$$

The next step is the assemblage of the above stiffness matrix to get the global stiffness matrix.

$$[K_G] = \begin{bmatrix} \frac{12EI}{L^3} & \frac{6EI}{L^2} & -\frac{12EI}{L^3} & \frac{6EI}{L^2} & 0 & 0 & 0 & 0 \\ \frac{6EI}{L^2} & \frac{4EI}{L} & -\frac{6EI}{L^2} & \frac{2EI}{L} & 0 & 0 & 0 & 0 \\ -\frac{12EI}{L^3} & -\frac{6EI}{L^2} & \frac{24EI}{L^3} & 0 & -\frac{12EI}{L^3} & \frac{6EI}{L^2} & 0 & 0 \\ \frac{6EI}{L^2} & \frac{2EI}{L} & 0 & \frac{8EI}{L} + \frac{AE}{L} & -\frac{6EI}{L^2} & \frac{2EI}{L} & 0 & \frac{AE}{L} \\ 0 & 0 & -\frac{12EI}{L^3} & -\frac{6EI}{L^2} & \frac{12EI}{L^3} & -\frac{6EI}{L^2} & 0 & 0 \\ 0 & 0 & \frac{6EI}{L^2} & \frac{2EI}{L} & -\frac{6EI}{L^2} & \frac{4EI}{L} & 0 & 0 \\ 0 & 0 & 0 & 0 & 0 & 0 & 0 & 0 \\ 0 & 0 & 0 & -\frac{AE}{L} & 0 & 0 & 0 & \frac{AE}{L} \end{bmatrix} \quad (A4)$$

The structural equation would be

$$\begin{bmatrix} F_{1x} \\ M_1 \\ F_{2x} \\ F_{2y} \\ F_{3x} \\ M_3 \\ F_{4x} \\ F_{4y} \end{bmatrix} = \begin{bmatrix} \frac{12EI}{L^3} & \frac{6EI}{L^2} & -\frac{12EI}{L^3} & \frac{6EI}{L^2} & 0 & 0 & 0 & 0 \\ \frac{6EI}{L^2} & \frac{4EI}{L} & -\frac{6EI}{L^2} & \frac{2EI}{L} & 0 & 0 & 0 & 0 \\ -\frac{12EI}{L^3} & -\frac{6EI}{L^2} & \frac{24EI}{L^3} & 0 & -\frac{12EI}{L^3} & \frac{6EI}{L^2} & 0 & 0 \\ \frac{6EI}{L^2} & \frac{2EI}{L} & 0 & \frac{8EI}{L} + \frac{AE}{L} & -\frac{6EI}{L^2} & \frac{2EI}{L} & 0 & \frac{AE}{L} \\ 0 & 0 & -\frac{12EI}{L^3} & -\frac{6EI}{L^2} & \frac{12EI}{L^3} & -\frac{6EI}{L^2} & 0 & 0 \\ 0 & 0 & \frac{6EI}{L^2} & \frac{2EI}{L} & -\frac{6EI}{L^2} & \frac{4EI}{L} & 0 & 0 \\ 0 & 0 & 0 & 0 & 0 & 0 & 0 & 0 \\ 0 & 0 & 0 & -\frac{AE}{L} & 0 & 0 & 0 & \frac{AE}{L} \end{bmatrix} \begin{bmatrix} u_1 \\ \theta_1 \\ u_2 \\ v_2 \\ u_3 \\ \theta_3 \\ u_4 \\ v_4 \end{bmatrix} \quad (A5)$$

The boundary conditions for our system are as follows:

$$\begin{aligned} F_{x1} = M_1 = F_{x3} = M_3 = F_{x2} = F_{x4} = F_{y4} &= 0 \\ u_{x1} = \theta_1 = u_{x3} = \theta_3 = u_{x4} = u_{y4} &= 0 \\ F_{y2} &= F_{SMA} \end{aligned} \quad (A6)$$

The structural equation reduces to the following equation:

$$F_{SMA} = \left( \frac{8EI}{L_{beam}} + \frac{AE}{L_{bar}} \right) U_{2y} \quad (A7)$$

The deflection could be calculated as follows:

$$\frac{F_{SMA}}{\left(\frac{8EI}{L_{beam}} + \frac{AE}{L_{bar}}\right)} = U_{2y} \quad (A8)$$

This is the deflection that needs to be solved by the FEA. It should be noted that SMA force is the only variable in this equation, and also this SMA force is calculated inside the FEA code as follows:

$$F_{SMA} = EA\varepsilon_L\xi \quad (A9)$$

## Author details

Velaphi Msomi\* and Graeme Oliver

\*Address all correspondence to: msomiv@gmail.com

Cape Peninsula University of Technology, Bellville, South Africa

## References

- [1] Paiva A, Savi MA. An overview of constitutive models for shape memory alloys. Hindawi Publishing Corporation (Mathematical Problems in Engineering). 2006;1:1-30
- [2] Tanaka K. A thermomechanical sketch of shape memory effect: One-dimensional tensile behavior. *Materials Science Research International*. 1985;18:251
- [3] Tanaka K, Nagaki S. Thermomechanical description of materials with internal variables in the process of phase transitions. *Ingenieur- Archive*. 1982;51:287-299
- [4] Boyd JG, Lagoudas DC. A thermodynamic constitutive model for the shape memory materials. Part I: The monolithic shape memory alloys. *International Journal of Plasticity*. 1996;12(6):805-842
- [5] Liang C, Rogers CA. One-dimensional thermomechanical constitutive relations for shape memory materials. *Journal of Intelligent Material Systems and Structures*. 1990;1:207-234
- [6] Anders WS, Rogers CA, Fuller CR. Vibration and low-frequency acoustic analysis of piecewise-activated adaptive composite panels. *Journal of Composite Materials*. 1992;26:103-120
- [7] Rogers CA, Liang C, Fuller CR. Modeling of shape memory alloy hybrid composites for structural acoustic control. *Journal of Acoustic Society of America*. 1991;89(1):210-220

- [8] Brinson LC. One-dimensional constitutive behaviour of shape memory alloys: Thermomechanical derivation with non-constant material functions and redefined martensite internal variable. *Journal of Intelligent Materials and Structures*. 1993;**4**(2):229-242
- [9] Rajapakse RKND, Sun S. Simulation of pseudoelastic behaviour of SMA under cyclic loading. *Computational Materials Science*. 2003;**28**:663-674
- [10] Msomi V, Oliver GJ. Smart morphing based on shape memory alloy plate. *Journal of Engineering, Design and Technology*. 2016;**14**(3):475-488
- [11] Lagoudas DC, editor. *Shape Memory Alloys: Modeling and Engineering Applications*. New York: Springer; 2008
- [12] Buravalla V, Khandelwal A. Evolution kinetics in shape memory alloys under arbitrary loading: Experiments and modeling. *Journal of Mechanics and Materials*. 2011;**43**:807-823
- [13] Kamrani M, Kadkhodaei M. Investigation on local and global behaviours of pseudo elastic shape memory alloy wires in simple tensile test considering stress concentration of grippers. *Journal of Intelligence Material Systems and Structures*. 2015;**27**:221-232
- [14] Zare F, Kadkhodaei M, Salafian I. Thermomechanical modelling of stress relaxation in shape memory alloy wires. *Journal of Material Engineering and Performance*. 2015;**24**(4): 1763-1770
- [15] Shirani M, Kadkhodaei M. One dimensional constitutive model with transformation surfaces for phase transition in shape memory alloys considering the effect of loading history. *International Journal of Solids and Structures*. 2016;**81**:117-129



---

# Experiments and Models of Thermo-Induced Shape Memory Polymers

---

Qianhua Kan, Jian Li, Guozheng Kang and  
Zebin Zhang

Additional information is available at the end of the chapter

<http://dx.doi.org/10.5772/intechopen.78012>

---

## Abstract

Recent advances in experiments and models of thermo-induced shape memory polymers (TSMPs) were reviewed. Some important visco-elastic and visco-plastic features, such as rate-dependent and temperature-dependent stress-strain curves and nonuniform temperature distribution were experimentally investigated, and the interaction between the mechanical deformation and the internal heat generation was discussed. The influences of loading rate and peak strain on the shape memory effect (SME) and shape memory degeneration of TSMPs were revealed under monotonic and cyclic thermo-mechanical loadings, respectively. Based on experimental observations, the capability of recent developed visco-elastic and visco-plastic models for predicting the SME was evaluated, and the thermo-mechanically coupled models were used to reasonably predict the thermo-mechanical responses of TSMPs.

**Keywords:** shape memory polymers, thermo-mechanical coupling, constitutive models, glassy transition, relaxation

---

## 1. Introduction

Thermo-induced shape memory polymers (TSMPs) are one of most widely applicable shape memory polymers (SMPs) at present, which exhibit the shape memory effect (SME) by changing the ambient temperature. TSMPs are different from the traditional polymers; some of their important features related to the SME were summarized by Lendlein et al. [1] and Hager et al. [2] as follows: (1) a phase presents the rubber-like state in a wide temperature range above the glassy transition temperature ( $T_g$ ) and has a stable strength to deform; (2) a

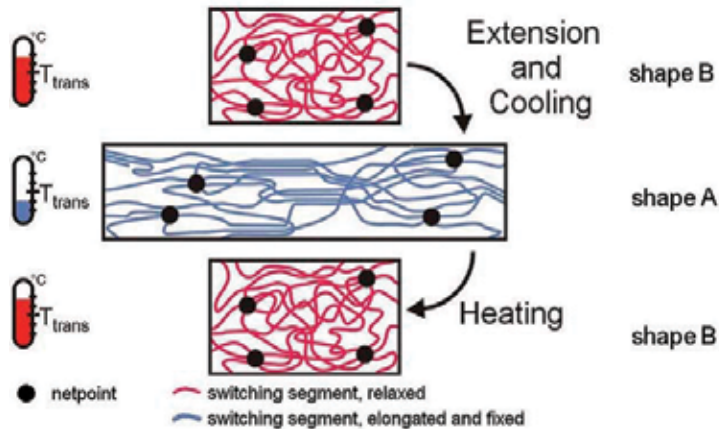


**Figure 1.** The molecular mechanism of the SME of TSMPs [3].

phase presents the glass-like state in a wide temperature range below  $T_g$  and has a stable strength to ensure that the internal stress is not be released in storage; (3) The two separable phases are the structural basis of SME and the suitable ratio between the two phases should be existent. The molecular mechanism of TSMPs was presented by Behl et al. [3], as shown in **Figure 1**. There are three parts in TSMPs, including the netpoint, the relaxed switching segment, the elongated and fixed switching segment (i.e., the transition phase, it can transform between the netpoint and the relaxed switching segment with the change of temperature).

The popular topics focus on the fabrications, the analysis of mechanisms and applications of TSMPs [3–5]. The constitutive models describing the glassy transition mechanism of TSMPs are summarized and they can be divided into two types according to different deformation mechanisms, including the thermo-visco-elastic rheology model and the meso-mechanical model [6]. The thermo-visco-elastic model can describe the mobility of chain segments and relaxation with temperature by introducing the relaxation time and the temperature-dependent modulus. The meso-mechanical model adopted a mixture rule of rubber and glassy phases by the volume fractions of frozen and active phases. For considering the interaction between the internal heat generation and mechanical deformation, the thermo-mechanically coupled models were developed by introducing different dissipation mechanisms.

In this chapter, recent advances in experiments and models of TSMPs are reviewed. According to experimental observations, some deformation mechanisms and features of TSMPs are summarized. The capability of two types of models in predicting the mechanical responses and the SME of TSMPs are evaluated, and some interesting issues and further developments of TSMPs were discussed in the end.

## 2. Experiment observations

### 2.1. Mechanical performances

The mechanical properties of TSMPs are strongly sensitive to the ambient temperature and the loading rate and can be obtained from tensile experiments at different temperatures and loading rates, as shown in **Figure 2**.

It is found from **Figure 2** that the high-stress responses at low temperature is a typical feature of amorphous polymers, and the low stress responses at high temperature is a typical feature of visco-elastic polymer. The yield peak gradually disappears when the temperature goes beyond the glassy transition temperature  $T_g$ .

The thermo-mechanical properties can be obtained from the dynamic mechanical analysis (DMA) [7]. As shown in **Figure 3**, the storage and loss moduli obtained from DMA are found as functions of temperature. The glassy transition temperature, where the ratio of loss modulus and storage modulus ( $\tan \delta$ ) dramatically changes, can be obtained from the DMA results, and the glassy transition temperature increases with the frequency [8]. In addition, the glassy transition temperature can be also obtained from the differential scanning calorimeter (DSC) test [9].

### 2.2. Thermo-mechanical coupling behaviors

The thermo-mechanical coupling behaviors are divided into two types here, one is that the mechanical behavior changes with the ambient temperature, that is, SME; the other is the temperature changes induced by the internal heat generation.

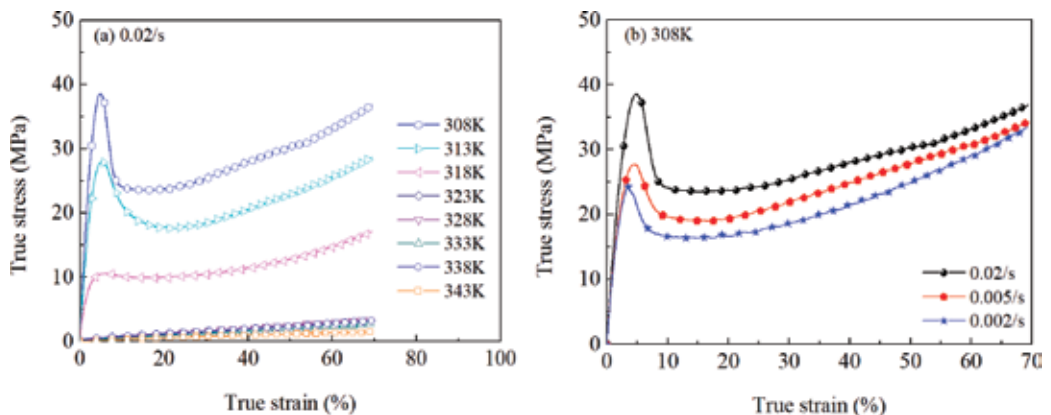


**Figure 2.** Stress-strain curves of monotonic tension at (a) different temperatures and (b) loading rates.

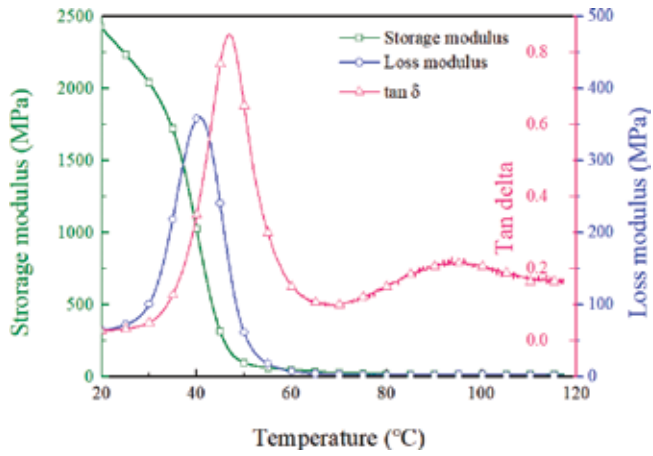


Figure 3. The curves of storage modulus, loss modulus, and  $\tan\delta$  versus temperature.

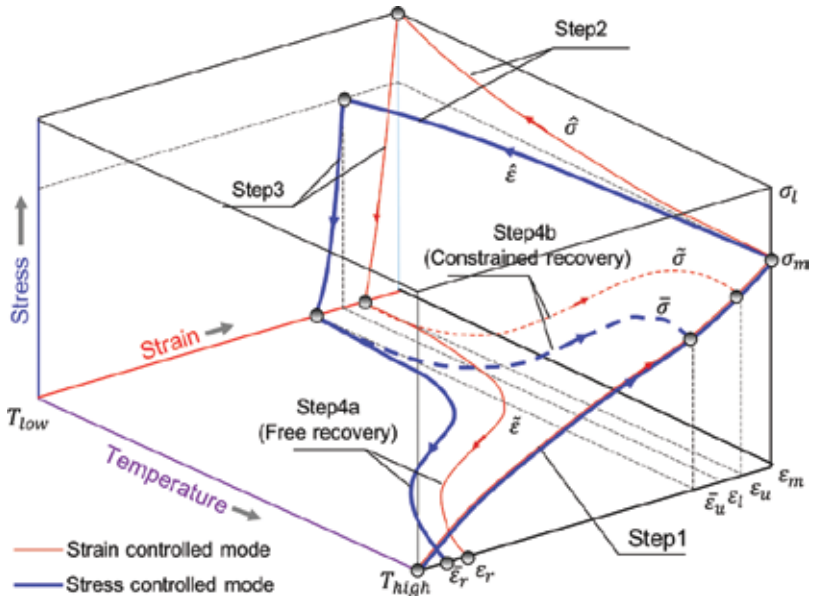


Figure 4. The illustration of SME of TSMPs.

2.2.1. Shape memory effect

As shown in **Figure 4**, a typical SME process includes four stages, that is, Step1: deforming at high temperature above  $T_g$ ; Step2: cooling to the storage temperature (room temperature in general); Step3: unloading at the storage temperature and the shape is fixed; Step4: heating to the recoverable temperature above  $T_g$ , the deformed shape returns to the initial undeformed shape.

The SME process can be divided into stress-controlled (stress-free recovery) and strain-controlled (strain-constraint recovery) modes during strain recovery by heating, respectively. Two parameters are usually used to character the SME, including the shape fixity ratio  $R_f$  and the shape recovery ratio  $R_r$  [10, 11] as shown in Eqs. (1) and (2).

$$R_f = \frac{\varepsilon_u}{\varepsilon_m} \times 100 \quad (1)$$

$$R_r = \frac{\varepsilon_m - \varepsilon_r}{\varepsilon_m} \times 100 \quad (2)$$

where  $\varepsilon_m$ ,  $\varepsilon_u$  and  $\varepsilon_r$  denote the peak strain, fixed strain and residual strain, respectively.

Besides, the recoverable glassy transition temperature in the stress-free recovery, the maximum recovery stress in the constraint recovery and the recoverable temperature at the maximum recovery stress are also used to quantify the SME [10–13].

The experimental results of TSMPs sheet (MM4520) at different strain rates and peak strains are shown in **Figure 5**.

It is found from **Figure 5** that the maximum stress at the cooling stage decreases with the increase of loading rate, and the shape recovery ratio of TSMPs in the stress-free recovery decreases with the increase of peak strain and the decrease of strain rate, which is similar with shape memory experiments of TSMPs sheet (MS4510) [14]. It is the reason that the viscosity increases with the increase of strain rate and the damage in chain segments increases with the increase of peak strain. The correlation between the loading rate and the shape recovery ratio can be explained, as the relaxation of the stored elastic energy is easier at low loading rate than at high loading rate. However, the SME in the stress-free recovery is independent on the peak strain; the recovery maximum stress increases with the increase of peak strain for the aliphatic polyether urethane [13].

In the molecular level, a prior orientation of switching chain segments of thermoplastic TSMPs improves with the increase of macroscopic deformation; once these chain segments return to the random coil-like conformation, the maximum recovery stress increases in the strain-constraint recovery. However, the peak strain has almost no influence on the SME for the

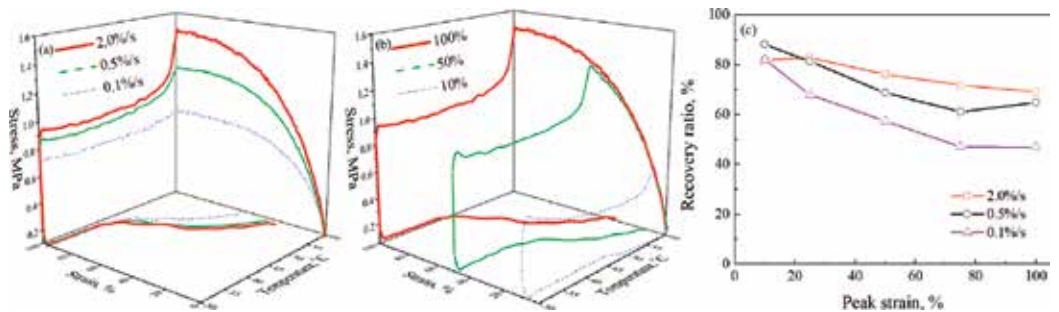


**Figure 5.** Stress-strain-temperature curves at different (a) strain rates, (b) peak strains, and (c) shape recovery ratio versus peak strain at different strain rates.

thermoset TSMPs [12, 15] since the thermoset TSMPs have a more stable molecular structure than the thermoplastic TSMPs.

Hu et al. [14] found that TSMPs film (MS4510) exhibits an excellent SME at the temperature range from  $T_g$  to  $T_g + 25^\circ\text{C}$ , and the shape recovery ratio decreases beyond the temperature range. To obtain better SME in practical applications, the TSMPs film should be cooled to its frozen state as soon as possible after being deformed at high temperature. Cui and Lendlein [13] found the switching temperature of shape recovery in the stress-free recovery, the maximum recovery stress and the corresponding temperature in the strain-constraint recovery increase with the increase of deformation temperature. The start temperature of shape recovery can be controlled by adjusting the cooling temperature during unloading [16].

Besides, many factors can remarkably affect the shape recovery ratio, for example, the shape recovery ratio decreases with the increase of holding time after deformation since the increase of holding time causes a large relaxation of the stored elastic energy [17, 18]. The shape recovery ratio increases with the increase of finish recovery temperature since the mobility of chain segments is more active at high temperature [14, 18]. If the recovery temperature is higher than the deformation temperature, the inactive chain segments during the deforming stage can be activated to increase their mobility. The shape recovery ratio increases with the decrease of heating rate since the heat conduction of TSMPs requires enough time. If the holding time increases after approaching the finish recovery temperature, the effect of heating rate on the shape recovery ratio can be eliminated [15].

According to the experiment results, the mobility of chain segments, visco-elasticity, stress relaxation and structural relaxation of TSMPs also have influences on the SME. These influential factors change with temperature and can be utilized to optimize the SME.

### *2.2.2. Internal heat generation induced by deformation*

TSMPs are sensitive to the temperatures, including the temperature caused by the internal heat generation and ambient temperature. According to the thermo-mechanically coupled experiments [8, 19, 20], an infrared camera is used to measure the surface temperature of TSMPs for indicating the interaction between mechanical deformation and temperature. It is concluded that TSMPs are very sensitive to the temperature and loading rate, and the temperature localization is related to the strain localization, as shown in **Figures 6–8**. The temperature firstly decreases during the elastic deformation stage and then increases during visco-plastic deformation stage in tension, which implies that the internal heat generation is contributed by two parts, that is, the decreased temperature due to the thermo-elastic effect and the increased temperature due to the visco-plastic dissipation. It is noted from **Figure 7** that the temperature variation increases with the increase of loading rate and it can be explained as with the increase of loading rate in tension, the resistance of the slipping of chain segments increases, which results in a larger dissipation caused by the friction of disentanglement of chain segments.

The stress-strain curves and temperature variations of TSMPs subjected to loading-unloading mechanical cycles were obtained by Pieczynska et al. [20], as shown in **Figure 9**. It is found that the residual strain accumulates and the amplitude of temperature variation decreases with the

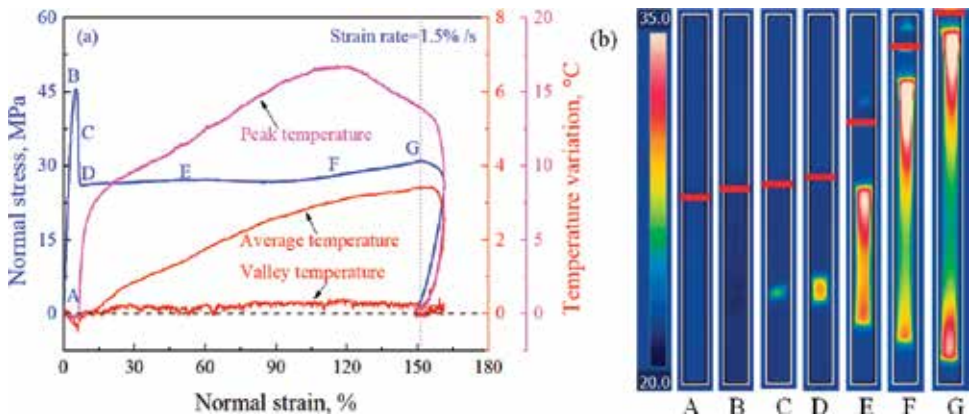


Figure 6. (a) Curves of stress-strain and strain-temperature variation; and (b) temperature field distribution.

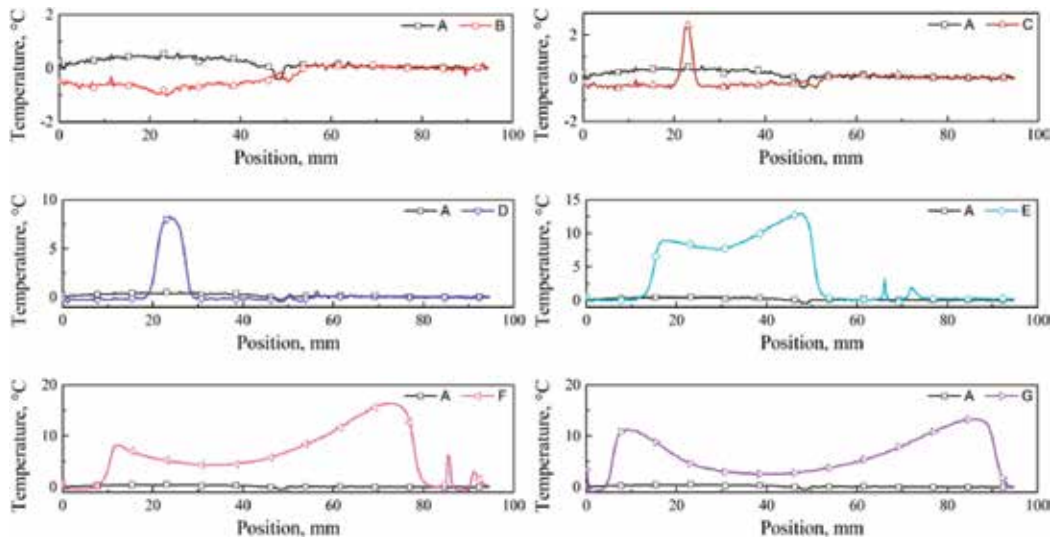
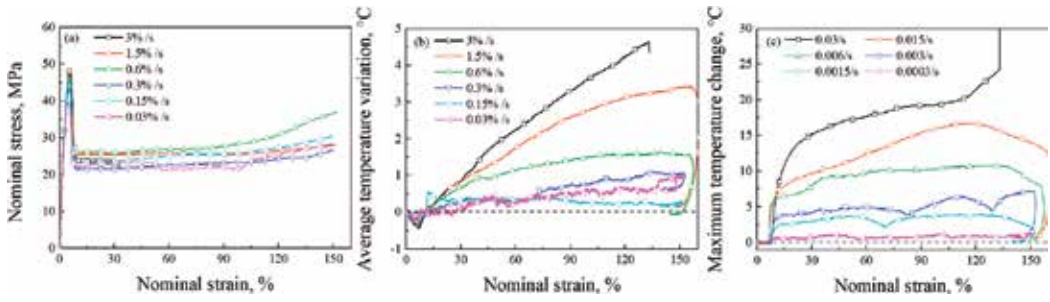


Figure 7. Curves of temperature versus position corresponding to Figure 6(b).

increase of number of cycles. It is the reason that the decreased stress at peak strain due to the stress relaxation and the accumulated residual strain after unloading result in a narrower and narrower hysteresis loop, that is, decreased visco-plastic dissipation with the increase of number of cycles.

### 2.3. Shape memory degradation

When the TSMPs are subjected to thermo-mechanical cyclic loadings (i.e., repeated shape memory cycles), the shape memory degradation can be characterized by the strain recovery rate  $R_{rate}$  [11, 21] and strain recovery ratio  $R_{ratio}$  [22], respectively, as below:



**Figure 8.** (a) Stress-strain curves; (b) curves of average temperature variation versus strain; and (c) curves of maximum temperature variation versus strain.

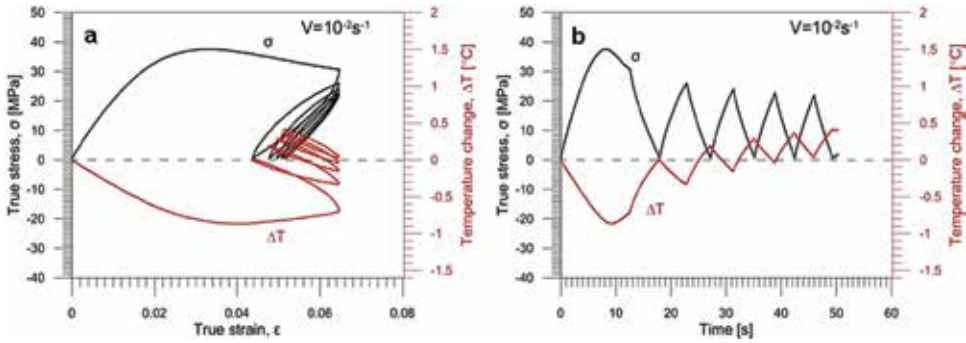


**Figure 9.** Stress and temperature change of TSMPs subjected to loading-unloading cycles versus (a) true strain and (b) time [20].

$$R_{\text{rate}}(N) = \frac{\epsilon_u(N) - \epsilon_r(N)}{\epsilon_u(N) - \epsilon_r(N-1)} \times 100 \quad (3)$$

$$R_{\text{ratio}}(N) = \frac{\epsilon_m - \epsilon_r(N)}{\epsilon_m} \times 100 \quad (4)$$

where  $\epsilon_m$  denotes the peak strain during loading,  $\epsilon_u(N)$  and  $\epsilon_r(N)$  denote the fixed strain and residual strain after unloading in the  $N$ -th cycle, respectively.

The experimental results subjected to shape memory cycles are shown in **Figure 10** [11, 22]. It is found that the strain recovery rate gradually increases with the decrease of peak strain and the increase of number of cycles and rapidly approaches 100% after several cycles. However, the recovery strain ratio depends on the peak strain, for example, it increases with the increase of peak strain; however, it decreases when the peak strain is up to 150%.

The shape memory degeneration also depends on the deformable temperature, recovery temperature and mechanical training [22–25]. For example, as shown in **Figure 11**, the strain

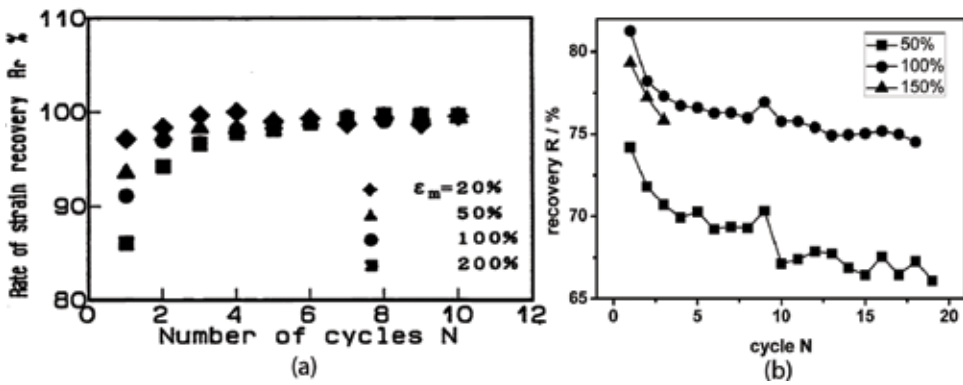


Figure 10. Curves of (a) the strain recovery rate [11] and (b) the strain recovery ratio [22] with number of cycles.

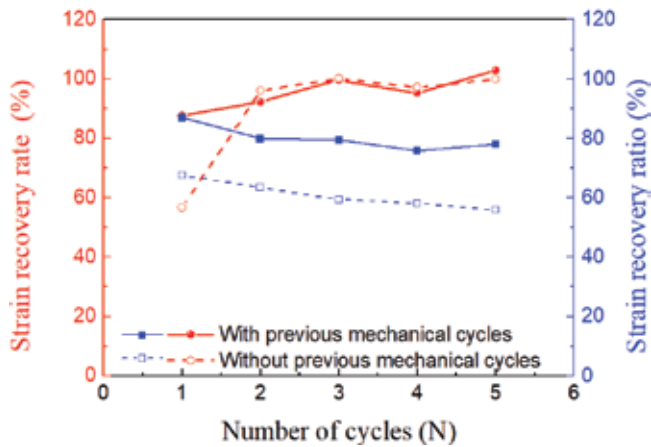


Figure 11. The influences of previous mechanical cycles on the strain recovery rate and strain recovery ratio [25].

recovery ratio of TSMPs can be improved by undergoing previous mechanical cycles since the mechanical training can eliminate the heterogeneous structure of chain segments [24]. However, the previous mechanical cycles have almost no influence on strain recovery rate.

#### 2.4. Novel experimental observations on SME

Conventional experimental methods limited within uniaxial tension or compression were discussed in Sections 2.1–2.3. Recently, many advanced experimental methods and complex loading modes were developed to investigate the SME of TSMPs. For example, the nano-indentation technology was used to examine the SME of TSMPs, and the indentation can be recovered by heating the sample to above the glass transition temperature [26]; this research provides a foundation to explore the nano-mechanical behavior of TSMPs.

The shear deformation and its recovery behavior were investigated through a double lap joint arrangement at below and above  $T_g$  [27]. Torsional shape memory tests were carried out to characterize the SME, and a torsional device with a CCD camera was used to quantify the parameters of the SME [28]. A series of tension, compression, bending and twisting experiments of TSMPs were performed to indicate the SME; it is shown that the heating rate has an obvious influence on the start temperature of shape recovery [29].

These experimental findings provide an experimental guidance for future applications, including aerospace, automotive, robotics, and smart actuator, and so on. Some novel experiments and protocols are expected to be designed for characterizing the SME of smart structures in future.

### 3. Constitutive models

Constitutive models of TSMPs, including shape memory model describing the SME and the thermo-mechanically coupled model describing the internal heat generation caused by mechanical deformation, are commented on in this section.

#### 3.1. Shape memory model

Based on the different deformation mechanisms, different models were constructed to describe the SME of TSMPs, including the rheology model considering the mobility and relaxation and the meso-mechanical model considering the phase transition between the frozen and active phases.

##### 3.1.1. Rheology model

The mobility of chain segments is a classical mechanism to describe the SME, which remarkably depends on ambient temperature. Tobushi et al. [21] think that the shape of TSMPs can be fixed due to the decreased mobility of chain segments with the decrease of temperature, and the shape can be recovered due to the increased mobility of chain segments with the increase of temperature. Therefore, a rheological model was proposed by introducing a slip element into a three-element standard linear visco-elastic model, as shown in **Figure 12**, and the mobility of chain segments can be expressed as the exponential functions between material parameters and temperature, as shown in Eq. (5).

$$x(T) = \begin{cases} x(T_l) & (T \leq T_l) \\ x_g \exp \left[ a_x \left( \frac{T_g}{T} - 1 \right) \right] & (T_l \leq T \leq T_h) \quad (x = E, \mu, \lambda, C, \varepsilon_l) \\ x(T_h) & (T \geq T_h) \end{cases} \quad (5)$$

where,  $\sigma$ ,  $\varepsilon$  and  $\varepsilon_l$  denote the stress, strain and irrecoverable strain,  $E$  is elastic modulus.  $\mu$  and  $\lambda$  are viscosity and retardation time, respectively.  $C$  is a coefficient of irrecoverable strain.  $T$ ,  $T_l$ ,  $T_g$ ,  $T_h$  and  $a_x$  denote the current temperature, low temperature, glassy transition temperature, melting temperature and proportional coefficient, respectively.

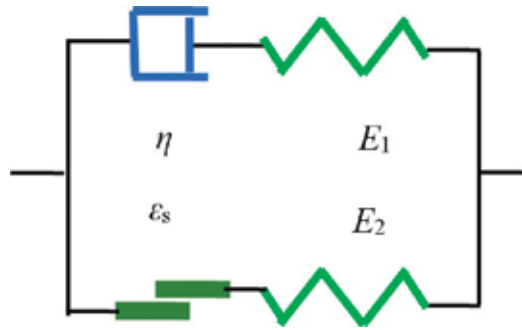


Figure 12. Four-element model.

To describe the nonlinear behaviors of TSMPs, a one-dimensional nonlinear visco-elastic model was extended from a linear visco-elastic version [30]. However, the extended model provides an overestimation of the responded stress at large strain, and thus the linear model was further modified to reasonably simulate the SME of TSMPs at large strain by introducing new nonlinear evolution equations with stress threshold values into the cooling modulus and irrecoverable strain [31].

It is noted that, even though the mechanical responses at large strain were simulated, the abovementioned models were established at small deformation. Therefore, Diani et al. [32] developed a thermo-mechanical model of TSMPs at finite deformation based on the three element standard linear visco-elastic model [21]. The total deformation gradient is decomposed into elastic and viscous parts. The total Cauchy stress includes the stresses caused by the entropy change and internal energy change, respectively.

Nguyen et al. [33] developed a thermo-visco-elastic model to describe the time-dependent and temperature-dependent deformations of TSMPs by incorporating structural relaxation and stress relaxations. The model can reproduce the strain-temperature response, rate-dependent stress-strain response and some important features of temperature dependent shape memory responses. In the model, a fictive temperature  $T_f$  is used to describe the structural relaxation behavior and the structural relaxation time is obtained from the WLF equation, as shown in Eq. (6). The stress relaxation adopts the form of visco-elasticity in the glass transition region and rubbery state, and the modified WLF equation is introduced into the Eyring equation to obtain a modified visco-plastic flow rule for describing the visco-plastic deformation, including the glassy state and rubbery state, see Eq. (7).

$$\tau_R(T, T_f(\bar{\delta}^{neq})) = \tau_{Rg} \exp \left[ -\frac{C_1}{\log e} \left( \frac{C_2(T - T_f) + T(T_f - T_g^{ref})}{T(C_2 + T_f - T_g^{ref})} \right) \right] \quad (6)$$

$$\dot{\gamma}^v = \frac{s_y}{\sqrt{2}\eta_s^{ref}} \frac{T}{Q_s} \exp \left[ \frac{C_1}{\log e} \left( \frac{C_2(T - T_f) + T(T_f - T_g^{ref})}{T(C_2 + T_f - T_g^{ref})} \right) \right] \sinh \left( \frac{Q_s \|\mathbf{s}^{neq}\|}{T \sqrt{2}s_y} \right) \quad (7)$$

where  $\tau_R$  and  $\tau_{Rg}$  are the structural relaxation time and relaxation time at a reference temperature  $T_g^{ref}$ , respectively;  $C_1$  and  $C_2$  are material constants using in the WLF equation.  $\bar{\delta}^{neq}$  denotes the nonequilibrium part of the isobaric volumetric deformation.  $\dot{\gamma}^v$  and  $s_y$  denote the effective viscous shear stretch rate and yield strength.  $Q_s$  is a thermal activation parameter and  $\mathbf{s}^{neq}$  is the nonequilibrium part of the deviatoric component of Cauchy stress.

Based on the model proposed by Nguyen et al. [33], Li et al. [7] also developed a thermo-visco-elastic-visco-plastic model considering the structural relaxation and stress relaxation. The model was used to predict the nonlinear SME of TSMPs programmed by cold-compression below the glassy transition temperature. Chen et al. [34] performed parameter studies on the SME in the conditions of the stress-free recovery and strain-constrained recovery with different loading parameters, including the cooling rate, heating rate, strain rate, anneal time and temperature. The results show that the SME is affected by different mechanisms, including the thermal expansion, structural relaxation and stress relaxation. Chen et al. [35] developed a rheological model by introducing the thermal expansion, structural relaxation and stress relaxation into a standard linear visco-elastic model; the Mooney-Rivlin function and Newton fluid assumptions were used to describe the hyper-elasticity of rubbery state and flow behavior of glassy state during the process of the glass transition, respectively.

Recently, the multibranch models considering the stress relaxation were developed to reasonably capture the SME of TSMPs [16, 36–38]. For considering more complex shape memory behaviors, Xiao et al. [39] proposed a thermo-visco-plastic model at finite deformation to describe the multiple SME and temperature memory effect by introducing the structural relaxation and stress relaxation [39]. Besides, for the purpose of the structural analysis, the linear visco-elastic model [21] was extended to three-dimensional version and was implemented into ABAQUS by using the user material subroutine UMAT to simulate the SME of structures [40–43].

### 3.1.2. Meso-mechanical model

The meso-mechanical model was firstly proposed by Liu et al. [44] to describe the physical mechanisms of the stress-free recovery and strain-constraint recovery at the pre-deformation strain level of TSMPs. In the model, it is assumed that the TSMPs consist of two extreme phases, including the frozen phase and active phase. The frozen phase is the major phase in the glassy state, where the conformational motion is constrained. In contrast, the active phase exists in the full rubbery state, and the free conformational motion potentially occurs. By changing the ratio of these two phases, the glassy transition in a thermo-mechanical cycle is embodied and thus the shape memory effect can be captured. To quantify the changes of mechanical properties with temperature, the volume fraction of frozen phase is defined as Eq. (8) and can be obtained by fitting the curve of recovery strain. It is assumed that the corresponding stresses in these two phases are equal to  $\boldsymbol{\sigma}$  (see Eq. (9)), and the total strain  $\boldsymbol{\varepsilon}$  is defined as Eq. (10).

$$\phi_f = 1 - \frac{1}{1 + c_f(T_h - T)^n} \quad (8)$$

$$\boldsymbol{\sigma} = \phi_f \boldsymbol{\sigma}_f + (1 - \phi_f) \boldsymbol{\sigma}_a, \boldsymbol{\sigma}_f = \boldsymbol{\sigma}_a = \boldsymbol{\sigma} \quad (9)$$

$$\boldsymbol{\varepsilon} = \phi_f \boldsymbol{\varepsilon}_f + (1 - \phi_f) \boldsymbol{\varepsilon}_a \quad (10)$$

where  $\phi_f$  denotes the volume fraction of frozen phase;  $\boldsymbol{\sigma}$  is the total stress;  $\boldsymbol{\sigma}_a$  and  $\boldsymbol{\sigma}_f$  are the stresses in the active phase and frozen phase, respectively;  $\boldsymbol{\varepsilon}$  is the total strain; and  $\boldsymbol{\varepsilon}_a$  and  $\boldsymbol{\varepsilon}_f$  are the strains in the active phase and frozen phase, respectively.

Based on the meso-mechanical model [44], the thermo-elastic models [45, 46] were constructed to simulate the SME of TSMPs at small deformation and large deformation, respectively. Qi et al. [47] assumed that the TSMPs consist of three phases, including the rubbery phase, initial glassy phase and frozen glassy phase. The volume fraction of each phase is assumed as the function of temperature, as shown in Eq. (11). The volume fraction of rubbery phase  $\phi_r$  is defined as Eq. (12) during cooling and heating. The volume fraction of rubbery phase transforms into the volume fraction of frozen glassy phase during cooling. It is assumed that the increments in the volume fractions of the initial glassy phase  $\phi_{g0}$  and frozen glassy phases  $\phi_T$  depend on their relative volume fraction during reheating, as shown in Eq. (12). In the meantime, the corresponding stresses in the three phases satisfy with the rule of mixture, see Eq. (13).

$$\phi_g + \phi_r = 1, \quad \phi_{g0} + \phi_T = \phi_g \tag{11}$$

$$\phi_r = \frac{1}{1 + \exp[-(T - T_r)/A]}, \quad \Delta\phi_{g0} = \frac{\phi_{g0}}{\phi_{g0} + \phi_T} \Delta\phi_g, \quad \Delta\phi_T = \frac{\phi_T}{\phi_{g0} + \phi_T} \Delta\phi_g \tag{12}$$

$$\mathbf{T} = \phi_r \mathbf{T}_r + \phi_{g0} \mathbf{T}_{g0} + \phi_T \mathbf{T}_T \tag{13}$$

where  $\mathbf{T}$  is the total stress.  $\mathbf{T}_r$ ,  $\mathbf{T}_{g0}$  and  $\mathbf{T}_T$  denote stress in the rubbery phase, frozen phase and initial glassy phase, respectively.

Based on the abovementioned meso-mechanical method with a mixture rule, a three-dimensional model was proposed for TSMPs [48], which distinguishes between two phases presenting different properties. The model can reproduce both heating-stretching-cooling and cold drawing shape-fixing procedures and was applied in the simulations from simple uniaxial and biaxial tests to complex loadings of biomedical devices.

### 3.2. Thermo-mechanically coupled model

Pieczyska proposed thermo-mechanically coupled models at finite deformation [8, 19] to reproduce the rate-dependent stress-strain curve and the strain localization behavior. However, this model cannot describe the temperature variation induced by the internal heat generation since the thermo-elastic effect and the visco-plastic dissipation are neglected. To reasonably describe the influence of the internal heat generation on the mechanical behavior of TSMPs, the Helmholtz free energy  $\psi$  is decomposed into three parts, that is, the instantaneous elastic free energy  $\psi^e$ , visco-plastic free energy  $\psi^{vp}$  and heat free energy  $\psi^T$ , and the stress-strain relationship is derived from the Helmholtz free energy [49], as shown in Eqs. (14)–(17).

$$\psi(\mathbf{C}^e, \mathbf{B}^{vp}, T) = \psi^e(\mathbf{C}^e, T) + \psi^{vp}(\mathbf{B}^{vp}, T) + \psi^T(T) \tag{14}$$

$$\psi^e(\mathbf{E}^e, T) = G(T)|\mathbf{E}_0^e|^2 + \frac{1}{2}K(T)|\text{tr}(\mathbf{E}^e)|^2 - 3K(T)\text{tr}(\mathbf{E}^e)\alpha(T - T_0) \tag{15}$$

$$\psi^{VP}(\lambda^{VP}, T) = \mu_R(T)\lambda_L^2 \left[ \left( \frac{\lambda^{VP}}{\lambda_L} \right) x + \ln \left( \frac{x}{\sinh x} \right) \right], \quad x = \mathcal{L}^{-1} \left( \frac{\lambda^{VP}}{\lambda_L} \right) \quad (16)$$

$$\psi^T(T) = c \left[ (T - T_0) - T \ln \left( \frac{T}{T_0} \right) \right] + u_0 - \eta_0 T \quad (17)$$

where  $\mathbf{C}^e$ ,  $\mathbf{B}^{VP}$  denote the elastic right Cauchy-Green tensor and visco-plastic left Cauchy-Green tensor, respectively.  $\mathbf{E}^e$  and  $\mathbf{E}_0^e$  are the Hencky's logarithmic strain and its deviatoric part, respectively.  $T_0$  is the initial temperature.  $\lambda^{vp}$  and  $\lambda_L$  denote the visco-plastic stretch and limiting stretch, respectively.  $u_0$  and  $\eta_0$  denote the initial internal energy and initial entropy, respectively.  $\mu_R$ ,  $G$  and  $K$  denote the temperature-dependent hardening modulus, shear modulus and bulk modulus, respectively. The parameter  $c$  denotes the specific heat, and the symbol  $\mathcal{L}^{-1}$  denotes the inverse of Langevin function.

The heat equilibrium equation of the internal heat generation and heat exchange is derived based on an average temperature filed along the sample, as shown in Eq. (18).

$$c_{\text{eff}} \dot{T} = \omega \Gamma_{\text{eff}} + \frac{h(T_0 - T)S}{V} \quad (18)$$

where  $h$  is the heat exchange coefficient of ambient media, which is a constant if without forced convection.  $c_{\text{eff}}$  and  $\Gamma_{\text{eff}}$  are the equivalent specific heat and dissipation, respectively,  $S$  and  $V$

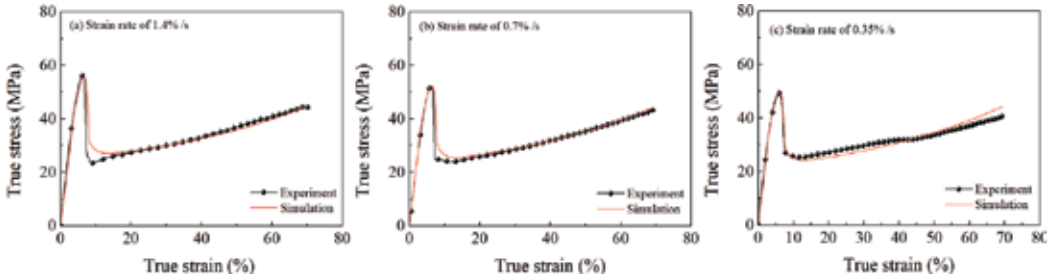


**Figure 13.** Experimental and simulated stress-strain curves at different strain rates: (a) 1.4%/s; (b) 0.7%/s; and (c) 0.35%/s.

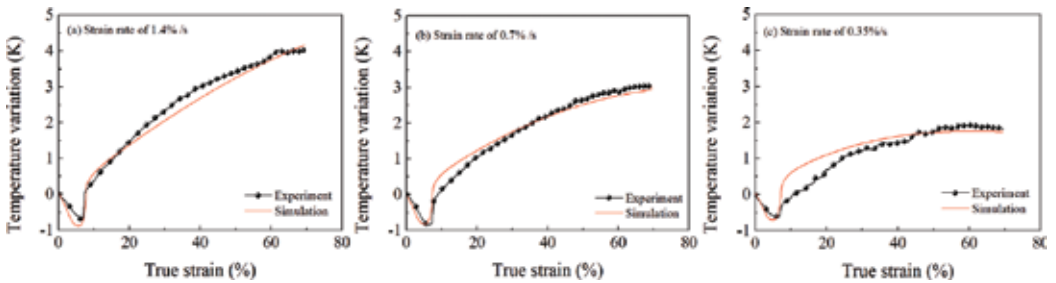


**Figure 14.** Experimental and simulated temperature variation at different strain rates: (a) 1.4%/s; (b) 0.7%/s; and (c) 0.35%/s.

are the volume and surface of a specimen. The proportional factor  $n$  is introduced to reflect the proportion of the work converting into heat.

Based on the abovementioned constitutive description, a thermo-elasto-visco-plastic model was established at finite deformation to reasonably predict the rate-dependent stress-strain responses and temperature variations, including the temperature drop due to the thermo-elastic effect and the temperature rise due to the visco-plastic dissipation, as shown in **Figures 13** and **14**.

#### 4. Conclusions and remarks

Recent advances in experiments and models of TMPs are reviewed, the main conclusions are below:

1. The TSMPs exhibit rate-dependent and temperature-dependent mechanical responses, a strong interaction between the internal heat generation and mechanical deformation is observed and strain and temperature distributions are nonuniform in tension. The internal heat generation is contributed by the decreased temperature due to the thermo-elastic effect and the increased temperature due to the visco-plastic dissipation.
2. The SME of TSMPs in the conditions of the stress-free recovery and strain-constraint recovery can be characterized by the shape recovery ratio, which decreases with the increases of peak strain, holding time after deformation, heating rate and decrease with the decreases of loading rate and finish recovery temperature.
3. The shape memory degeneration of TSMPs occurs under cyclic thermo-mechanical loadings and can be reflected by the strain recovery ratio, which gradually decreases with the increase of number of cycles and also depends on the peak strain, deformable temperature, recovery temperature and previous mechanical training.
4. Two types of models have been established, including the shape memory model which describing the SME and the thermo-mechanically coupled model which describing the interaction between the mechanical deformation, internal heat generation and heat exchange.
5. As mentioned earlier, most experiments and models of TSMPs are limited within uniaxial loading and the SME is performed by heating to a certain temperature. The experimental observations on the proportional and nonproportional multiaxial mechanical responses and the SME subjected to shape memory cycles are insufficient, the multiaxial thermo-mechanically coupled model is necessary to be constructed for predicting the SME more accurate. Moreover, the experimental and theoretical investigations on the deformation mechanisms of the multiple SME and temperature memory effect are necessary to be addressed in future.

#### Acknowledgements

Financial supports by National Natural Science Foundation of China (11572265; 11532010) and Excellent Youth Found of Sichuan Province (2017JQ0019) are acknowledged.

## Author details

Qianhua Kan<sup>1\*</sup>, Jian Li<sup>2</sup>, Guozheng Kang<sup>1</sup> and Zebin Zhang<sup>2</sup>

\*Address all correspondence to: qianhuakan@foxmail.com

1 State Key Laboratory of Traction Power, Southwest Jiaotong University, Chengdu, P. R. China

2 School of Mechanics and Engineering, Southwest Jiaotong University, Chengdu, P. R. China

## References

- [1] Lendlein A, Kelch S. Shape-memory polymers. *Angewandte Chemie International Edition*. 2002;**41**(12):2034-2057. DOI: 10.1007/978-3-642-12359-7
- [2] Hager MD, Bode S, Weber C, et al. Shape memory polymers: Past, present and future developments. *Progress in Polymer Science*. 2015;**49-50**:3-33. DOI: 10.1016/j.progpolymsci.2015.04.002
- [3] Behl M, Lendlein A. Shape-memory polymers. *Materials Today*. 2007;**10**(4):20-28. DOI: 10.1016/S1369-7021(07)70047-0
- [4] Leng JS, Lan X, Liu Y, et al. Shape-memory polymers and their composites: Stimulus methods and applications. *Progress in Materials Science*. 2011;**56**(7):1077-1135. DOI: 10.1016/j.pmatsci.2011.03.001
- [5] Hu J, Zhu Y, Huang H, et al. Recent advances in shape-memory polymers: Structure, mechanism, functionality, modeling and applications. *Progress in Polymer Science*. 2012;**37**(12):1720-1763. DOI: 10.1016/j.progpolymsci.2012.06.001
- [6] Nguyen TD. Modeling shape-memory behaviour of polymers. *Polymer Reviews*. 2013;**53**(1):130-152. DOI: 10.1080/15583724.2012.751922
- [7] Li G, Xu W. Thermomechanical behaviour of thermoset shape memory polymer programmed by cold-compression: Testing and constitutive modeling. *Journal of the Mechanics & Physics of Solids*. 2011;**59**(6):1231-1250. DOI: 10.1016/j.jmps.2011.03.001
- [8] Pieczyska EA, Maj M, Kowalczykgajewska K, et al. Thermomechanical properties of polyurethane shape memory polymer-experiment and modelling. *Smart Materials & Structures*. 2015;**24**(4):045043. DOI: 10.1088/0964-1726/24/4/045043
- [9] Zhang ZX, He ZZ, Yang JH, et al. Crystallization controlled shape memory behaviors of dynamically vulcanized poly (l-lactide) /poly (ethylene vinyl acetate) blends. *Polymer Testing*. 2016;**51**:82-92. DOI: 10.1016/j.polymertesting.2016.03.003
- [10] Kim BK, Sang YL, Mao X. Polyurethane having shape memory effect. *Polymer*. 1996;**37**(26):5781-5793. DOI: 10.1016/S0032-3861(96)00442-9

- [11] Tobushi H, Hara H, Yamada E, et al. Thermomechanical properties in a thin film of shape memory polymer of polyurethane series. *Smart Materials & Structures*. 1996;**2716**(4):483. DOI: 10.1117/12.232168
- [12] Atli B, Gandhi F. Thermomechanical characterization of shape memory polymers. *Journal of Intelligent Material Systems & Structures*. 2009;**17**(20):7002-7011. DOI: 10.1117/12.715248
- [13] Cui J, Kratz K, Lendlein A. Adjusting shape-memory properties of amorphous polyether urethanes and radio-opaque composites thereof by variation of physical parameters during programming. *Smart Materials & Structures*. 2010;**19**(6):065019. DOI: 10.1088/0964-1726/19/6/065019
- [14] Hu JL, Ji FL, Wong YW. Dependency of the shape memory properties of a polyurethane upon thermomechanical cyclic conditions. *Polymer International*. 2005;**54**(3):600-605. DOI: 10.1002/pi.1745
- [15] Volk B L, Lagoudas D C, Chen Y C, et al. Analysis of the finite deformation response of shape memory polymers: I. Thermomechanical characterization. *Smart Material Structures*. 2010;**19**(7):75005-75014(10). DOI: 10.1088/0964-1726/19/7/075005
- [16] Zhang C, Gou X, Xiao R. Controllable shape-memory recovery regions in polymers through mechanical programming. *Journal of Applied Polymer Science*. 2017;**135**(8). DOI: 10.1002/app.45909
- [17] McClung AJW, Tandon GP, Baur JW. Deformation rate-, hold time-, and cycle-dependent shape-memory performance of Veriflex-E resin. *Mechanics of Time-Dependent Materials*. 2013;**17**(1):39-52. DOI: 10.1007/s11043-011-9157-6
- [18] Azra C, Plummer CJG, Manson JAE. Isothermal recovery rates in shape memory polyurethanes. *Smart Materials & Structures*. 2011;**20**(8):082002. DOI: 10.1088/0964-1726/20/8/082002
- [19] Pieczyska EA, Staszczak M, Maj M, et al. Investigation of thermomechanical couplings, strain localization and shape memory properties in a shape memory polymer subjected to loading at various strain rates. *Smart Materials & Structures*. 2016;**25**(8):085002. DOI: 10.1088/0964-1726/25/8/085002
- [20] Pieczyska EA, Staszczak M, Kowalczyk-Gajewska K, et al. Experimental and numerical investigation of yielding phenomena in a shape memory polymer subjected to cyclic tension at various strain rates. *Polymer Testing*. 2017;**60**:333-342. DOI: 10.1016/j.polymertesting.2017.04.014
- [21] Tobushi H, Hashimoto T, Hayashi S, et al. Thermomechanical constitutive modeling in shape memory polymer of polyurethane series. *Journal of Intelligent Material Systems and Structures*. 1997;**8**(8):711-718. DOI: 10.1177/1045389X9700800808
- [22] Schmidt C, Neuking K, Eggeler G. Functional fatigue of shape memory polymers. *Advanced Engineering Materials*. 2010;**10**(10):922-927. DOI: 10.1002/adem.200800213

- [23] Schmidt C, Chowdhury AMS, Neuking K, et al. Studies on the cycling, processing and programming of an industrially applicable shape memory polymer Tecoflex(R) (or TFX EG 72D). *Journal of the Royal Society of Medicine*. 2011;**80**(9):544-546. DOI: 10.1177/0954008311405245
- [24] Mogharebi S, Kazakeviciute-Makovska R, Steeb H, et al. On the cyclic material stability of shape memory polymer. *Materialwissenschaft Und Werkstofftechnik*. 2013;**44**(6):521-526. DOI: 10.1002/mawe.201300023
- [25] Zhang Z, Li J, Chen K, et al. Experimental observation on the thermo-mechanically cyclic deformation behaviour of shape memory polyurethane. *Gongneng Cailiao/journal of Functional Materials*. 2017;**48**(5):05174-05179. DOI: 10.3969/j.issn.1001-9731.2017.05.032
- [26] Wornyo E, Gall K, Yang F, et al. Nanoindentation of shape memory polymer networks. *Polymer*. 2007;**48**(11):3213-3225. DOI: 10.1016/j.polymer.2007.03.029
- [27] Khan F, Koo JH, Monk D, et al. Characterization of shear deformation and strain recovery behaviour in shape memory polymers. *Polymer Testing*. 2008;**27**(4):498-503. DOI: 10.1016/j.polymertesting.2008.02.006
- [28] Diani J, Frédy C, Gilormini P, et al. A torsion test for the study of the large deformation recovery of shape memory polymers. *Polymer Testing*. 2011;**30**(3):335-341. DOI: 10.1016/j.polymertesting.2011.01.008
- [29] Du H, Liu L, Zhang F, et al. Thermal-mechanical behaviour of styrene-based shape memory polymer tubes. *Polymer Testing*. 2017;**57**:119-125. DOI: 10.1016/j.polymertesting.2016.11.011
- [30] Tobushi H, Okumura K, Hayashi S, et al. Thermomechanical constitutive model of shape memory polymer. *Mechanics of Materials*. 2001;**33**(10):545-554. DOI: 10.1016/S0167-6636(01)00075-8
- [31] Li J, Dong SY, Kan QH, et al. A Thermo-mechanical constitutive model of glassy shape memory polymers. *Applied Mechanics & Materials*. 2016;**853**:96-100. DOI: 10.4028/www.scientific.net/AMM.853.96
- [32] Diani J, Liu Y, Gall K. Finite strain 3D thermoviscoelastic constitutive model for shape memory polymers. *Polymer Engineering & Science*. 2006;**46**(4):486-492. DOI: 10.1002/pen.20497
- [33] Nguyen TD, Qi HJ, Castro F, et al. A thermoviscoelastic model for amorphous shape memory polymers: Incorporating structural and stress relaxation. *Journal of the Mechanics and Physics of Solids*. 2008;**56**(9):2792-2814. DOI: 10.1016/j.jmps.2008.04.007
- [34] Chen X, Nguyen TD. Influence of thermoviscoelastic properties and loading conditions on the recovery performance of shape memory polymers. *Mechanics of Materials*. 2011;**43**(3):127-138. DOI: 10.1016/j.mechmat.2011.01.001
- [35] Chen J, Liu L, Liu Y, et al. Thermoviscoelastic shape memory behaviour for epoxy-shape memory polymer. *Smart Materials and Structures*. 2014;**23**(5):055025. DOI: 10.1088/0964-1726/23/5/055025

- [36] Westbrook KK, Kao PH, Castro F, et al. A 3D finite deformation constitutive model for amorphous shape memory polymers: A multi-branch modeling approach for non-equilibrium relaxation processes. *Mechanics of Materials*. 2011;**43**(12):853-869. DOI: 10.1016/j.mechmat.2011.09.004
- [37] Yu K, McClung AJW, Tandon GP, et al. A thermomechanical constitutive model for an epoxy based shape memory polymer and its parameter identifications. *Mechanics of Time-Dependent Materials*. 2014;**18**(2):453-474. DOI: 10.1007/s11043-014-9237-5
- [38] Li Y, He Y, Liu Z. A viscoelastic constitutive model for shape memory polymers based on multiplicative decompositions of the deformation gradient. *International Journal of Plasticity*. 2017;**91**:300-317. DOI: 10.1016/j.ijplas.2017.04.004
- [39] Xiao R, Guo J, Nguyen TD. Modeling the multiple shape memory effect and temperature memory effect in amorphous polymers. *RSC Advances*. 2014;**5**(1):416-423. DOI: 10.1039/c4ra11412d
- [40] Zhou B, Liu Y, Leng J. Finite element analysis on thermo-mechanical behaviour of styrene-based shape memory polymers. *Acta Polymerica Sinica*. 2009;**009**(6):525-529. DOI: 10.3321/j.issn:1000-3304.2009.06.005
- [41] Shi G, Yang Q, He X, et al. A three-dimensional constitutive equation and finite element method implementation for shape memory polymers. *Computer Modeling in Engineering & Sciences*. 2013;**90**(5):339-358. DOI: 10.3970/cmescs.2013.090.339
- [42] Shi GH, Yang QS, He XQ. Analysis of intelligent hinged shell structures: Deployable deformation and shape memory effect. *Smart Materials & Structures*. 2013;**22**(12):126-132. DOI: 10.1088/0964-1726/22/12/125018
- [43] Liu YF, Wu JL, Zhang JX, et al. Feasible evaluation of the Thermo-mechanical properties of shape memory polyurethane for orthodontic Archwire. *Journal of Medical & Biological Engineering*. 2017;**37**(5):666-674. DOI: 10.1007/s40846-017-0263-z
- [44] Liu Y, Gall K, Dunn ML, et al. Thermomechanics of shape memory polymers: Uniaxial experiments and constitutive modeling. *International Journal of Plasticity*. 2006;**22**(2):279-313. DOI: 10.1016/j.ijplas.2005.03.004
- [45] Chen YC, Lagoudas DCA. Constitutive theory for shape memory polymers. Part I: Large deformations. *Journal of the Mechanics & Physics of Solids*. 2008;**56**:1752-1765. DOI: 10.1016/j.jmps.2007.12.005
- [46] Chen YC, Lagoudas DC. A constitutive theory for shape memory polymers. Part II : A linearized model for small deformations. *Journal of the Mechanics and Physics of Solids*. 2008;**56**(5):1766-1778. DOI: 10.1016/j.jmps.2007.12.004
- [47] Qi HJ, Nguyen TD, Castro F, et al. Finite deformation thermo-mechanical behaviour of thermally induced shape memory polymers. *Journal of the Mechanics & Physics of Solids*. 2008;**56**(5):1730-1751. DOI: 10.1016/j.jmps.2007.12.002

- [48] Boatti E, Scalet G, Auricchio F. A three-dimensional finite-strain phenomenological model for shape-memory polymers: Formulation, numerical simulations, and comparison with experimental data. *International Journal of Plasticity*. 2016;**83**:153-177. DOI: 10.1016/j.ijplas.2016.04.008
- [49] Li J, Kan Qnnnnn Kang G, et al. Thermo-mechanically coupled thermo-elasto-visco-plastic modeling of thermo-induced shape memory polyurethane at finite deformation. *Acta Mechanica Solida Sinica*. 2018;**31**(2):141-160. DOI: 10.1007/s10338-018-0022-x

---

# Shape Memory Hydrogels Based on Noncovalent Interactions

---

Leire Ruiz-Rubio, Leyre Pérez-Álvarez,  
Beñat Artetxe, Juan M. Gutiérrez-Zorrilla and  
José Luis Vilas

Additional information is available at the end of the chapter

<http://dx.doi.org/10.5772/intechopen.78013>

---

## Abstract

Shape memory polymers (SMPs) are polymeric materials that are capable of fixing temporary shape and recovering the permanent shape in response to external stimuli. In particular, supramolecular interactions and dynamic covalent bond have recently been introduced as temporary switches to construct supramolecular shape memory hydrogels (SSMHs), arising as promising materials since they can exhibit excellent cycled shape memory behavior at room temperature. On the other hand, hydrogels, conventionally, are flexible but sometimes extremely soft, and they can be easily damaged under external force, which could limit their long-time application. Therefore, self-healing hydrogels that can be rapidly auto-repaired when the damage occurs have been recently developed to solve this problem. These materials present more than one triggering stimulus that can be used to induce the shape memory and self-healing effect. These driven forces can be originated from hydrogen bonds, hydrophobic interactions, and reversible covalent bonds, among others. Beyond all these, hybrid organic-inorganic interactions represent an interesting possibility due to their versatility and favorable properties that allow the fabrication of multiresponsive hydrogels. In this chapter, shape memory hydrogels based on noncovalent interactions are described.

**Keywords:** shape memory, hydrogels, supramolecular interactions, self-healing, smart materials

---

## 1. Introduction

Hydrogels are three-dimensional soft networks formed by physical and/or chemical cross-linking of hydrophilic polymers, which are able to swell absorbing and retaining a substantial

---

amount of water [1]. Hydrogels have been intensively studied due to their relevant properties, such as their similarity to body tissues, low surface friction, ability to encapsulate and release (molecules, ions, cells), appropriate morphology for cell proliferation and stimuli-responsive properties. This stimuli-responsiveness allows hydrogels to be programmed to vary spatially and/or temporally their properties as response against external changes. Different external triggers have been deeply studied along the last years to induce reversible hydrogel-solution or swollen-collapsed transitions, such as pH, temperature, radiation, redox reactions, or chemical triggers [2]. As a consequence of these switchable properties, these materials can behave as actuators or sensors, and therefore, they have been intensively investigated in the last decades in a great variety of fields, among which it is worth to highlight, biomedicine, agriculture and wastewater treatment [3]. Currently, hydrogels are being actively commercialized in all those application fields. However, hydrogels generally show poor mechanical properties, and consequently, mechanical damages and cracks limit their correct function over a long period of time, which is especially problematic for biomedical applications. For this reason, nowadays mechanically more stable materials, such as ceramics or metals, are preferred in this area. Thus, an interesting approach to exploit the full potential of hydrogels would be to promote their self-healing and shape memory properties, which are well known for conventional materials or even polymers but nowadays continues being a challenging issue for hydrogels [4].

Self-healing is one of the most fascinating functions encountered in nature, and it represents the ability of a material to regenerate and repair itself after damage. This property is based on reversible chemical or physical interactions that quickly and efficiently are reformed within the structure of the hydrogels, and they would allow to increasing the working lifespan and application frame of hydrogels [5]. A closely related but different property is that so-called shape memory effect (SME), which represents the nonisotropic response of the hydrogel network against changes in the medium. These materials constitute the growing family of shape memory hydrogels (SMH). This means that the polymeric network is able to switch spatially their shape without major volume alteration. This more complex effect requires more sophisticated structural and chemical approaches than self-healing. The SME implies an elastic deformation (programming) of the hydrogels that are temporarily fixed by means of reversible chemical or physical crosslinking. This temporary shape can reverse to the original shape when these molecular switches are turned off (**Figure 1**). So, shape memory effect lets to recover from the programmed temporary shape when the material is exposed to a given external stimulus; [6] typically temperature, but also light, magnetic or electric field response has been successfully developed [7]. Shape memory polymers (SMP) based on pure polymers, blends and composites have been intensively studied for actuators, sensors, microfluidic systems in aerospace technology, vascular grafts and cardiovascular stents in biomedicine, for textile industry applications and consumer care products [8]. However, SME on hydrophilic soft networks entails some additional difficulties that make impossible the direct transfer from the well-known molecular architecture of hydrophobic SMPs because temporary shape fixation requires crosslinks able to remain stable in an aqueous environment. For example, this fixation may not be carried out by crystalline domains from the hydrophilic polymer acting as main

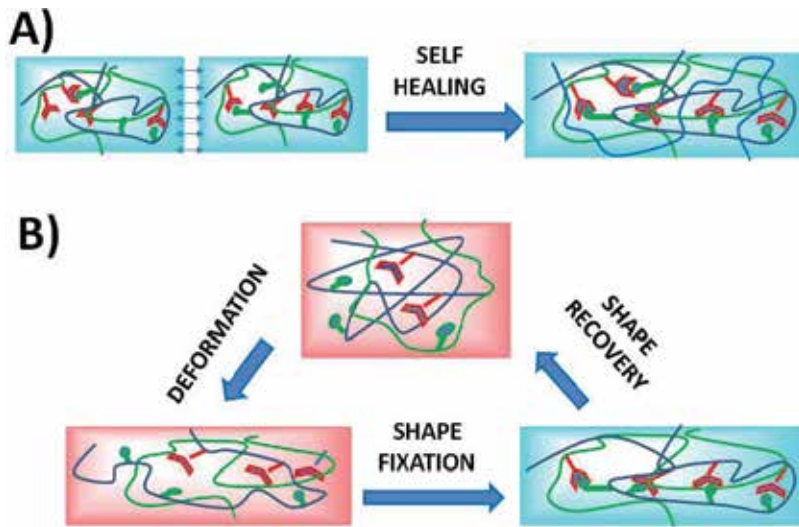


**Figure 1.** Schematic representation of (A) self-healing and (B) shape memory effects for hydrogels.

chain (which is one of the most used strategies for hydrophobic SMPs) because they may dissolve. Thus, more elaborated approaches have been developed, such as hydrogels in which hydrophobic crystallizable side chains have been grafted to hydrophilic polymer networks to act as temperature-sensitive temporary crosslinking [9]. However, due to the easy permeation by small molecules and light permeability of hydrogels on their swollen state, in contrast to hydrophobic shape memory polymers, stimuli different to temperature, such as light, [10] pH, [11] or ions [12] can be easily used. When molecular switches reply to more than one stimulus, multishape memory effect can be addressed inducing multiple actions on the hydrogels [13].

Therefore, self-healing and shape-memory are both originated from the same switchable interactions. In addition to the classical approach that involves the use of crystallizable side chains, these temporary linkers could be dynamic covalent bonds or supramolecular interactions, such as hydrogen bonding, host-guest recognition, or metal-ligand coordination. This chapter reviews the last advances in the strategies in which supramolecular interactions have been used to fix the temporary shape in the quest for obtaining SMH. The interactions can be properly employed in the efficient design of hydrogels for advanced applications and new functionalities that would display high impact in fields like biomedicine. In this sense, sensors for diagnosis, drug delivery systems for controlled and minimal invasive implantation, self-tightening degradable sutures, devices for easy in vitro growth and manipulation of cells, or materials for 3D printing of biomedical devices and soft tissue engineering, among others, are expected to be soon improved by the development of self-healing and shape memory hydrogels. Response time is a key factor in the design of new and effective self-healing and shape memory hydrogels. On the one hand, hydrogels with slow SME may be promising materials for medical implants, in order to

avoid post-implantation shocks originated by the sudden alterations. On the other hand, fast SME are of great importance for the development of sensors and actuators, such as robotic devices and artificial muscles. Recently, multiple supramolecular SMH combined with self-healing properties have been reported as an evidence of the promising future of this research field [14]. The obtaining of multiple programmed shapes triggered by diverse properties and tailored SME response speed are currently the main challenges in the development of SMH technology that would open opportunities for a wider range of potential applications and value-added properties.

## 2. Mechanism

Shape memory mechanism in polymers is based on a dual segment material. On the one hand, an elastic polymer network with netpoints is required to define the permanent shape. These netpoints usually are chemical cross-linkings or physical netpoints such as crystalline domains or complexes. In addition, a programming process consisting of the elastic deformation of the sample takes place and additional molecular switches provide temporary cross-links to reversibly fix the temporary shape of the material. As a result of the application of an external stimulus, usually temperature, molecular switches are disturbed and the polymer chains acquire their initial mobility that leads to a macroscopic movement resulting in the initial shape [15]. In case of thermoresponsive SME polymeric segments with specific thermal transitions like glass transition, melting, or liquid-crystalline phase transition, these transitions can act as molecular switches when temperature is varied.

In order to extend the potential of SMPs as biomaterials, crucial requirements such as biocompatibility, mechanical properties, and biodegradability have promoted the development of the hydrogels with SME. Similar to thermally induced SMPs, supramolecular shape memory hydrogels present cross-linkings that define the network, this is the permanent shape, and stimuli responsive switches, consisting of reversible interactions to fix the temporary shape (**Figure 1**). Thus, shape fixation and recovery demand interactions easy to be broken and formed, while adequate mechanical properties of the material are closely related to the concentration and strength of all the possible kinds of cross-linkings.

The temporary shape can be created by folding, elongation, or compression. The high water uptake in hydrogels gives rise to shape memory materials able of undergoing large deformation between the temporary and permanent states.

Molecular switches, in the case of hydrogels, usually are not part of the main chain forming the polymer network. Typically, are pending moieties such as short crystallizable side chains, [16] specific groups for host-guest interactions, [17] complex-forming groups [18] or groups able to form dynamic bonds [19]. Similar to self-healing process, polymeric segments reorganize and water flows through the polymer network via diffusion, and the kinetics of these process in different states of deformation of the network will govern the global rate of the SME.

The simplest SME is also referred as dual shape memory effect and corresponds to the case in which only one reversible interaction and thus one temporary shape is fixed in each shape memory cycle. Accordingly, triple shape memory effect corresponds to two reversible and independent interactions occurring in the same hydrogel network. Currently, despite the huge investigation effort made in the last years, still there is a reduced bibliography about triple and multishape memory hydrogels.

Although noncovalent interactions are weaker than covalent interactions, their importance in polymer science has been shown; in this context, supramolecular shape memory hydrogels based on noncovalent interactions present an arisen importance. The incorporation of noncovalent interactions into hydrogel network could modify the properties of the formed hydrogel. These variations increased the possible applications not only for shape memory effect or a closely related self-healable ability, but also for the development of high tough hydrogels. In **Figure 2**, the most common interactions used in shape memory hydrogels are described such as hydrogen bonds, metal-ligand interactions, and ion-ion interactions.

## 2.1. Hydrogen bonding

Hydrogen bond is an electrostatic attraction between donors and acceptors when a hydrogen atom is covalently bound to a highly electronegative atom. These interactions are considered as a key interaction in supramolecular chemistry due to their highly directionality and their relative high strength. In addition, their ability to form dynamic interactions, with a continuous formation/disruption of the bonds by external stimuli, has increased their use as a driving force in shape memory hydrogels.

The addition of moieties capable to form hydrogen bonds dimers in the hydrogel structure has been successfully used to improve the shape memory effect. For example, ureidopyrimidinone (UPy) presents strong self-complementary dimers by a quadruple hydrogen-bonding, [20] and

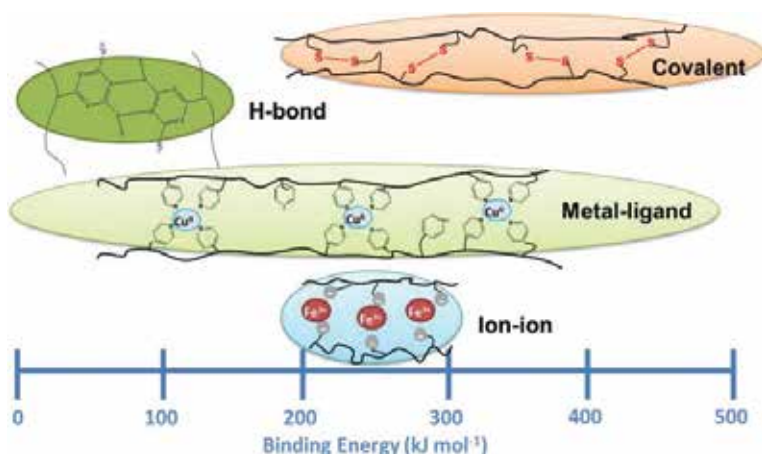


**Figure 2.** Reversible interactions for shape memory hydrogels construction.

this strong and unidirectional dimerization could induce the shape recovery effect in the hydrogels. These moieties could be added to the hydrogel by a direct substitution on the main chain of the hydrogel, for example poly(vinylalcohol) (PVA) chain [21] or by modifying one of the monomers such as in a triblock copolymer of poly(*N*-isopropylacrylamide-*b*-ethylene oxide-*N*-isopropylacrylamide) with UPy motifs on some of *N*-isopropylacrylamide monomers and polymerize by reversible addition-fragmentation chain-transfer (RAFT) [22]. Similarly, some authors have used the strong H-bond dimer of diaminotriazine (DAT) present in 2-vinyl-4,6-diamino-1,3,5-triazine groups to construct SMHs that present strong hydrogen bond dimer (**Figure 3**). Liu et al. have copolymerized DAT units with *N,N*-dimethylacrylamide and PEG diacrylate. These hydrogels possessed robust mechanical properties because of the strong double hydrogen bonds (DAT-DAT hydrogen bonds) that could be broken by the protonation of the two amino groups of DAT, being the shape memory of this hydrogels triggered by pH changes in the medium [23].

A slightly different approach has been described by Chen et al. [24] in which tannic acid (TA), a polyphenol derived from plants which easily forms H-bonds, develops strong multiple hydrogen bonds with poly(vinyl alcohol) (PVA), and they coagulate when they are physically mixed around 60°C and easily obtained hydrogel at room temperature. The strong hydrogen bonds between PVA and TA fix the permanent crosslink, whereas the H-bonds formed between poly(vinyl alcohol) chains, weaker than the PVA-TA H-bonds, are the temporary crosslinks.

Often the described hydrogen bond interactions not only provide a shape memory effect in the hydrogels but also give a self-healing capability to the formed networks.

## 2.2. Self-assembly processes in biomimetic systems

The self-assembly process of biomacromolecules can be considered as a specific way to get the hydrogen bonding-based shape memory performance. Formation of triple-helix structures is

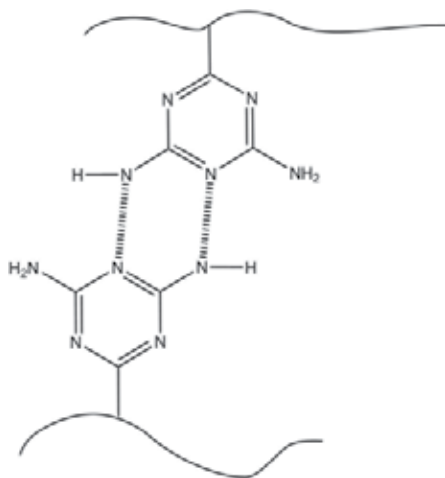


**Figure 3.** Hydrogen bond dimer associated to diaminotriazine.

in the origin of (1) thermally triggered shape memory behavior of collagen-containing hydrogels [25] and (2) near-infrared light induced rapid shape recovery in a (gelatin/graphene oxide)-based hybrid system, among others [26]. This concept has been extensively studied by Willner and collaborators for the fabrication of DNA-acrylamide SMHs. A pH-responsive material containing polymeric chains with self-complementary DNA strands fixed its temporary triangular shape *via* self-assembly at pH = 5, whereas it transformed back to the original quasi-liquid state when pH was increased to 8 [27]. This rational approach was later extended to more complicated systems exhibiting more than one pair of self-complementary DNA strands and exhibiting two pH-dependent temporary states, [28, 29] and as much as three different triggering stimuli [30].

### 2.3. Host-guest interactions

Host-guest interactions are in the basis of another interesting method to construct SMHs. The supramolecular interactions established between molecular hosts with large cavities and complementary guests that usually exhibit molecular recognition are able to induce a temporary crosslink. Hydrogels can be synthesized by (1) mixing polymers bearing host entities with those containing guest species or (2) copolymerizing monomers functionalized host and guest units. Although different macrocyclic hosts such as cucurbit[n]urils, crown ethers and cyclodextrins have been used to fabricate self-healing hydrogels based on host-guest interactions according to a recent review [31], only the latter have been exploited to date for the preparation of SSMHs.

Cyclodextrins (CD) are a family of cyclic oligosaccharides which have been traditionally used in supramolecular chemistry due to their capability to generate host-guest complexes. Typical cyclodextrins contain six ( $\alpha$ -CDs), seven ( $\beta$ -CDs), or eight ( $\gamma$ -CDs) glucose units disposed in a ring, and thus, the size of the inner cavity varies accordingly. CDs have been widely used as drug-delivery systems in pharmaceutical applications because they can form inclusion compounds with hydrophobic drugs and become them water-soluble [32]. Analogously, their shape and chemical properties make CDs ideal candidates for the preparation of rotaxanes [33]. Inspired by rotaxane-like systems, Yang's group reported a poly(pseudorotaxane) supramolecular SMH *via* copolymerization of host ( $\alpha$ -CD) and guest (PEG) monomers [34]. The use of acrylamide and acrylate comonomers avoided the rapid precipitation of  $\alpha$ -CD/PEG inclusion complexes in the photoinitiated copolymerization process and afforded a mechanically tough physical hydrogel. Following a different synthetic approach, a mixture of poly- $\beta$ -cyclodextrin and a polymer with adamantane groups in the side chains affords a physical hydrogel with a high self-healing efficiency [35]. Shape memory properties were added in both systems after being treated with  $\text{FeCl}_3$  aqueous solution. The mechanism of the temporary crosslinking arisen from the coordination between carboxylate groups and  $\text{Fe}^{3+}$  ions and the methods for recovering the original shape are those that will be discussed more specifically in the next section.

With regard to hydrogels that display shape memory behavior induced by host-guest interactions, Li, Zhang and collaborators reported a pH sensitive SMH cross-linking  $\beta$ -CD-modified alginate and diethylenetriamine-modified alginate with  $\text{Ca}^{2+}$  ions [36]. At high pH values

(11.5), the material can be easily deformed to its temporary phase because the protonation of amino groups from diethylenetriamine prevents the formation of the inclusion complex. Deprotonation at neutral pH allows the system to recover its initial shape. Encouraged by the high recovery ratio (> 95%), the biocompatibility of the polymeric backbone and the physiological pH in which the shape memory process takes place, and the SMH was evaluated as a promising candidate for biomedical applications. The chemical approach was later extended by the same research group to prepare redox-active SMHs. In this case, ferrocene-modified branched polyethylenimine (PEI) was used in combination with  $\beta$ -CD-modified chitosan. The reduced form of the ferrocene ( $\text{Fe}^{2+}$ ) interacts with  $\beta$ -CD and permits the processing of this material into temporary shapes, whereas its oxidation leads to the shape recovery because the positively charged form is excluded from the CD cavity (**Figure 4**) [37].

Moving a step forward, the use of two different kinds of inclusion complexes acting simultaneously resulted in a SSMH with excellent self-healing and expansion-contraction properties [17]. Both ferrocene and adamantane guests and  $\beta$ -CD hosts were attached in polyacrylamide-based main chains to generate a dual temporary crosslinks. Oxidation of ferrocene groups leads to not only the shape memory behavior, but also to the expansion of the hydrogel. It is worth noting that different temporary shapes can be fixed through mechanical stress applied on the oxidized form taking advantage of the lability of  $\beta$ -CD/adamantine interactions.

## 2.4. Metal-ligand coordination bonds

This approach is based on the interactions established between the functional oxygen- or nitrogen-donor groups of the polymeric chains that act as ligands toward the transition metal ions that have been incorporated into the system. Coordination bonds are able to fix the temporary shape, whereas their removal by external chelating agent, the action of a reducing species and light- or electrically driven reactions leads back to the original state of the hydrogel. The addition of colorful, redox-, magnetically- and catalytically active transition metal cations can also confer the polymeric material with additional functionalities. It is worth noting that the temporary interactions could often show strong contributions from the electrostatic forces

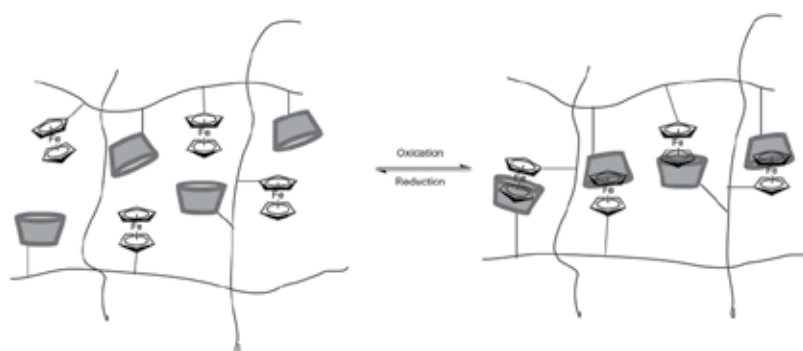


**Figure 4.** Schematic representation of the SME in redox-sensitive hydrogels based on host-guest interactions between ferrocene and CD groups.

between positively charged metal cations and negatively charged groups like phosphates or carboxylates. Examples including systems in which the electrostatic interactions have been identified as the origin of the shape memory behavior will be covered in the next section.

Metal-ligand coordination bonds have been applied in a variety of systems that cover from hard Lewis-bases like O-donor ligands in combination with hard Lewis-acids ( $\text{Fe}^{3+}$ ) to N-donor ligands that interact with softer acids ( $\text{Cu}^{2+}$ ,  $\text{Zn}^{2+}$ ). The former strategy has been applied in cross-linked polyacrylamide/polyacrylic acid gels [38–40]. For instance, randomly distributed and physically cross-linked copolymer hydrogels showed high toughness and excellent processability in such a way that they could be fabricated by three-dimensional printing technologies. The metal coordination bonds could be easily removed through the light-induced reduction of the  $\text{Fe}^{3+}$  in the presence of citric acid or protonation of carboxylate groups under acidic pH. Conversely, chemical crosslink afforded a controllable self-deforming SMH: the original shape can be gradually modified as a function of the pH, whereas the transition-metal triggered shape memory behavior starts when the temporary form at basic pH is fixed by its immersion in an aqueous solution containing  $\text{Fe}^{3+}$  ions. Shape recovery takes place in a controllable way by sequential steps that imply the increase of  $\text{H}^+$  concentration in the aqueous media.

When it comes to N-donor ligands pyridine, imidazole and cyanide groups have been employed with redox active  $\text{Cu}^{2+}$  and nonactive  $\text{Zn}^{2+}$  ions to lock the temporary shape. For redox sensitive  $\text{Cu}^{2+}$ -pyridine bonds (**Figure 5**), the reduction to  $\text{Cu}^+$  *via* sodium metabisulphite was used as the external stimulus required to recover the original shape through a process that involved not only the cited shape memory behavior, but also changes in the color and mechanical properties of the material [41]. On the contrary, the polyacrylate chains with

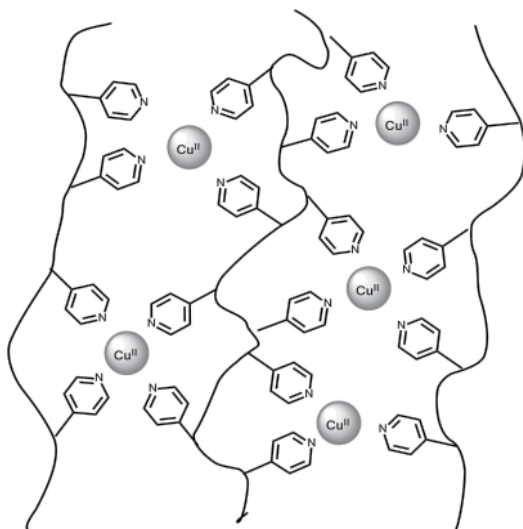


**Figure 5.** Schematic representation of the SME in redox-sensitive hydrogels based on metal-coordination bonds between copper cations and pyridine groups.

imidazole side groups generated a SMH based on  $Zn^{2+}$ /imidazole bonds whose shape can only be reversed by the addition of strong chelating agents such as EDTA [42]. In a closely related work, a UV-light triggered shape memory was described in a similar polymeric matrix. In this case, diphenyliodonium nitrate was incorporated which generates protons under UV light leading to the protonation of imidazole groups and consequent cleavage of coordination bonds [43]. Regarding cyanide containing materials, Liu et al. reported on dipole-dipole reinforced, acrylonitrile-based, ultra-high strength hydrogels that displays triple shape memory effect regulated by zinc ion concentration. Additional investigations by this group demonstrated that the temporary shape can be pre-programmed by surface micropatterning [12, 43].

## 2.5. Electrostatic interactions

Ionic temporary crosslink has been long used to induce self-healing behavior in covalently cross-linked hydrogels. Electrostatic forces between anionic functional groups and cationic metal cations can afford highly stretchable and tough self-healable hydrogels, as exemplified by photo-cross-linked polyacrylamide networks with  $Ca^{2+}$ -alginate interactions [44]. Following this approach and combining it with covalent boronate ester dynamic bonds, a dual shape memory/self-healing PVA hydrogel was developed where the incorporations/removal of  $Ca^{2+}$  ions was used to trigger the shape recovery process [45]. According to the authors, the temporary state can be fixed in 30 s, much faster than other shape memory hydrogels induced by metal ions, which need hours for that purpose. This is the case of acrylamide/isoprenyl phosphonic acid copolymers cross-linked by PEG diacrylate where the presence of  $Fe^{3+}$  ions allows the shape memory to take place [46]. In both systems, the extraction of metal ions with EDTA chelating agent completely recovers the original shape. Additionally, the reduction of  $Fe^{3+}$  with erythorbic acid for the later example and the removal of  $Ca^{2+}$  ions upon immersion of the hydrogel in basic aqueous media for the former can be applied as alternative recovering stimuli. Among the alginate-based shape-memory materials, it is worth highlighting the superelastic hydrogel that incorporates flexible  $SiO_2$  nanofibers and exhibits pressure-dependent conductivity. Trivalent  $Al^{3+}$  cations facilitate complete recovery from 80% strain in this ultrahigh water content hydrogel (99.8 wt%) [47].

The electrostatic approach can be applied in combination with not only dynamic covalent bonds, but also another additional temporary interactions such as hydrogen bonds as was demonstrated by  $Ca^{2+}$ -triggered shape memory properties in PVDT-PAA (VDT = 2-vinyl-4,6-diamino-1,3,5-triazine) hydrogels synthesized *via* photo-polymerization [48]. The low cytotoxicity of the system encouraged the authors to evaluate biological aspects. It was proved that cells could adhere to the hydrogel surface, and afterward, they can be conveniently detached by simply adding calcium ions without influencing their viability. Thus, this dual strategy paves the way for the design of new multifunctional high strength hydrogels for biomedical applications.

Besides the addition of metal cations, charged groups can also be coexisting in zwitterionic copolymers. Classic examples include those in which anionic carboxylate or sulfonate monomers and cationic ammonium units are copolymerized with neutral comonomers. These hydrogels can show the shape memory behavior in the absence of any chemical cross-linker or addition of metal salts. Tong [49] have opted for synthesizing polyampholyte hydrogels by reacting

cationic 3-(methacryloylamino)propyltrimethylammonium, anionic *p*-styrenesulfonate and neutral methacrylic acid monomers in a one-step process. Apart from the pH-dependent shape memory effect that can be repeated over 10 times, the hydrogel showed a spontaneous shape change after the first cycle. Therefore, the hydrogel prepared was proposed as a starting point for the design of new soft actuators that require successive actions. However, the preparation of the desired shape memory material in polyampholyte hydrogels is often challenging. As shown by previous works, different authors were forced to incorporate Fe<sup>3+</sup> ions or to induce salt-dependent hydrophobic association in order to fix the temporary shape [18].

Although the field of shape memory hydrogels based on electrostatic assembly is basically limited to simple metal-ion containing systems, recent advances in self-healing hydrogels that incorporate another inorganic entities provide new ideas that could be promisingly exploited with the aim of pursuing shape-memory behavior. Indeed temporary ionic bonds are in the origin of (1) the rapid self-healing ability of mechanically robust hybrid PAA hydrogels that contain amino-derivatized nanometric polyhedral oligomeric silsesquioxanes (POSS) [50]; (2) the magnetic auto-repairing ability of a chitosan-based hydrogel loaded with magnetite (Fe<sub>3</sub>O<sub>4</sub>) nanoparticles that display coatings modified with carboxylic acid functionalities [51]; and (3) the combination of anionic polyoxometalate (POM) [EuW<sub>10</sub>O<sub>36</sub>]<sup>9-</sup> oxo-clusters with cationic triblock copolymers bearing guanidinium groups that result in hybrid hydrogels with both tunable luminescent and self-healing capability [52].

### 3. Multishape memory effect

Triple-shape or multishape memory hydrogels can be designed by a combination of two or more noninterfering dynamic switches incorporated in hydrogel's network [53]. In spite of the great variety of supramolecular interactions described above, triple/multiple shape memory effect still represents a great challenge. This class of SSMH is capable to store two or more metastable shapes in addition to the original shape. In contrast to conventional shape memory polymers in which temporally switches are based on temperature changes, SSMHs can respond to different stimuli (pH, redox...) through sequential changes at room temperature [54]. This kind of hydrogels is until now less studied, and only few examples have been reported. Xiao et al. have demonstrated the triple-shape and multishape memory effect by using two reversible interactions based on dynamic covalent interactions and metal–ligand coordination bonds. The hydrogel was prepared by the polymerization of acrylamide monomer in the presence of chitosan and oxidized dextran. The temporary shape could be obtained by multiresponsive Schiff base-type bonds established between the amino groups of chitosan and the aldehyde groups of the oxidized dextran. In addition, other secondary temporary shape could be fixed with the chelating capability of the chitosan with several metal cations [53]. More complicated studies have been devoted to the hydrogels based on three switchers based on metal–ligand coordination, dynamic covalent bonds and coil–helix transaction. Each of these interactions could fix one temporary shape in the hydrogel. The first temporary shape was achieved by coordination of acrylic acid moieties to Fe<sup>3+</sup> cations. A second temporary shape was fixed by the reaction between phenylboronic acid (PBA) and 1,2-diols forming ester

bonds under basic pH (pH = 10). Finally, the third temporary shape was fixed by coil-helix transition of the agar structure that represents switch rarely used in the design of this kind of hydrogels [55]. A very similar approach was described by Le et al. where a triple-shape memory was based on PBA-diol bonds and the coordination interactions between alginate and calcium cations [56].

## 4. Conclusion

In summary, highly promising advances have been made in the development of supramolecular shape memory hydrogels, and a plethora of new hydrogels will be synthesized in the following years due to the versatility of the supramolecular interactions. In addition, the self-healable capability and their adequate biocompatible properties added great capability of adaptation to different requirements.

## Acknowledgements

This work has been funded by UPV/EHU (grant PG17/37, IT1082-16, IT718-13), MINECO (MAT2017-89553-P). B.A. thanks the Vice-rectorate for Research of UPV/EHU for a postdoctoral fellowship within the program "Convocatorias de Ayudas para la Especialización de Personal Investigador."

## Conflict of Interest

The authors declare no conflict of interest.

## Author details

Leire Ruiz-Rubio<sup>1,3\*</sup>, Leyre Pérez-Álvarez<sup>1,3</sup>, Beñat Artetxe<sup>2</sup>, Juan M. Gutiérrez-Zorrilla<sup>2,3</sup> and José Luis Vilas<sup>1,3</sup>

\*Address all correspondence to: leire.ruiz@ehu.eus

1 Macromolecular Chemistry Group (LABQUIMAC), Department of Physical Chemistry, Faculty of Science and Technology, University of the Basque Country UPV/EHU, Bilbao, Spain

2 Department of Inorganic Chemistry, Faculty of Science and Technology, University of the Basque Country UPV/EHU, Bilbao, Spain

3 BCMaterials, Basque Center for Materials, Applications and Nanostructures, UPV/EHU Science Park, Leioa, Spain

## References

- [1] Langer R, Peppas NA. Advances in biomaterials, drug delivery, and bionanotechnology. *AICHE Journal*. 2003;**49**:2990-3006. DOI: 10.1002/aic.690491202
- [2] Gupta P, Vermani K, Garg S. Hydrogels: From controlled release to pH-responsive drug delivery. *Drug Discovery Today*. 2002;**7**:569-579. DOI: 10.1016/S1359-6446(02)02255-9
- [3] Richter AA, Paschew G, Klatt S, Lienig J, Arndt KF, HJP A. Review on hydrogel-based pH sensors and microsensors. *Sensors*. 2008;**8**:561-581. DOI: 10.3390/s8010561
- [4] Gyarmati B, Szilágyi BA, Szilágyi A. Reversible interactions in self-healing and shape memory hydrogels. *European Polymer Journal*. 2017;**93**:642-669. DOI: 10.1016/j.eurpolymj.2017.05.020
- [5] Taylor DL. in het Panhuis M. Self-Healing Hydrogels. *Adv. Maternité*. 2016;**8**:9060-9093. DOI: 10.1002/adma.201601613
- [6] Löwenberg C, Balk M, Wischke C, Behl M, Lendlein A. Shape-memory hydrogels: Evolution of structural principles to enable shape switching of hydrophilic polymer networks. *Accounts of Chemical Research*. 2017;**50**:723-732. DOI: 10.1021/acs.accounts.6b00584
- [7] Zhao Q, Qi HJ, Xie T. Recent progress in shape memory polymer: New behavior, enabling materials, and mechanistic understanding. *Progress in Polymer Science*. 2015;**49-50**:79-120. DOI: 10.1016/j.progpolymsci.2015.04.001
- [8] Hu J, Zhu Y, Huang H, Lu J. Recent advances in shape-memory polymers: Structure, mechanism, functionality, modeling and applications. *Progress in Polymer Science*. 2012;**7**:1720-1763. DOI: 10.1016/j.progpolymsci.2012.06.001
- [9] Li G, Zhang H, Fortin D, Xia H, Zhao Y. Poly(vinyl alcohol)-poly(ethylene glycol) double-network hydrogel: A general approach to shape memory and self-healing functionalities. *Langmuir*. 2015;**31**:11709-11716. DOI: 10.1021/acs.langmuir.5b03474
- [10] Habault D, Zhang H, Zhao Y. Light-triggered self-healing and shape-memory polymers. *Chemical Society Reviews*. 2013;**2**:7244. DOI: 10.1039/c3cs35489j
- [11] Liu C, Qin H, Mather PT. Review of progress in shape-memory polymers. *Journal of Materials Chemistry*. 2007;**17**:1543. DOI: 10.1039/b615954k
- [12] Han Y, Bai T, Liu Y, Zhai X, Liu W. Zinc ion uniquely induced triple shape memory effect of dipole-dipole reinforced ultra-high strength hydrogels. *Macromolecular Rapid Communications*. 2012;**33**:225-231. DOI: 10.1002/marc.201100683
- [13] Xiao YY, Gong XL, Kang Y, Jiang ZC, Zhang S, Li BJ. Light-, pH- and thermal-responsive hydrogels with the triple-shape memory effect. *Chemical Communications*. 2016;**52**:10609-10612. DOI: 10.1039/C6CC03587F
- [14] Zhang H, Zhao Y. Polymers with dual light-triggered functions of shape memory and healing using gold nanoparticles. *ACS Applied Materials & Interfaces*. 2013;**5**:13069-13075. DOI: 10.1021/am404087q

- [15] Ratna D, Karger-Kocsis J. Recent advances in shape memory polymers and composites: A review. *Journal of Materials Science*. 2008;**43**:254-269. DOI: 10.1007/s10853-007-2176-7
- [16] Bilici C, Can V, Nöchel U, Behl M, Lendlein A, Okay O. Melt-processable shape-memory hydrogels with self-healing ability of high mechanical strength. *Macromolecules*. 2016;**49**:7442-7449. DOI: 10.1021/acs.macromol.6b01539
- [17] Miyamae K, Nakahata M, Takashima Y, Harada A. Self-healing, expansion-contraction, and shape-memory properties of a preorganized supramolecular hydrogel through host-guest interactions. *Angewandte Chemie International Edition*. 2015;**54**:8984-8987. DOI: 10.1002/anie.201502957
- [18] Fan Y, Zhou W, Yasin A, Li H, Yang H. Dual-responsive shape memory hydrogels with novel thermoplasticity based on a hydrophobically modified polyampholyte. *Soft Matter*. 2015;**11**:4218-4225. DOI: 10.1039/C5SM00168D
- [19] Li Z, Lu W, Ngai T, Le X, Zheng J, Zhao N, Huang Y, Wen X, Zhang J, Chen T. Mussel-inspired multifunctional supramolecular hydrogels with self-healing, shape memory and adhesive properties. *Polymer Chemistry*. 2016;**7**:5343-5346. DOI: 10.1039/C6PY01112H
- [20] Nieuwenhuizen MML, TFA DG, Der Bruggen RLJ V, Paulusse JMJ, Appel WPJ, Smulders MMJ, Sijbesma RP, Meijer EW. Self-assembly of ureido-pyrimidinone dimers into one-dimensional stacks by lateral hydrogen bonding. *Chemistry – A European Journal*. 2010;**16**:1601-1612. DOI: 10.1002/chem.200902107
- [21] Chen H, Li Y, Tao G, Wang L, Zhou S. Thermo- and water-induced shape memory poly(vinyl alcohol) supramolecular networks crosslinked by self-complementary quadruple hydrogen bonding. *Polymer Chemistry*. 2016;**7**:6637-6644. DOI: 10.1039/C6PY01302C
- [22] Zhang G, Chen Y, Deng Y, Ngai T, Wang C. Dynamic supramolecular hydrogels: Regulating Hydrogel properties through self-complementary quadruple hydrogen bonds and thermo-switch. *ACS Macro Letters*. 2017;**6**:641-646. DOI: 10.1021/acsmacrolett.7b00275
- [23] Xu B, Zhang Y, Liu W. Hydrogen-bonding toughened hydrogels and emerging CO<sub>2</sub>-responsive shape memory effect. *Macromolecular Rapid Communications*. 2015;**36**:1585-1591. DOI: 10.1002/marc.201500256
- [24] Chen YN, Peng L, Liu T, Wang Y, Shi S, Wang H. Poly(vinyl alcohol)-tannic acid hydrogels with excellent mechanical properties and shape memory behaviors. *ACS Applied Materials & Interfaces*. 2016;**8**:27199-27206. DOI: 10.1021/acsmi.6b08374
- [25] Skrzyszewska PJ, Jong LN, de Wolf FA, Cohen Stuart MA, van der Gucht J. Shape-memory effects in biopolymer networks with collagen-like transient nodes. *Biomacromolecules* 2011;**12**:2285-2292. DOI: 10.1021/bm2003626
- [26] Huang J, Zhao L, Wang T, Sun W, Tong Z. NIR-triggered rapid shape memory PAM-GO-gelatin hydrogels with high mechanical strength. *ACS Applied Materials & Interfaces*. 2016;**8**:12384-12392. DOI: 10.1021/acsmi.6b00867
- [27] Guo W, Lu CH, Orbach R, Wang F, Qi XJ, Ceconello A, Seliktar D, Willner I. pH-stimulated DNA hydrogels exhibiting shape-memory properties. *Advanced Materials*. 2015;**27**:73-78. DOI: 10.1002/adma.201403702

- [28] Hu Y, Lu CH, Guo W, Aleman-Garcia MA, Ren J, Willner I. A shape memory acrylamide/DNA hydrogel exhibiting switchable dual pH-responsiveness. *Advanced Functional Materials*. 2015;**25**:6867-6874. DOI: 10.1002/adfm.201503134
- [29] Hu Y, Guo W, Kahn JS, Aleman-Garcia MA, Willner I. A shape-memory DNA-based hydrogel exhibiting two internal memories. *Angewandte Chemie International Edition*. 2016;**55**:4210-4214. DOI: 10.1002/anie.201511201
- [30] Lu CH, Guo W, Hu Y, Qi XJ, Willner I. Multitriggered shape-memory acrylamide–DNA hydrogels. *Journal of the American Chemical Society*. 2015;**137**:15723-15731. DOI: 10.1021/jacs.5b06510
- [31] Strandman S, Zhu XX. Self-healing supramolecular hydrogels based on reversible physical interactions. *Gels*. 2016;**2**:16. DOI: 10.3390/gels2020016
- [32] Webber MJ, Langer R. Drug delivery by supramolecular design. *Chemical Society Reviews*. 2017;**46**:6600-6620. DOI: 10.1039/C7CS00391A
- [33] Sliwa W, Girek T. CD-based rotaxanes and polyrotaxanes as representative supramolecules. In: Sliwa W, Girek T, editors. *Cyclodextrins*. Weinheim: Wiley-VCH Verlag; 2017. pp. 9-50. DOI: 10.1002/9783527695294.ch1
- [34] Feng W, Zhou W, Dai Z, Yasin A, Yang H. Tough polypseudorotaxane supramolecular hydrogels with dual-responsive shape memory properties. *Journal of Materials Chemistry B*. 2016;**4**:1924-1931. DOI: 10.1039/C5TB02737C
- [35] Cai T, Huo S, Wang T, Sun W, Tong Z. Self-healable tough supramolecular hydrogels crosslinked by poly-cyclodextrin through host-guest interaction. *Carbohydrate Polymers*. 2018;**193**:54-61. DOI: 10.1016/j.carbpol.2018.03.039
- [36] Dong ZQ, Cao YY, Yuan QJ, Wang YF, Li JH, Li BJ, Zhang S. Redox- and glucose-induced shape-memory polymers. *Macromolecular Rapid Communications*. 2013;**34**:867-872. DOI: 10.1002/marc.201300084
- [37] Han XJ, Dong ZQ, Fan MM, Liu Y, Li JH, Wang YF, Yuan QJ, Li BJ, Zhang S. pH-induced shape-memory polymers. *Macromolecular Rapid Communications*. 2012;**33**:1055-1060. DOI: 10.1002/marc.201200153
- [38] Zhang T, Silverstein MS. Doubly-crosslinked, emulsion-templated hydrogels through reversible metal coordination. *Polymer*. 2017;**126**:386-394. DOI: 10.1016/j.polymer.2017.07.044
- [39] Zheng SY, Ding H, Qian J, Yin J, Wu ZL, Song Y, Zheng Q. Metal-coordination complexes mediated physical hydrogels with high toughness, stick–slip tearing behavior, and good processability. *Macromolecules*. 2016;**49**:9637-9646. DOI: 10.1021/acs.macromol.6b02150
- [40] Le X, Zhang Y, Lu W, Wang L, Zheng J, Ali I, Zhang J, Huang Y, Serpe MJ, Yang X, Fan X, Chen T. A novel anisotropic hydrogel with integrated self-deformation and controllable shape memory effect. *Macromolecular Rapid Communications*. 2018:1800019. DOI: 10.1002/marc.201800019
- [41] Harris RD, Auletta JT, Motlagh SAM, Lawless MJ, Perri NM, Saxena S, Weiland LM, Waldeck DH, Clark WW, Meyer TY. Chemical and electrochemical manipulation of

- mechanical properties in stimuli-responsive copper-cross-linked hydrogels. *ACS Macro Letters*. 2013;**2**:1095-1099. DOI: 10.1021/mz4004997
- [42] Nan W, Wang W, Gao H, Liu W. Fabrication of a shape memory hydrogel based on imidazole–zinc ion coordination for potential cell-encapsulating tubular scaffold application. *Soft Matter*. 2013;**9**:132-137. DOI: 10.1039/C2SM26918J
- [43] Feng W, Zhou W, Zhang S, Fan Y, Yasin A, Yang H. UV-controlled shape memory hydrogels triggered by photoacid generator. *RSC Advances*. 2015;**5**:81784-81789. DOI: 10.1039/C5RA14421C
- [44] Sun JY, Zhao X, Illeperuma WRK, Chaudhuri O, Oh KH, Mooney DJ, Vlassak JJ, Suo Z. Highly stretchable and tough hydrogels. *Nature*. 2012;**489**:133-136. DOI: 10.1038/nature11409
- [45] Meng H, Xiao P, Gu J, Wen X, Xu J, Zhao C, Zhang J, Chen T. Self-healable macro-/microscopic shape memory hydrogels based on supramolecular interactions. *Chemical Communications*. 2014;**50**:12277-12280. DOI: 10.1039/C4CC04760E
- [46] Yasin A, Li H, Lu Z, ur Rehman S, Siddiq M, Yang H. A shape memory hydrogel induced by the interactions between metal ions and phosphate. *Soft Matter*. 2014;**10**:972-977. DOI: 10.1039/C3SM52666F
- [47] Si Y, Wang L, Wang X, Tang N, Yu J, Ding B. Ultrahigh-water-content, superelastic, and shape-memory nanofiber-assembled hydrogels exhibiting pressure-responsive conductivity. *Advanced Materials*. 2017;**29**:1700339. DOI: 10.1002/adma.201700339
- [48] Ren Z, Zhang Y, Li Y, Xu B, Liu W. Hydrogen bonded and ionically crosslinked high strength hydrogels exhibiting  $\text{Ca}^{2+}$ -triggered shape memory properties and volume shrinkage for cell detachment. *Journal of Materials Chemistry B*. 2015;**3**:6347-6354. DOI: 10.1039/C5TB00781J
- [49] Zhang Y, Liao J, Wang T, Sun W, Tong Z. Polyampholyte hydrogels with pH modulated shape memory and spontaneous actuation. *Advanced Functional Materials*. 2018: 1707245. DOI: 10.1002/adfm.201707245
- [50] Pu W, Jiang F, Chen P, Wei B. A POSS based hydrogel with mechanical robustness, cohesiveness and a rapid self-healing ability by electrostatic interaction. *Soft Matter*. 2017;**13**:5645-5648. DOI: 10.1039/C7SM01492A
- [51] Zhang Y, Yang B, Zhang X, Xu L, Tao L, Li S, Wei Y. A magnetic self-healing hydrogel. *Chemical Communications*. 2012;**48**:9305. DOI: 10.1039/c2cc34745h
- [52] Wei H, Du S, Liu Y, Zhao H, Chen C, Li Z, Lin J, Zhang Y, Zhang J, Wan X. Tunable, luminescent, and self-healing hybrid hydrogels of polyoxometalates and triblock copolymers based on electrostatic assembly. *Chemical Communications*. 2014;**50**:1447-1450. DOI: 10.1039/C3CC48732F



*Edited by Alicia Esther Ares*

Shape-memory materials are materials that react under variations of electric or magnetic fields, physical or chemical changes, and that when returning to the initial conditions recover their original form, capable of repeating this process an infinite number of times without deteriorating.

The characteristics, fabrication techniques, and thermomechanical treatment of various shape-memory materials are described in detail in this book. The book describes several principles and applications.

Published in London, UK

© 2018 IntechOpen  
© nespix / iStock

**IntechOpen**

